Electrochemical Characterization of Nanomaterials and Development of New Electrochemical Methods

Chu Han

A dissertation

submitted in partial fulfillment of the

requirements for the degree of

Doctor of Philosophy

University of Washington

2018

Reading Committee:

Bo Zhang, Chair

Charles T. Campbell

D. Michael Heinekey

Program Authorized to Offer Degree:

Chemistry

University of Washington

Abstract

Electrochemical Characterization of Nanomaterials and Development of New Electrochemical Methods

Chu Han

Chair of the Supervisory Committee:
Professor Bo Zhang
Department of Chemistry

This dissertation focuses on studying fundamental properties of nanomaterials with electrochemical methods and the development of new electrochemical methods to study single nanoparticles and vesicles. Chapter 1 introduces nanomaterials including nanoparticles and nanoparticle films and addresses the importance of single-nanoparticle study with electrochemical methods. This chapter also discusses the electrochemical methods that are employed in the following chapters. Chapter 2 discusses the electrochemical characterization of uniform ultrathin nanoparticle films that can be fabricated by layer-by-layer assembly with well-controlled film thickness and composition. The electrocatalytic activity towards oxygen reduction reaction of the film are studied with voltammetric techniques. Chapter 3 discusses the characterization of single Janus Au-SiO_2 nanoparticle with single-nanoparticle collision method. The apparent electroactive area of single Janus nanoparticles can be obtained from the transient current signals from hydrazine

oxidation and proton reduction. The study in chapter 4 represents the first evidence that transient bipolar electrochemistry can happen on small free moving metal nanoparticles. This innovative study utilizes the highly focusing power of a nanopore for the applied voltage so that the potential drop across a 40 nm particle is sufficient to couple two electrochemical reactions. The use of nanopore and resistive-pulse sensing may be extended to future nanoparticle studies in ultrafast electrochemistry, nanoparticle catalyst screening, and gas nucleation on nanoparticle. In chapter 5 we design a high throughput electrochemical analyzer for counting and sizing single vesicles and propose its potential in integration with ultramicroelectrodes to obtain more complicated information of singe vesicles.

TABLE OF CONTENTS

LIST OF FIGURES

LIST OF TABLES

ACKNOWLEDGEMENTS

I would like to thank Professor Bo Zhang for his guidance in the past five years. He is a knowledgeable scientist and great advisor, and he encouraged me to continuously learn and try new things in graduate school. I also would like to thank my committee members: Prof. Charles T. Campbell, Prof. Michael Heinekey, and Prof. Guozhong Cao for their valuable suggestions and feedback on my research.

I appreciate the help from all the present and past members in the Zhang lab. I would like to thank Dr. Steve J. Percival for being a great mentor to me in the beginning of my graduate school. I learn and grow a lot from the collaboration with him, and I want to thank him for always being patient and supportive. Thanks to Dr. Rui Hao for his countless brilliant ideas and suggestions, especially on the Ag nanoparticle project. I also would like to thank Yunshan Fan for being a great friend and coworker all the time. I would also like to thank several people: Dr. Zhihui Guo, Dr. Jin Lu, Dr. Chris Gunderson, Dr. Steve Oja and all others, you are all great people to work with.

I would like to thank my parents for their unconditional love since I was born. Although we are thousands of miles away, they are always there to support and motivate me when I feel down. I also would like to thank Kun for his support. I would like to thank all of my friends for their friendship and love.

Chapter 1. INTRODUCTION

1.1 ELECTROCHEMISTRY

Electrochemistry, as a branch of chemistry, studies the charge transfer process at electrode/electrolyte interfaces and has wide applications in battery, catalysis, chemical analysis, sensing, imaging, and corrosion protection. Electrochemical methods are commonly used as tools to study chemical systems. In a traditional electrochemical cell, a potentiostat controls the potential bias between a working electrode and a reference electrode. Electrons could flow from a working electrode surface and reduce redox molecules in the solution when a relatively negative potential was applied on the working electrode and vice versa. By measuring the electrical potential, current, or charge and their relationship with the chemical parameters, one can obtain abundant information of analytes including the identity, concentration, reaction kinetics, etc.[1] Besides the intrinsic properties of the analytes, the geometry, material and surface property of the electrode can also affect the electrochemical reaction, especially for inner-sphere reactions. One of the typical electrochemical analytical methods is cyclic voltammetry: a potential applied on the electrode is continuously cycled in a certain range that can oxidize or reduce the analyte while the current flowing through the electrode is measured and plotted versus applied potential. Another common approach is chronoamperometry in which a constant potential is held to continuously reducing or oxidizing the analyte and the current is monitored over time. A better understanding of the electrochemical interface is critical for designing better electrochemical systems for sensing and energy field. Therefore, it is critical for us to study fundamental electrochemistry at the electrode/solution interface in order to solve real-world problems.

1.2 NANOSCALE ELECTROCHEMISTRY

A variety of nanoscale materials such as nanoparticles, nanowires and nanoparticle films have been designed and synthesized since last century. They have high surface-to-volume ratio and exhibit unique properties that are not shown in bulk materials.[2] Metal nanoparticles such as gold, platinum and silver nanoparticles are especially important due to their unique physical and chemical properties. The localized surface plasmon resonance characteristics of metal nanoparticles are extensively used in chemical sensing and biosensing field[3, 4]. More importantly, nanoparticles are excellent catalysts due to their large surface area and high density of active sites, and they have been widely applied to photocatalysis[5] and electrocatalysis[6, 7]. Nanoparticles could be selectively synthesized to achieve different functions, and the shape, size and surface properties of nanoparticles are closely related to their optical and catalytic properties. Therefore, significant effort has been put into improving the understanding of the fundamental properties of nanoparticles.[8]

Nanoparticles can be assembled to form two-dimensional nanoparticle films, which have high surface area and collective nanoscale features and can be used as devices to produce measurable signals.[9] Therefore, nanoparticle films are especially useful in several application areas such as fuel cell catalysis[10], chemical and biosensing.[11] There are to date several approaches to fabricate nanoparticle films including in-situ growth of nanoparticles in a polymer template,[12,13] Langmuir-Blodgett method,[14,15] sol-gel chemistry-based deposition,[16] electrodeposition,[17,18] and layer-by-layer deposition,[19,20,21] However, it is still challenging to fabricate nanoparticle films with a good control of the film structure and composition. In chapter 2, we report the preparation, characterization, and electrochemical study of conductive, ultrathin films made of cross-linked metal nanoparticles. Nanoparticle films ranging from 40 to 200 nm in thickness composed of gold

and platinum nanoparticles of ~5 nm can be fabricated via a powerful layer-by-layer spin coating process. This process allows preparation of uniform nanoparticle films as large as 2 × 2 cm^2 with precise control over thickness, structure, and electrochemical and electrocatalytic properties. Gold, platinum, and bimetallic nanoparticle films were fabricated and characterized using cyclic voltammetry, scanning electron microscopy, and conductance measurements. We investigate their electrocatalytic activity toward the oxygen reduction reaction (ORR), and our results show that the electrochemical activity of such nanoparticle films is initially hindered by the presence of dense thiolate cross-linking ligands. Both electrochemical cycling and oxygen plasma cleaning are effective means in restoring their electrochemical activity. Gold nanoparticle films have higher electric conductivity than platinum possibly due to more uniform film structure and closer particle−particle distance. The electrochemical and electrocatalytic performance of platinum nanoparticle films can be greatly enhanced by the incorporation of gold NPs.

The performance of nanoparticle film is based on the average of the response on a large quantity of nanoparticles, while analyzing each individual response can help to improve the overall performance for applications. To further investigate the heterogeneity among nanoparticles, it is necessary to conduct single-nanoparticle level study. Tremendous characterization techniques have been applied to study single nanoparticles, including electron microscopy such as scanning electron microscopy (SEM) and transmission electron microscopy (TEM), optical methods such as fluorescence microscopy, dark field microscopy, and surface plasmon resonance microscopy.[22] Electrochemical methods are especially useful in characterizing single nanoparticles. Since mid-1980s, the development in nanofabrication produced nanoscale electrochemical probes like ultramicroelectrodes, nanoelectrodes, and nanopores, which significantly improve the sensitivity of electrochemical detection.[23,24] Ultramicroelectrodes can be used to detect stochastic, transient

electrochemical events caused by single nanoparticles. Nanoelectrodes can be used to conduct real single-particle study by isolating a single nanoparticle on the surface. Moreover, smaller double layer capacitance and faster mass transport of nanoelectrodes enable the detection of ultrafast electron-transfer kinetics. Nanopores are high throughput and simple tools to detect single nanoparticles and get abundance information such as the shape, size and surface charge of nanoparticles. With nanoscale electrochemical probes, electrochemistry can achieve picoamps current and nanoseconds time resolution, and has become a powerful tool in studying numerous properties of nanoparticles.[24] The following sections in this chapter will introduce electrochemical characterization of single nanoparticles with these electrochemical tools.

1.3 NANOPARTICLE COLLISION

Nanoparticle collision (or nanoparticle impact) is an efficient and simple experimental approach to electrochemically characterize single nanoparticles with an ultramicroelectrode. The idea was initially proposed by Lemay group in 2004 to detect individual nonreactive microbeads when they adsorb on a microelectrode and block mass transfer of redox mediators.[25] Bard group further developed a method of electrocatalytic current amplification via nanoparticle collision.[26,27] By holding a constant potential on an inert electrode where the faradaic reaction of the electroactive species does not happen, an electrocatalytically active nanoparticle landing on the electrode surface could catalyze the faradaic reaction and produce an increased current signal. The current signal could be determined by the nanoparticle size, shape and electrocatalytic activity. Therefore, nanoparticle collision could reveal abundant information of single nanoparticles.

Based on this initial idea, various experimental systems have been explored to detect different nanoparticle with the use of different electrode and electroactive species. For example, Pt,[28] Au,[29] Ag,[30] IrO_x,[31] TiO_2,[32] CeO_2,[33] ZnO,[34] Mo,[35] and fullerene[36] nanoparticles have been

detected. Soft particles such as emulsion droplets, liposomes and vesicles were also reported.[37, 38, 39] In chapter 3, we report the electrochemical characterization of apparent electroactive area of Janus Au-silica nanoparticles at the single particle level with nanoparticle collision method. By holding a constant potential on an inert carbon ultramicroelectrode (UME), current transient can be induced and detected when a single Janus nanoparticle lands on the electrode surface and catalyzes the reaction of hydrazine oxidation or proton reduction. We are able to calculate the electroactive area of Au-SiO_2 nanoparticles from the current signals. Through the finite-element simulation of the hydrazine concentration profile on the Au-SiO_2 nanoparticle, the geometry of nanoparticles was correlated with electroactivity. This work demonstrates that nanoparticle collision experiment can be a simple and efficient technique to characterize single Janus nanoparticles and study the geometry quantitatively.

1.4 Bipolar Electrochemistry

A bipolar electrode is an electrode that could couple oxidation and reduction reaction separately on its two extremities.[40] A bipolar electrode is quite different from a traditional working electrode. Generally, as the setup shows in Figure 1.1, a bipolar electrode can be simplified as a conductor that is placed in the electrolyte between two driving electrodes. A sufficiently high potential is applied between the driving electrodes and there is a potential drop in the electrolyte solution, which induces potential difference at conductor/solution interfaces. The maximum potential difference is at the two extremities of the conductor. If the potential difference is large enough, faradaic processes could be coupled on the conductor: reduction reaction at the cathodic pole coupled with oxidation reactions at the anodic pole. To maintain electroneutrality, the reduction and oxidation reactions must occur at the same rate, indicating that we could investigate the reaction at one pole by monitoring the reaction at the other pole.[41]

Compared to traditional electrochemistry, bipolar electrochemistry is advantageous in several aspects: Firstly, the experimental setup is greatly simplified because no direct electrical contact is needed. One power supply is able to drive the coupled faradaic reaction simultaneously on millions of bipolar electrodes, such as micro- and nano-electrode arrays, which increases the sensing area dramatically.[42,43] Secondly, the currents flow in cathodic pole is equal to the current in anodic pole. Therefore, one can use fluorescence or luminescence to monitor the electrochemical reaction at the opposite pole.[44] Our group has done a lot of work in developing a detection system called fluorescence-enabled electrochemical microscopy (FEEM) to couple a conventional redox reaction with a fluorogenic redox reaction on a bipolar electrode.[42, 45] Bipolar electrochemistry has also been widely used in electrocatalyst screening,[42] material synthesis,[46] and micro- or nano-motors.[47, 48] Such experiments often require the use of micro-sized objects in order to have sufficient potential drop across the particle length. It would be interesting and necessary to study bipolar electrochemistry on a single nanoparticle to address some fundamental questions, such as how redox reactions are coupled on the same nanoparticle. Also, nanoparticles can be potentially applied as nanoscale bipolar electrodes for FEEM, which could significantly improve the spatial resolution of fluorescence imaging. However, bipolar coupling on objects down to nanometer scale is still very challenging. In chapter 5, we report the observation of transient bipolar electrochemical coupling on freely-moving 40 nm silver nanoparticles. The use of an asymmetric electrochemical environment at the nanopore orifice enabled us to observe unusually large current blockages of single Ag nanoparticles. We attribute these current blockages to the formation of H_2 nanobubbles on the surface of translocating Ag nanoparticles due to the coupled faradaic reactions, in which the reduction of protons and water is coupled to the oxidation of Ag and water under potentials higher than 1 V. The appearance of large current blockages is strongly dependent on

voltage and the choice of anions in the bulk solution. The correlation between large current blockages with the oxidation of Ag nanoparticles and their nanopore translocation was further confirmed by simultaneous fluorescence and electric recordings. This study demonstrates that transient bipolar electrochemistry can take place on small metal nanoparticles when they pass through nanopores where the electric field is highly localized. The use of a nanopore and the resistive-pulse sensing method to study transient bipolar electrochemistry of nanoparticles may be extended to the future studies in ultrafast electrochemistry, nanocatalyst screening, and gas nucleation on nanoparticles.

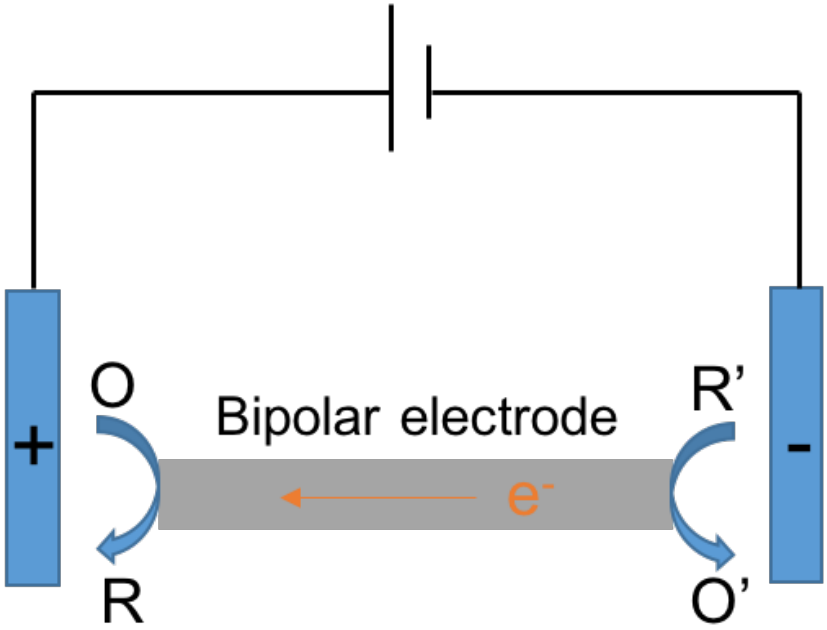

Figure 1.1. Experimental setup of a bipolar electrode system

1.5 NANOPORE SENSING

Nanopore sensing is another popular electrochemical method to detect single nanoparticles. The mechanism is based on the Coulter-counter principle, which was discovered by Wallace Coulter in the 1950s.[49] The Coulter counter has electrolyte solution in two compartments separated by a micrometer-sized pore. Two electrodes are placed in opposite sides of the pore, and a potential bias is applied between electrodes. Ionic current flows through the pore and is measured as a function of time. The ionic current is determined by the pore geometry and electrolyte conductivity. Analyte particles present in electrolyte solution are pulled through the pore by either pressure or electrophoretic force and displace a certain amount of ions in the pore, resulting in a transient change in ionic resistance that is proportional to the volume of the particle, and the passage of particle is reflected as a resistive current pulse in the current-time trace. Coulter counter is mainly applied to counting and sizing blood cells in electrolytes. With the development of nanofabrication technique, the pore can be shrinked to nanometer scale and be used to detect nanoscale objects. In recent years, nanopore sensing technique has been further expanded to detect various analytes such as molecules,[50,51] viruses,[52,53] DNA,[54,55] and nanoparticles.[56-59] Various kinds of nanopores have been fabricated for different applications, such as silicon nitride pores,[60,61] glass nanopores and nanopipettes, [62] and biological nanopores [63] . Nanopore sensing has been widely used in nanoparticle counting and sizing as a high-throughput and nondestructive technique. [64] The magnitude of the current pulse is proportional to the size of the nanoparticle, and the pulse duration tells us the nanoparticle translocation time through the nanopore. Besides, nanopore sensing could also reveal other information including surface charge[65] and shape of the nanoparticle[66], as well as the geometry of the pore and interior surface of the pore[67]. In chapter 4 we proposed a new

approach to study the transient bipolar electrochemical reactions on a single nanoparticle in a nanopore and detect the nanobubble on a single nanoparticle based on nanopore sensing technique. Nanopores are also useful in detecting soft particles such as microgel and liposomes.[68,69] These soft particles could deform during translocation process and are more complicated than solid nanoparticles, but the study of soft particles could also reveal more interesting information, and the study of soft particles could also be applied to the study of biological vesicles. Presented in chapter 5 is a detailed report on the design and fabrication of a glass microbulb analyzer and its application in detection of single vesicles isolated from PC12 cells with nanopore sensing technique.

1.6 REFERENCES

(1) Wang, J. Analytical Electrochemistry, John Wiley & Sons VCH, Hoboken, New Jersey, USA, **2006**.

(2) Roduner, E. Size Matters: Why Nanomaterials are Different. *Chem. Soc. Rev.* **2006**, *35*, 583-592.

(3) Unser, S.; Bruzas, I.; He, J.; Sagle, L. Localized Surface Plasmon Resonance Biosensing: Current Challenges and Approaches. *Sensors,* **2015**, *15*, 15684-15716.

(4) Campbell, F. W.; Compton, R. G.; The use of Nanoparticles in Electroanalysis: an Updated Review. *Anal. Bioanal. Chem.,* **2010**, *396*, 241-259.

(5) Avasare, V.; Zhang, Z.; Avasare, D.; Khan, I.; Qurashi.; A. Room-Temperature Synthesis of TiO_2 Nanospheres and their Solar Driven Photoelectrochemical Hydrogen Production *Int. J. Energy Res.,* **2015**, *39*, 1714-1719.

(6) Ning, F.; Shao, M.; Xu, S.; Y. Fu, R. Zhang, M. Wei, D.G. Evans, X. Duan. TiO_2/graphene/NiFe-layered Double Hydroxide Nanorod Array Photoanodes for Efficient Photoelectrochemical Water Splitting. *Energy Environ. Sci*., **2016**, 9, 2633-2643.

(7) Koper. M. T. M. Structure Sensitivity and Nanoscale Effects in Electrocatalysis. *Nanoscale*, **2011**, *3*, 2054-2073.

(8) Kleijn, S.E.F; Lai, S.C.S.; Koper, M.T.M.; Unwin, P.R. Electrochemistry of Nanoparticles. *Angew. Chem. Int. Ed*. **2014**, *53*, 3558-3586.

(9) Hanarp, P.; Sutherland, D. S.; Gold, J.; Kasemo, B. Control of Nanoparticle Film Structure for Colloidal Lithography. *Colloids Surf. A* **2003**, *214*, 23-26.

(10) Kumar, S.; Zou, S. Electrooxidation of Carbon Monoxide and Methanol on Platinum-Overlayer-Coated Gold Nanoparticles: Effects of Film Thickness. *Langmuir* **2007**, *23*, 7365-7371.

(11) Jia, J.; Wang, B.; Wu, A.; Cheng, G.; Li, Z.; Dong, S. A Method to Construct a Third-generation Horseradish Peroxidase Biosensor: Self-Assembling Gold Nanoparticles to Three-Dimensional Sol-Gel Network. *Anal. Chem*. **2002**, *74*, 2217-2223.

(12) Boontongkong, Y.; Cohen, R. E. Cavitated Block Copolymer Micellar Thin Films: Lateral Arrays of Open Nanoreactors. *Macromolecules* **2002**, *35*, 3647-3652.

(13) Segalman, R. A. Patterning with Block Copolymer Thin Films. *Mater. Sci. Eng., R.* **2005**, *48*, 191-226.

(14) Paul, S.; Pearson, C.; Molloy, A.; Cousins, M. A.; Green, M.; Kolliopoulou, S.; Dimitrakis, P.; Normand, P.; Tsoukalas, D.; Petty, M. C. Langmuir-Blodgett Film Deposition of Metallic Nanoparticles and their Application to Electronic Memory Structures. *Nano Lett.* **2003**, *3*, 533-536.

(15) Brust, M.; Stuhr-Hansen, N.; Norgaard, K.; Christensen, J. B.; Nielsen, L. K.; Bjornholm, T. Langmuir-Blodgett Films of Alkane Chalcogenide (S, Se, Te) Stabilized Gold Nanoparticles. *Nano Lett.* **2001**, *1*, 189-191.

(16) Fan, H. Y.; Wright, A.; Gabaldon, J.; Rodriguez, A.; Brinker, C. J.; Jiang, Y. B. Three-Dimensionally Ordered Gold Nanocrystal/Silica Superlattice Thin Films Synthesized via Sol-Gel Self-Assembly. *Adv. Funct. Mater.* **2006**, *16*, 891-895.

(17) Zhao, L. Y.; Eldridge, K. R.; Sukhija, K.; Jalili, H.; Heinig, N. F.; Leung, K. T. Electrodeposition of Iron Core-shell Nanoparticles on a H-terminated Si (100) Surface. *Appl. Phys. Lett.* **2006**, *88*, 033111.

(18) Quinn, B. M.; Dekker: C.; Lemay, S. G. Electrodeposition of Noble Metal Nanoparticles on Carbon Nanotubes. *J. Am. Chem. Soc*. **2005**, *127*, 6146-6147.

(19) Iler, R. K. Multilayers of Colloidal Particles. *J. Colloid Interface Sci*. **1966**, *21*, 569-594.

(20) Decher, G.; Hong, J. D. Buildup of Ultrathin Multilayer Films by a Self-Assembly process, 1 Consecutive Adsorption of Anionic and Cationic Bipolar Amphiphiles on Charged Surfaces. *Makromol. Chem., Macromol. Symp.* **1991**, *46*, 321-327.

(21) Lee, D.; Rubner, M. F.; Cohen, R. E. All-Nanoparticle Thin-Film Coatings. *Nano Lett.*, **2006**, *6*, 2305-2312.

(22) Wang, W.; Tao, N. Detection, Counting, and Imaging of Single Nanoparticles. *Anal. Chem.* **2014**, *86*, 2-14.

(23) Cox, J. T.; Zhang, B. Nanoelectrodes: Recent Advances and New Directions. *Annu. Rev. Anal. Chem.* **2012**, *5*, 253-272.

(24) Oja, S. M.; Wood, M.; Zhang, B. Nanoscale Electrochemistry. *Anal. Chem.* **2013**, *85*, 473-486.

(25) Quinn, B. M; van 't Hof, P. G.; Lemay. S. G. Time-Resolved Electrochemical Detection of Discrete Adsorption Events. *J. Am. Chem. Soc*. **2004**, *126*, 8360-8361.

(26) Xiao, X.; Bard, A. J. Observing Single Nanoparticle Collisions at an Ultramicroelectrode by Electrocatalytic Amplification. *J. Am. Chem. Soc*. **2007**, *129*, 9610-9612.

(27) Xiao, X.; Fan, F.-R. F.; Zhou, J.; Bard, A. J. Current Transients in Single Nanoparticle Collision Events. *J. Am. Chem. Soc.* **2008**, *130*, 16669-16677.

(28) Wakerley, D.; Güell, A. G.; Hutton, L. A.; Miller, T. S.; Bard, A. J.; Macpherson, J. V. Boron Doped Diamond Ultramicroelectrodes: A Generic Platform for Sensing Single Nanoparticle Electrocatalytic Collisions. *Chem. Commun.* **2013**, *49*, 5657-5659.

(29) Zhou, H.; Fan, F.-R. F.; Bard, A. J. Observation of Discrete Au Nanoparticle Collisions by Electrocatalytic Amplification using Pt Ultramicroelectrode Surface Modification. *J. Phys. Chem. Lett.* **2010**, *1*, 2671-2674.

(30) Oja, S. M.; Robinson, D. A.; Vitti, N. J.; Edwards, M. A.; Yuwen Liu, White, H. S.; Zhang, B. Observation of Multipeak Collision Behavior during the Electro-Oxidation of Single Ag Nanoparticles. *J. Am. Chem. Soc.* **2017**, *139*, 708-718.

(31) Kwon, S. J.; Bard, A. J. Analysis of Diffusion-Controlled Stochastic Events of Iridium Oxide Single Nanoparticle Collisions by Scanning Electrochemical Microscopy. *J. Am. Chem. Soc*. **2012**, *134*, 7102-7108.

(32) Fernando, A.; Parajuli, S.; Alpuche-Aviles, M. A. Observation of Individual Semiconducting Nanoparticle Collisions by Stochastic Photoelectrochemical Currents. *J. Am. Chem. Soc.* **2013**, *135*, 10894-10897.

(33) Sardesai, N. P.; Andreescu, D.; Andreescu, S. Electroanalytical Evaluation of Antioxidant Activity of Cerium Oxide Nanoparticles by Nanoparticle Collisions at Microelectrodes. *J. Am. Chem. Soc.* **2013**, *135*, 16770-16773.

(34) Perera, N.; Karunathilake, N.; Chhetri, P.; Alpuche-Aviles, M. A. Electrochemical Detection and Sizing of Colloidal ZnO Nanoparticles. *Anal. Chem.* **2015**, *87*, 777-784.

(35) Giovanni, M.; Ambrosi, A.; Sofer, Z.; Pumera, M. Impact Electrochemistry of Individual Molybdenum Nanoparticles. *Electrochem. Commun.* **2015**, *56*, 16-19.

(36) Stuart, E. J. E.; Tschulik, K.; Batchelor-McAuley, C.; Compton, R. G. Electrochemical Observation of Single Collision Events: Fullerene Nanoparticles. *ACS Nano.* **2014**, *8*, 7648-7654.

(37) Cheng, W.; Compton, R. G. Oxygen Reduction Mediated by Single Nanodroplets Containing Attomoles of Vitamin B12: Electrocatalytic Nano-Impacts Method. *Angew. Chem., Int. Ed.* **2015**, *54*, 7082-7085.

(38) Dunevall, J.; Fathali, H.; Najafinobar, N.; Lovric, J.; Wigstrom, J.; Cans, A. S.; Ewing, A. G. Characterizing the Catecholamine Content of Single Mammalian Vesicles by Collision–Adsorption Events at an Electrode. *J. Am. Chem. Soc.* **2015**, *137*, 4344-4346.

(39) Toh, H. S.; Compton, R. G. Electrochemical Detection of Single Micelles through 'Nano-Impacts'. *Chem. Sci.* **2015**, *6*, 5053-5058.

(40) Mavre, F.; Anand, R. K.; Laws, D. R.; Chow, K.-F.; Chang, B.-Y.; Crooks, J. A.; Crooks, R. M. Bipolar Electrodes: A Useful Tool for Concentration, Separation, and Detection of Analytes in Microelectrochemical Systems. *Anal. Chem.* **2010**, *82*, 8766-8774.

(41) Zhang, X.; Zhai, Q.; Xing, H.; Li, J.; Wang, E. Bipolar Electrodes with 100% Current Efficiency for Sensors. *ACS Sensors* **2017**, *2*, 320-326.

(42) Guerrette, J. P., Percival, S. J., Zhang, B. Fluorescence Coupling for Direct Imaging of Electrocatalytic Heterogeneity. *J. Am. Chem. Soc*. **2013**, 135, 855-861.

(43) Chow, K.-F.; Mavre´, F.; Crooks, R. M. Wireless Electrochemical DNA Microarray Sensor. *J. Am. Chem. Soc*. **2008**, *130*, 7544-7545.

(44) Arora, A.; Eijkel, J. C. T.; Morf, W. E.; Manz, A. A Wireless Electrochemiluminescence Detector Applied to Direct and Indirect Detection for Electrophoresis on a Microfabricated Glass Device. *Anal. Chem.* **2001**, *73*, 3282-3288.

(45) Oja, S. M.; Guerrette, J. P.; David, M. R.; Zhang, B. Fluorescence-Enabled Electrochemical Microscopy with Dihydroresorufin as a Fluorogenic Indicator. *Anal. Chem.* **2014**, *86*, 6040-6048.

(46) Wood, M.; Zhang, B. Bipolar Electrochemical Method for Dynamic *In Situ* Control of Single Metal Nanowire Growth. *ACS Nano.* **2015**, *9*, 2454-2464.

(47) Paxton, W. F.; Kistler, K. C.; Olmeda, C. C.; Sen, A.; St. Angelo, S. K.; Cao, Y.; Mallouk, T. E.; Demirok, U. K.; Laocharoensuk R.; Manesh, K. M.; Wang, J. Fluorescence-Enabled Electrochemical Microscopy with Dihydroresorufin as a Fluorogenic Indicator. *Angew. Chem. Int. Ed*. **2008**, *47*, 9349-9351.

(48) Lammert, P. E.; Crespi, V. H.; Catalytic Nanomotors: Autonomous Movement of Striped Nanorods. *J. Am. Chem. Soc*. **2004**, *126*, 13424-13431.

(49) Coulter, W. H. U.S. Patent 2656508, October 20, 1953.

(50) Howorka, S.; Siwy, Z. Nanopore Analytics: Sensing of Single Molecules. *Chem. Soc. Rev.* **2009**, *38*, 2360-2384.

(51) Bayley, H.; Cremer, P. S. Stochastic Sensors Inspired by Biology. *Nature* **2001**, *413*, 226-230.

(52) Zhou, K.; Li, L.; Tan, Z.; Zlotnick, A.; Jacobson, S. C. Characterization of Hepatitis B Virus Capsids by Resistive-Pulse Sensing. *J. Am. Chem. Soc.* **2011**, *133*, 1618-1621.

(53) Deblois, R. W.; Wesley, R. K. A. Sizes and Concentrations of Several type C Oncornaviruses and Bacteriophage T2 by the Resistive-Pulse Technique. *J. Virol.* **1977**, *23*, 227-233.

(54) Smeets, R. M. M.; Keyser, U. F.; Krapf, D.; Wu, M.-Y.; Dekker, N. H.; Dekker, C. Salt Dependence of Ion Transport and DNA Translocation through Solid-State Nanopores. *Nano Lett.* **2006**, *6*, 89-95.

(55) Deamer, D. W.; Branton, D. Characterization of Nucleic Acids by Nanopore Analysis. *Acc. Chem. Res.* **2002**, *35*, 817-825.

(56) Deblois, R. W.; Bean, C. P. Counting and Sizing of Submicron Particles by the Resistive Pulse Technique. *Rev. Sci. Instrum*. **1970**, *41*, 909-916.

(57) Deblois, R. W.; Bean, C. P.; Wesley, R. K. A. Electrokinetic Measurements with Submicron Particles and Pores by the Resistive Pulse Technique. *J. Colloid Interface Sci.* **1977**, *61*, 323-335.

(58) Henriquez, R. R.; Ito, T.; Sun, L.; Crooks, R. M. The Resurgence of Coulter Counting for Analyzing Nanoscale Objects. *Analyst* **2004**, *129*, 478-482.

(59) Lan, W. J.; Holden, D. A.; Zhang, B.; White, H. S. Nanoparticle Transport in Conical-Shaped Nanopores. *Anal. Chem.* **2011**, *83*, 3840-3847.

(60) Li, J.; Stein, D.; McMullan, C.; Branton, D.; Aziz, M. J.; Golovchenko, J. A. Ion-Beam Sculpting at Nanometre Length Scales. *Nature* **2001**, *412*, 166-169.

(61) Li, J. L.; Gershow, M.; Stein, D.; Brandin, E.; Golovchenko, J. A. DNA Molecules and Configurations in a Solid-State Nanopore Microscope. *Nat. Mater*. **2003**, *2*, 611-615.

(62) Wang, Y.; Kececi, K.; Mirkin, M. V.; Mani, V.; Sardesai, N.; Rusling, J. F. Resistive-Pulse Measurements with Nanopipettes: Detection of Au Nanoparticles and Nanoparticle-Bound Anti-Peanut IgY. *Chem. Sci*. **2013**, *4*, 655-663.

(63) Bezrukov, S. M.; Vodyanoy, I.; Parsegian, V. A. Counting Polymers Moving through a Single Ion Channel. *Nature* **1994**, *370*, 279-281.

(64) Luo, L.; German, S. R.; Lan, W.-J.; Holden, D. A.; Mega, T. L.; White, H. S. Resistive-Pulse Analysis of Nanoparticles. *Annu. Rev. Anal. Chem.* **2014**, *7*, 513-535.

(65) Lan, W.-J.; Kubeil, C.; Xiong, J.-W.; Bund, A.; White, H. S. Effect of Surface Charge on the Resistive Pulse Waveshape during Particle Translocation through Glass Nanopores. *J. Phys. Chem. C* **2014**, *118*, 2726−2734.

(66) Zhang, Y.; Edwards, M. A.; German, S. R.; White, H. S. Multipass Resistive-Pulse Observations of the Rotational Tumbling of Individual Nanorods. *J. Phys. Chem. C* **2016**, *37*, 20781-20788.

(67) Pevarnik, M.; Healy, K.; Toimil-Molares, M.E.; Morrison, A.; Letant, S.E.; Siwy, Z.S. Polystyrene Particles Reveal Pore Substructure as they Translocate. *ACS Nano* **2012,** *6*, 7295-7302.

(68) Holden, D.A.; Hendrickson, G., Lyon, L.A.; White, H.S. Resistive Pulse Analysis of Microgel Deformation during Nanopore Translocation. *J. Phys. Chem. C* **2011**, *115*, 2999-3004.

(69) Holden, D.A.; Watkins, J.J.; White, H.S. Resistive-Pulse Detection of Multilamellar Liposomes. *Langmuir*, **2012**, *28*, 7572-7577.

Chapter 2. ELECTROCHEMICAL CHARACTERIZATION OF ULTRATHIN CROSS-LINKED METAL NANOPARTICLE FILMS

This chapter is mostly adapted from the original publication: Han, C.; Percival, S. J.; Zhang, B. "Electrochemical Characterization of Ultrathin Cross-linked Metal Nanoparticle Films" Langmuir, 2016, 32, 8783-8792. DOI: 10.1021/acs.langmuir.6b00710.

2.1 ABSTRACT

Here we report the preparation, characterization, and electrochemical study of conductive, ultrathin films of cross-linked metal nanoparticles (NPs). Nanoporous films ranging from 40 to 200 nm in thickness composed of gold and platinum NPs of ~5 nm were fabricated via a powerful layer-by-layer spin coating process. This process allows preparation of uniform NP films as large as 2×2 cm^2 with precise control over thickness, structure, and electrochemical and electrocatalytic properties. Gold, platinum, and bimetallic NP films were fabricated and characterized using cyclic voltammetry, scanning electron microscopy, and conductance measurements. Their electrocatalytic activity toward the oxygen reduction reaction (ORR) was investigated. Our results show that the electrochemical activity of such NP films is initially hindered by the presence of dense thiolate cross-linking ligands. Both electrochemical cycling and oxygen plasma cleaning are effective means in restoring their electrochemical activity. Gold NP films have higher electric conductivity than platinum possibly due to more uniform film structure and closer particle−particle distance. The electrochemical and electrocatalytic performance of platinum NP films can be greatly enhanced by the incorporation of gold NPs. This work focuses on electrochemical

characterization of cross-linked NP films and demonstrates several unique properties. These include quick and easy preparation, ultrathin and uniform film thickness, tunable structure and composition, and transferability to many other substrates.

2.2 INTRODUCTION

Nanoporous metal films have been under intense investigation due to high surface area and important properties in a number of fields such as fuel cell catalysis[1-4] and highly sensitive chemical sensing.[5-8] Several methods have been used to prepare nanoporous films and these include physical vapor deposition,[9] chemical vapor deposition,[10] and high temperature thermal oxidation.[11] Metal nanoparticles (NPs) can be used to form nanoporous films with unique properties due to their tunable optical, electronic, and catalytic properties.[12] A number of preparation methods have been reported including hard templating,[13,14] dealloying,[15,16] self-assembly,[17-19]and electrochemical deposition.[20,21] Templating and dealloying offer good control over the size and structure of the metal film but they are generally time-consuming and difficult to perform. Electrodeposition can fabricate films of various thicknesses and composition but can only be used on conductive substrates. A conductive substrate, such as glassy carbon,[22,23] carbon nanotubes[24,25] and indium tin oxide (ITO) glass,[26,27] is often needed when NP films are used in electrochemical applications.

Thin film layer-by-layer assembly (LbL) is an attractive approach, and NP films made with LbL can have tunable thickness, morphology, and composition.[28] They can be made by alternating adsorption/deposition of NPs through various interactions such as hydrogen bonding,[29,30] electrostatic interaction,[18,31] and covalent bonding.[32,33] The ability of combining functions of different materials enables their wide application in numerous areas such as selective chemical sensors,[34-36] fuel cells,[37,38] and nanomechanical devices.[39] By introducing different materials into

nanoporous conductive films, one can tune electron and ion transfer properties at nanoscale.[40] Therefore, LbL assembly can be a unique approach in designing nanostructured electrocatalysts with tunable properties.[21,26,41]

Schlicke and co-workers[42] have recently reported a new LbL method for fabricating large, conductive NP films comprised of cross-linked gold NPs. Such films are ultrathin, conductive, and optically semitransparent. Their high surface-to-volume ratio could facilitate interaction between sensor and analytes for high sensitivity. Moreover, large films can be prepared and transferred to other flexible substrates. Based on these advantages, these films could act as both an electrocatalyst and good conductive sensor layer.

Our group[43] and others[44-46] have been interested in electrodes modified by NPs and their use in single-cell neurochemical sensing and electrocatalysis.[47] Most of the previous methods generate electrodes with somewhat random particle distribution and submonolayer coverage. To the best of our knowledge, there have been few or no reports on NP-modified electrodes using closed-packed NP films with well-controlled film thickness, composition, and morphology. Schlicke's method can be an attractive strategy for quick modification of electrodes for these applications because one can have multilayer films and control film composition, structure, and can transfer these to many other substrates. In order to use them for future electroanalytical sensing and electrocatalysis, however, it is necessary to first characterize their basic electrochemical properties. Here, ultrathin, conductive, cross-linked NP films of gold and platinum were prepared by the Schlicke method and thoroughly characterized by electron microscopy, conductance measurements, and cyclic voltammetry. Bimetallic films consisting of alternative layers of gold and platinum NPs were also prepared demonstrating the high level of structure control and the ability to tailor their property. Oxygen Reduction Reaction (ORR) was chosen to evaluate their

electrocatalytic performance because it is considered as the key rate limiting process in most fuel-cell experiments.[2,22,25] The electrocatalytic activity was investigated to understand its dependence on film thickness and composition. Potential cycling and oxygen plasma treatments were both demonstrated as effective methods to clean NP films and eliminate blocking of alkene dithiol ligands on NP surfaces. These treatments greatly improved film conductivity and electrocatalytic activity. In addition to conductive substrates, glass was used as a nonconductive but transparent substrate for NP films. These films could be useful for future experiments involving combined use of electrochemistry and microscopy. In general, our study showed that NP films made by the Schlicke method are attractive electrode materials with unique and tunable nanostructures. They can be easily and quickly prepared to cover very large areas and can be transferred to arbitrary substrates. They have excellent electrochemical properties for both conventional outer-sphere redox species, such as ferrocene and ferricyanide, and inner sphere species, such as oxygen. Gold NP films have better conductivity compared to platinum likely due to more ordered structure and closer particle−particle spacing. Platinum films have superior electrocatalytic activity than gold as expected. We anticipate that these films will have exciting applications in future electroanalytical and electrocatalysis studies.

2.3 Experimental Section

2.3.1 *Chemicals and Materials*

Ferrocene−methanol (FcMeOH, 97%, Aldrich), potassium chloride (KCl, Mallinckrodt Baker), potassium ferrocyanide ($K_4Fe(CN)_6 \cdot 3H_2O$, 99.5%, Fluka), UV photoresist AZ5243 with AZ300 MIF developer (AZ Corporation), polished quartz wafers (Silicon Quest International, Inc.), argon (Ar, > 99%, Praxair), oxygen (O_2, > 99%, Praxair), NaOH pellets (98.5%, J.T. Baker), sulfuric acid (H_2SO_4, Fisher), 1,6-hexanedithiol (HDT, 99.5%, Aldrich), gold chloride trihydrate

($HAuCl_4 \cdot 3H_2O$, ≥ 99.9%, Aldrich), oleylamine (70%, Aldrich), tetrabutylammonium bromide (97%, Aldrich), chloroplatinic acid hydrate ($H_2PtCl_6 \cdot xH_2O$, ≥ 99.9%, Aldrich), tetraoctylammonium bromide (98%, Aldrich), methanol (Aldrich), acetone (Aldrich), acetonitrile (Aldrich), sodium borohydride ($NaBH_4$,98%, Aldrich), Nafion 117 solution (Aldrich) were used as received. All aqueous solutions were prepared using deionized water (>18 MΩ cm) obtained through a Barnstead Nanopure water purification system.

2.3.2 *Preparation of Gold Nanoparticles*

The oleylamine-capped Au NPs were synthesized according to a previously published procedure.[48] At first a precursor solution of 10 mL toluene, 10 mL oleylamine, and 0.1 g $HAuCl_4 \cdot 3H_2O$ was prepared at room temperature. A reducing solution containing 0.5 mmol of tetrabutylammonium bromide, 1 mL toluene, and 1 mL oleylamine was mixed and injected into the precursor solution. The mixture was allowed to react at room temperature for a while and then 60 mL acetone was added to the mixture to precipitate the particles. The Au NPs were collected by centrifugation (Fisher Scientific accuSpin 400) at 7500 rpm for 5 min, washed with acetone twice and dispersed in heptane. The concentration of the Au NP solution is about 0.02 mM.

2.3.3 *Preparation of Platinum Nanoparticles*

The oleylamine-capped Pt NPs were synthesized from the procedure in a previously published paper.[49] A mixture of 30 mL 10 mM $H_2PtCl_6 \cdot 6H_2O$ aqueous solution and 70 mL toluene was stirred for 30 min at room temperature. 60 mM tetraoctylammonium bromide in 10 mL toluene was added as a phase transfer reagent in toluene. 150 mM oleylamine in 10 mL toluene and 30 mL 200 mM $NaBH_4$ aqueous solution were added to the solution. The reaction mixture was vigorously stirred overnight. The organic layer was separated, and acetonitrile was added. After centrifugation

at 7800 rpm for 8 min, the precipitate was collected and dispersed in heptane. The concentration of the Pt NP solution is about 0.02 mM.

2.3.4 *Scanning Electron Microscope (SEM) Imaging*

Au films were transferred to a silicon chip (Silicon Quest International, Inc.) for SEM imaging. SEM images were obtained using a field-emission SEM (FEI Sirion XL30) operating at 20 kV accelerating potential equipped with a through lens secondary electron detector with a resolution of 1−3 nm.

2.3.5 *Transmission Electron Microscope (TEM) Imaging*

Au and Pt nanoparticles were transferred to a carbon-coated TEM grid (Ted Pella, Inc.) for TEM imaging. TEM images were obtained using a FEI Tecnai G2 F20 TEM under 200 kV with a single-tilt sample holder. Examples of the nanoparticles can be seen in Figure 2.1along with the measured size distribution histograms. The oleylamine-capped Au nanoparticles have uniform spherical shape and the average size is 5 nm in diameter. Some of Pt nanoparticles were more rod shaped and the particle size was measured along the longest length axis. The size of the Pt particles, shown in Figure 2.1D, were found to have a large proportion of particles that were ~3 nm (mostly spherical particles) with some that were larger (rod shaped particles). The histogram is seen to tail off at larger lengths with decreasing proportions of particles, up to ~ 12 nm in length.

2.3.6 *Oxygen Plasma Cleaning*

Oxygen plasma treatment was done by a Diener-Femto oxygen plasma cleaner with a power of 40 W and oxygen pressure of 140 mbar.

2.3.7 *Electrochemical and Conductance Measurements*

All electrochemical experiments were performed by using a standard three-electrode configuration with a Pt-wire counter electrode and a commercial Ag/AgCl reference electrode (Bioanalytical Sciences, Inc.) or a commercial Hg/Hg_2SO_4 reference electrode (CH Instruments, Inc.). Cyclic voltammetry and conductivity tests were performed using a bipotentiostat (Pine AFCBP1). Data were recorded using an in-house virtual instrumentation program written in LabView (National instruments) on a desktop PC equipped with a PCI-6251 (National Instruments) data acquisition card. Solutions for ORR testing were bubbled with oxygen or argon for over 20 min before use. Glassy carbon electrodes (GCE, 3 mm in diameter, Bioanalytical Sciences, Inc.) were polished and sonicated in water for several minutes. The electrodes were then rinsed with water and methanol and dried under nitrogen airflow. A piece of the freestanding film was picked up by a Pt micro ring from water surface and transferred to a GCE surface. The film was allowed to dry under room temperature. For ORR experiments, 10 μL diluted Nafion solution was applied on top of the electrodes to provide stability to the coated surfaces. After O_2 plasma cleaning, the film-coated glass was cut into 6 pieces by a diamond knife and made contact with tungsten wire and Ag paste. The exposed edges were encased in the same epoxy used to insulate the contacts so that only the flat face of the nanoparticle film would contribute to the electrochemical current. Each piece is treated as an individual electrode when evaluated with the outer-sphere redox molecules or for the ORR activity. When performing ORR experiments, 20 μL of 0.5% Nafion solution was applied on top of the electrodes and allowed to dry in order to provide stability to the coated surfaces.

2.3.8 *XPS Analysis*

All XPS spectra were taken on a Surface Science Instruments S-Probe photoelectron spectrometer. This instrument has a monochromatized Al Kα X-ray source, which was operated at 20 mA and 10 kV, and a low energy electron flood gun for charge neutralization. The samples were spin coated onto glass coverslips in the same manner as previously described. X-ray analysis area for these acquisitions was approximately 800 μm across. Pressure in the analytical chamber during spectral acquisition was less than 5×10^{-9} Torr. Pass energy for survey and detail spectra (to calculate composition) was 150 eV. Data point spacing was 1.0 eV/step for survey spectra, and 0.4 eV/step for detailed spectra. Pass energy for high resolution spectra was 50 eV. Data point spacing was 0.065 eV/ step for high resolution spectra. The takeoff angle (the angle between the sample normal and the input axis of the energy analyzer) was 0°, (0° takeoff angle ≅ 100 Å sampling depth). Service Physics Hawk version 7 data analysis software was used to calculate the elemental compositions from peak areas and to peak fit high-resolution spectra. An inelastic scattering (Shirley) background was used.

2.3.9 *Film Resistance Test*

The change in film resistance before and after oxygen plasma treatment was tested by attaching evaporated gold electrode leads to the film. First, the chips were spin coated with an adhesion promoter (Micro Prime MP-P20 (20% hexamethyldisilazane (HMDS), 80% propylene glycol monomethyl-ether acetate (PGMEA)), then with a ~2 um-thick layer of photoresist (AZ5214E, AZ Corporation). These were then exposed using a UV mask aligner (Newport). The exposed chips were then developed and gold contacts (50 nm of gold with 5 nm of chrome) evaporated onto the patterned chips using an in-house metal evaporator. The chips were placed in acetone overnight for metal lift-off. The electrodes had a 500 μm spacing between the two leads

but calculation of the film resistivity was not done because of the variable nature (size and shape) of the transferred films. Instead the resistance of the films and the resulting resistance change after oxygen plasma was determined for the different composition films.

To test the relative resistance of the different composition films, the freestanding films $(Au)_{10}$, $(Au\text{-}Pt)_{10}$ and $(Pt)_{10}$ were transferred by the micro ring to Au electrode respectively and allowed to dry at ambient conditions. Then the film was treated by O_2 plasma for 12 min, which is the optimal time for $(Au)_{10}$ film (discussed in the main text). These films show linear and stable Ohmic current–voltage (I-V) characteristics, as shown in Figure 2.9, where the applied potential between the source and drain electrodes was scanned repeatedly up to ± 10 volts. The corresponding optical image of the sample is also shown with the current-voltage sweeps in Figure 2.9. The current is seen to increase after plasma treatment for all of the samples. The (Au)10 film shows a resistance of 385 kΩ but after O_2 plasma cleaning, the resistance decreased to 21 kΩ. For the $(Au\text{-}Pt)_{10}$ bimetallic and (Pt)10 films their total resistances were 19,570 kΩ and 5,073,000 kΩ respectively before oxygen plasma treatment and 387 kΩ and 5425 kΩ after oxygen plasma treatment, respectively. This leads to an approximately 51-fold decrease and a 935-fold decrease in the total resistance for the $(Au\text{-}Pt)_{10}$ and $(Pt)_{10}$ films, respectively. The resistance of the bimetallic film was expected to increase because half of the layers were changed from gold to platinum and bulk platinum naturally has a lower conductivity than gold. Additionally, with the presence of the platinum nanoparticles with different shapes and sizes, the resulting film could have voids and defects inside the film, changing the film morphology from an ordered close packed film leading to a further increase in the film resistance. The $(Pt)_{10}$ film has the lowest conductivity even after O_2 plasma treatment where its resistance is larger than that of $(Au)_{10}$ by several orders of magnitude.

2.4 Results and Discussion

2.4.1 *Preparation of Nanoparticle Films*

Gold NP films were prepared according to a previously published procedure with modification.[42] Oleylamine-capped NPs were used instead of dodecylamine-capped NPs, and to obtain a uniform film a different amount of NP solution was used. Glass coverslips were first cleaned with water and ethanol in an ultrasonic bath and dried under a flow of nitrogen. As shown in Figure 2.2, a coverslip was spin coated (Specialty Coating Systems Inc., Model P6700 Series) at 3000 rpm. First a 15 μL drop of Au NP solution was added to the center of the rotating substrate followed by 2 aliquots of 15 μL of 7.4 mM 1,6-hexanedithiol (HDT) in methanol. Together, the NP solution and 2 aliquots of HDT are regarded as one complete spin coating cycle. Oleylamine ligands are only weakly bound to the particles and are efficiently replaced by dithiol, which also serves to cross-link the nanoparticles together. This is supported by the XPS results presented below. The spin coating cycle was repeated until the desired film thickness was reached and a 30 s waiting period was always used after each cycle. The resulting films were labeled as $(Au)_n$ where n is the number of spin coating cycles. NP films of Pt and Au/Pt bimetallic films were prepared using the same spin coating procedure as for the Au films. The $(Au{-}Pt)_{10}$ bimetallic films were prepared by alternately coating the substrate with Au and Pt NPs until the total number of layers reached 10 with Au as the initial layer and Pt as the topmost layer. Both Au and Au/Pt bimetallic films can be easily detached from the glass surface by floating on the surface of a basic solution of 0.1 M NaOH overnight and the detachment is believed to be caused by slow etching of the glass by OH^-. The NP film can be found to freely float on the water−air interface, which can be easily picked up by a Pt microring and transferred to a glassy carbon electrode or other desired substrates. Figure 2.3 shows a photo of a Pt microring used to transfer NP films.[50] Alternatively, the film can

be cleaned with oxygen plasma and subsequently cut into pieces to be used as individual electrodes. An optical image is also included in Figure 2.2, showing an electrically contacted, semitransparent NP film on glass.

2.4.2 *Scanning Electron Microscope (SEM) Imaging*

Gold NP films of different thicknesses ($(Au)_n$, n = 5, 7, 10, 12, 15), $(Au{-}Pt)_{10}$, and $(Pt)_{10}$ were transferred onto a silicon chip and allowed to dry under room temperature. These films were carefully scratched by the tip of a sharp tweezer. In certain areas, the broken films were found to bunch up into a stack, as shown in Figure 2.4. An SEM image of a large piece of $(Au)_{10}$ film can be seen in Figure 2.5, where the red arrows point to the scratched area. Figure 2.5B shows a $(Au)_5$ film imaged at higher magnification, which clearly resolves individual nanoparticles. Figure 2.5C shows the edges of a scratched $(Au)_{12}$ film. Each piece has a relatively uniform thickness, ~ 85 nm, along its entire length. The thickness of each film is determined by repeatedly measuring from the exposed edges of several samples and the average film thickness is shown in Figure 2.5D.

The film thickness of the $(Au)_n$ sample shows a linear relation with the number of deposition cycles, as expected. The slope of fitted line is around 8.1 nm/cycle. indicating that each deposition cycle results in an addition of about 8 nm in film thickness. This increase is about 60% greater than the average diameter of the gold NPs measured from TEM, which may be caused by the additional thickness of the thiol molecules and the non-uniform arrangement of particles. The $(Pt)_{10}$ film has a thickness of 195.9 nm, which is nearly 5 times of the predicted film thickness based on the size of the Pt NPs. We believe this is mainly due to the lack of uniformity in particle arrangement in such films possibly due to a weaker thiol-Pt interaction, non-spherical shape of Pt particles, and the less ordered thiol monolayers on Pt NP surfaces.[51] The $(Au{-}Pt)_{10}$ film that has 5 layers of Au and 5 layers of Pt had a measured thickness of 128.9 nm, which is more than the

$(Au)_{10}$ film (81.2 nm) but less than that of the $(Pt)_{10}$ film. The relatively large film thickness of Pt containing films may reflect more voids and defects in such films.

2.4.3 *XPS Analysis*

The formation of the film by cross-linking Au nanoparticles was also supported in XPS analysis. Figure 2.5E shows the S_{2p} high-resolution spectrum from the sum of the scans taken at one spot on the $(Au)_{10}$ nanoparticle film. The S_{2p} spectrum was fit with two doublets. One of the doublets at a binding energy of around 164 eV with a 2:1 ratio and 1.2 eV splitting is attributed to the presence of unbound thiol groups, while the additional doublet at a lower binding energy (around 162 eV) is attributed to the presence of bound dithiol molecules to Au nanoparticle surface.[52] Furthermore, one may notice that the amount of bound dithiol molecules is higher than those of the unbound dithiol molecules, even though there are lots of unbound thiol group on the top surface of $(Au)_{10}$ NP film. The result is consistent with those from the spectra of the other two spots. This indicates that most of the thiol ligands in the film were present in the form of Au-thiol bond thus supporting our claim that the metal NPs were cross-linked by dithiol molecules.

2.4.4 *Electrochemical Characterization*

Cyclic Voltammetry (CV) of simple outer sphere redox molecules, such as FcMeOH and $Fe(CN)_6^{4-}$, was used to further characterize $(Au)_{10}$ films. The sample films were first treated with oxygen plasma cleaning for 12 min to eliminate blockage of redox species from thiolate ligands. Three different film samples were investigated, which include $(Au)_{10}$ films on a gold coated (25 nm Au) glass substrate with and without O_2 plasma cleaning, and plasma cleaned $(Au)_{10}$ film directly supported on glass. The $(Au)_{10}$ film electrode on glass showed no apparent faradaic signal prior to plasma cleaning due to the poor film conductivity (along the glass surface) but well-

defined CVs characteristic of a diffusion-limited redox process after plasma activation. Figure 2.6A shows CVs of an activated $(Au)_{10}$ film electrode on glass at various scan rates in 2 mM FcMeOH and Figure 2.6B shows CVs from the same sample but in $Fe(CN)_6^{4-}$. It can be seen that the peak current increases as the scan rate is increased, as expected. The peak current was plotted to the square root of the scan rate, $\nu^{1/2}$, in Figure 2.6C, D. The peak current density was obtained from the geometric area of the films and compared to the calculated peak current density from the Randles−Sevcik equation,[53]

$$i_p = (2.69 \times 10^5) n^{3/2} A D^{1/2} C \nu^{1/2} \quad (2.1)$$

where n is the number of electrons, A is the area of the electrode, D is the diffusion coefficient (6.7×10^{-6} cm^2/s for FcMeOH and 6.88×10^{-6} cm^2/s for $Fe(CN)_6^{4-}$),[54,55] and C is the redox concentration. For both redox molecules, the untreated films had peak currents which deviate quite strongly from the prediction according to eq 2.1 and are smaller than the plasma cleaned samples, whether on gold or glass. This is due to strong inhibition from the dithiol linker molecules coating the Au NP surfaces acting as a barrier for electrons and redox molecules.[56] The plasma treatment effectively oxidizes and removes the dithiol molecules to expose the gold surfaces. In FcMeOH, the peak current density matches very closely with that calculated from the Randles-Sevcik equation. The good agreement indicates a diffusion controlled redox process. In $Fe(CN)_6^{4-}$ solution the peak current of the plasma cleaned electrodes deviate more strongly from the calculated values likely due to electrostatic effects from the negatively charged redox molecule and the negative charges on the gold NPs.[57] The peak current density of $(Au)_{10}$ electrode on glass is always smaller than that on the gold substrate. This may be due to a large distance that electrons have to travel in glass-supported films and a higher internal film resistance. Particles located far from the contact point experience less driving voltage due to ohmic voltage drop in the film.

Therefore, they participate less effectively in electrochemical reactions than particles close to the contact point. This ohmic drop is greatly eliminated or completely removed when glassy carbon is used as the substrate because of significantly reduced electron pathway from the conductive glassy carbon to the surface of the NP film.

Figure 2.6E, F shows plots of the peak separations, ΔE_p, as a function of scan rate for FcMeOH and $Fe(CN)_6^{4-}$, respectively. ΔE_p increases with scan rate for all of the $(Au)_{10}$ electrodes. However, some clearly have larger peak separations than others. The values ($\Delta E_p > 59$ mV) indicate a quasi-reversible redox process.[53] For FcMeOH, ΔE_p on the uncleaned gold-supported $(Au)_{10}$ film steadily increased with scan rate, but after plasma cleaning the ΔE_p was much larger at all scan rates. The ΔE_p for plasma cleaned glass-supported $(Au)_{10}$ film increased with scan rate and was similar to that on gold but had slightly larger peak separations due to a larger film resistance on glass. The fact that the ΔE_p was the lowest for the uncleaned $(Au)_{10}$ on gold was surprising but is likely due to the slight hydrophobicity of the FcMeOH where it preferentially interacted with the organic dithiol ligands.[56] The change in ΔEp in $Fe(CN)_6^{4-}$ was observed to decrease after plasma cleaning for gold-supported samples because of a change in the hydrophobicity caused by the plasma treatment.[58] McCreery has shown previously that $Fe(CN)_6^{4-}$ is a surface sensitive redox molecule and that the ΔE_p of $Fe(CN)_6^{4-}$ can easily be affected by the presence of adsorbed molecules on the electrode surface.[59] Removal of the thiolate ligands allows the $Fe(CN)_6^{4-}$ to more easily interact with the nanoparticle surface leading to an increased electron transfer rate.

2.4.5 *Film Activation*

Our initial testing on untreated NP films showed poor catalytic activity toward ORR because of the thiolate molecules blocking active sites. The film electrodes were potential cycled

in both 0.5 M H_2SO_4 and in 0.1 M NaOH to activate their catalytic activity. Potential cycling is a commonly used procedure in electrochemistry to clean electrodes to remove surface bound contaminants.[60] An example of the potential cycling can be clearly seen in Figure 2.7A where a piece of $(Au)_{10}$ film supported on glassy carbon was cycled continuously in Ar-purged 0.1 M NaOH[61] or 0.5 M H_2SO_4.[62] An oxidation wave can be seen starting at ~0.7 V on the anodic scan and a reduction peak at 0.4 V on the reverse scan. The oxidation wave is attributed to the oxidative desorption of thiolate and formation of gold oxide and the reduction peak is mainly due to the subsequent reduction of the Au oxide.[63] The Au oxide reduction peak increases from each potential cycle indicating increased exposure of Au surfaces.[63] The goal was to obtain a highly active surface with as much electroactive surface area as possible.[64] So, from each potential cycle, the electroactive area of the film was calculated from the integrated peak area (Au reduction charge 400 $\mu C/cm^2$)[43] and the roughness factor determined (ratio of electroactive area to geometric area [2,53]) for each potential cycle.

Figure 2.7B shows how the roughness factor changes with potential cycling for two sample film electrodes (one each in acidic and alkaline solution). The large roughness factor is related to the highly porous nature of the film. In both acidic and alkaline solution, it shows an increasing trend at first, but after a number of cycles the film starts to lose active area possibly due to nanoparticle sintering.[65,66] In H_2SO_4 it takes far less potential cycles to reach the peak roughness of 25.5, which has a larger value than the peak roughness of 9.9 in NaOH (Figure 2.8), which takes many more cycles to reach. This indicates that cycling in H_2SO_4 is more efficient in eliminating dithiol ligands before NPs sintering. Potential cycling in H_2SO_4 was chosen as the procedure to perform all further activations. The number of potential cycles was expected to depend on the film thickness. As such, the number of cycles to obtain the maximum electroactive area for each film

thickness was determined, as seen in Figure 2.7C. With the same scan rate and same potential scan window, the number of cycles required to obtain the largest roughness factor is positively correlated with film thickness. This determined the number of cycling for each film thickness when testing the ORR activity.

Potential cycling can sometimes be difficult to control and may lead to the particles sintering. Moreover, the procedure cannot be easily used on insulator-supported films and a conductive substrate, such as glassy carbon, needs to be used. For these reasons, O_2 plasma was also used to activate the film. By varying O_2 plasma time duration, using the same oxygen gas pressure, the cleaning procedure is easily controlled without changing the morphology and structure of the nanoparticle film. With O_2 plasma treatment dithiol molecules are oxidized and removed in the gas, which not only expose more catalytically active sites on nanoparticles but also significantly increases the film conductivity (Figure 2.9). Because of the increased conductivity the NP film-coated glass can be treated as individual electrodes for ORR catalysis.

The current density for the ORR in 0.5 M H_2SO_4 was used to evaluate the effectiveness of the plasma cleaning, as seen in Figure 2.7D. For all film electrodes tested ($(Au)_5$, $(Au)_{10}$ and $(Au)_{15}$) the current density is seen to increase with increased cleaning time and plateaus to the similar current density of ~760 $\mu A/cm^2$. This result shows that only the outermost layers of the films are active for ORR leading to the same current density regardless of the number of layers. This is because those NPs at top layers are active in catalysis, while those buried deeply are less active.[26] However, the smallest amount of time required to reach this max current density differs from each thickness and was 7 min for $(Au)_5$, 12 min for $(Au)_{10}$, and 15 min for $(Au)_{15}$. These cleaning times were used for the rest of the experiments on the glass-supported NP films. Notably, the current density at the different thicknesses deviates a lot at first several minutes from each other. This is

attributed to the increased the amount of ligands present that slow their complete removal from the surface and the film resistance. In the first several minutes, the top layer is partially cleaned, and ORR current density is restrained by both film resistance and exposed active area. As time increases, the top layer is fully cleaned and film resistance becomes the main limiting factor. This shows that O_2 plasma treatment is a useful method for cleaning and activating NP films on unreactive glass insulator substrates.

2.4.6 *Oxygen Reduction Reaction (ORR) on NP Films*

A glassy carbon electrode was used as a conductive substrate to compare the activity of the different types of Au NP films. NP films were potential cycled in Ar-saturated 0.5 M H_2SO_4 as described previously prior to ORR experiments. The electroactive surface area was calculated from the Au reduction peak. Figure 2.10A shows a typical CV of $(Au)_{10}$ in an Ar-saturated and oxygen-saturated 0.5 M H_2SO_4 solution. A large reduction wave can be seen in the O_2-saturated solution starting at ~100 mV that is absent from the Ar-saturated solution which is due to the catalytic reduction of oxygen on the NP surface. This wave is seen to reach a steady-state current and at around −200 mV, the cathodic current is again seen to increase, but this is attributed to the reduction of oxygen on the GCE surface. A typical ORR CV of a bare GCE can also be seen in Figure 2.10A. The cathodic ORR wave is seen to begin at −150 mV. The NP films would not entirely cover the GCE surface in order to accurately determine their activity on a conductive substrate. The ORR current was normalized by geometric area and electroactive area to obtain their respective current densities, j_{geo} and j_{EA}. Figure 2.10B shows how the current densities change with film thickness. The j_{geo} was observed to increase with film thickness, while an opposite trend was observed for the j_{EA}. More NP layers increase the amount of surface area leading to a higher electroactive area. This, however, will lead to a decrease in j_{EA} because only the outermost layers

are effectively catalyzing the reaction. The j_{geo} increases to a plateau for the same reason, i.e., the outermost layers are the most accessible for the diffusing oxygen molecules.

Besides the pure gold NP films, Pt films, and Au-Pt bimetallic films were characterized for their ORR behavior. The overall film thicknesses were kept at 10 layers as this was the most tested thickness and the layers in the bimetallic film could be alternated with a final composition of equal spin coating cycles of gold and Pt NPs. Potential cycling in H_2SO_4 was used for film activation for all samples, however, the electroactive area for Pt was estimated from the hydrogen adsorption peak using the average charge density of 210 μC/cm.[2,67] Figure 2.10C shows representative cathodic sweeps from GCE-supported $(Au)_{10}$, $(Au{-}Pt)_{10}$, and $(Pt)_{10}$ films. Similar to Figure 2.10A there is one large cathodic wave for each trace. However, the films containing the Pt NPs displayed a secondary cathodic wave, which is due to the proton adsorption on Pt as seen in Figure 2.11. The incorporation of Pt NPs markedly improved the ORR activity for the $(Au{-}Pt)_{10}$ bimetallic film. The $E_{1/2}$ was shifted from 0.003 V on the $(Au)_{10}$ film to 0.467 V on the bimetallic film and the current densities were observed to increase. The $(Pt)_{10}$ had the highest activity with the most positive $E_{1/2}$ and largest current density, as expected. The results for ORR testing from all the different films are listed in Table 2.1. The half wave potential of $(Au{-}Pt)_{10}$ is close to that of state-of-art Pt/C catalyst (0.5 V vs Ag/AgCl), indicating that $(Au{-}Pt)_{10}$ has a high catalytic activity toward the ORR.[68]

The ORR activity was also tested on glass-supported NP films after plasma activation. As shown in Figure 2.12A, before plasma cleaning, the catalytic activity of a glass-supported $(Au)_{10}$ film was low. After cleaning, a well-defined reduction wave for oxygen starting at 0.059 V versus Ag/AgCl was observed. The initial lack of substantial ORR current is not only due to the presence of surface blocking ligands but also poor in-film electrical conductance. Plasma cleaning not only

exposed more Au surfaces but also drastically improved the film conductivity. The ORR activity of the Au films on glass was lower than on the GCE as seen from both $E_{1/2}$ and geometric current density (the electroactive surface area could not be accurately determined for glass-supported films as the film would break apart with very high potential cycling). The different activities between the GCE-supported and glass-supported gold films can be seen in Table 2.2.The larger ORR overpotential and the lower current density seen on the glass-supported samples are due to significant film resistance.

Figure 2.12B shows how NP film composition affects the ORR activity when films are supported on glass. A surprising revelation was that by changing the composition from Au NPs to Pt NPs there was an almost complete elimination of the catalytic activity. In fact, the CV of the pure $(Pt)_{10}$ film (even after 12 min O_2 plasma cleaning) looks like a purely resistive i-V response (Figure 2.13). The $(Pt)_{10}$ has such a poor activity due to its low conductivity on glass substrate, as shown in Figure 2.9. The combination of Au and Pt in the $(Au{-}Pt)_{10}$ bimetallic film on glass turned out to be the most active composition on glass ($E_{1/2}$ and current density), of the three tested, with an obvious positive shift in the $E_{1/2}$ of ~0.43 V as compared to the $(Au)_{10}$ film. We believe this is due to the mixture of the high catalytic properties of Pt NPs and the highly conductive properties of the Au NPs within the same film. It is obvious from simple conductivity tests of the three film compositions (Figure 2.9) that the proportion of gold within the film will directly affect its relative sheet resistance. In the bimetallic film the superb catalytic activity of Pt and excellent conductivity of Au are united to obtain a highly active electrocatalyst on an insulating substrate, which displays much higher activity than either of the components alone. This simple result demonstrates the idea of a tunable NP film where the resulting films properties will be a result of the constituents incorporated into it.

2.5 CONCLUSIONS

In summary, we have presented the preparation, characterization, and electrochemical and electrocatalytic studies of ultrathin cross-linked metal nanoparticle films. The use of a layer-by-layer spin-coating process ensures that the thickness, composition, and electrochemical properties of the nanoparticle films can be precisely tailored. These ultrathin, freestanding films can be transferred to many other substrates such as glassy carbon, glass, and plastic. Two methods of film cleaning and activation were tested including potential cycling and O_2 plasma treatment. Both activation procedures lead to greatly enhanced electrocatalytic activity. The electrocatalytic activity toward ORR was evaluated for films supported on both glassy carbon electrode and glass. NP films containing pure Pt NPs showed the best catalytic activity, but the Au films were more conductive, likely due to more ordered structure and closer spacing between particles. These NP films are highly porous, stable, semitransparent, conductive, and can be easily made over large areas and transferred to other substrates, therefore they are expected to have exciting potential in future electroanalytical and electrocatalytic applications.

2.6 TABLES AND FIGURES

Table 2.1. Data showing the differences between ORR catalytic activity of different films on different substrates including $E_{1/2}$, E_p, j_{GEO} and j_{EA}

Electrode-substrate	j_{geo} (μA/cm^2)	j_{EA} (μA/cm^2)	E_p (mV)	$E_{1/2}$ (mV)
$(Au)_{10}$-GCE	917.1 ± 59.1	34.2 ± 3.7	-117 ± 5	3 ± 5
$(Au\text{-}Pt)_{10}$-GCE	1206.5 ± 62.8	51.6 ± 5.3	329 ± 10	458 ± 16

$(Pt)_{10}$-GCE	1312.9 ± 83.4	65.8 ± 7.5	354 ± 9	473 ± 13
$(Au)_{10}$-glass	757.2 ± 20.5	-	-198 ± 5	-77 ± 7
$(Au\text{-}Pt)_{10}$-glass	621.4 ± 117.6	-	111 ± 80	362 ± 43
$(Pt)_{10}$-glass	1.9 ± 1.0	-	-200	-

E_p refers to the potential where the respective peak current densities were measured. Films on GCE were activated by potential cycling and films on glass insulator were activated by O_2 plasma.

Table 2.2. Table with the $E_{1/2}$, j_{GEO} and the average geometric film areas from the $(Au)_5$, $(Au)_{10}$, and $(Au)_{15}$ films on both GCE and glass insulator

Au NP Film "Thickness"	Glassy Carbon Electrode			Glass Insulator		
	$E_{1/2}$ (mV)	j_{geo} (μA/cm^2)	Area (cm^2)	$E_{1/2}$ (mV)	j_{geo} (μA/cm^2)	Area (cm^2)
$(Au)_5$	1 ± 17	600.1 ± 65.0	0.042 ± 0.008	-71 ± 6	760.5 ± 54.3	0.644 ± 0.018
$(Au)_{10}$	3 ± 5	917.1 ± 59.1	0.029 ± 0.005	-77 ± 7	757.2 ± 20.5	0.545 ± 0.016
$(Au)_{15}$	-3 ± 6	997.5 ± 45.3	0.031 ± 0.008	-86 ± 4	760.7 ± 25.0	0.587 ± 0.023

The current densities and half wave potentials for oxygen reduction measured from Au NP films on GCE and glass supports are listed in Table S1. The films on GCE were cleaned by potential cycling and the films on glass insulators were all cleaned by oxygen plasma cleaning.

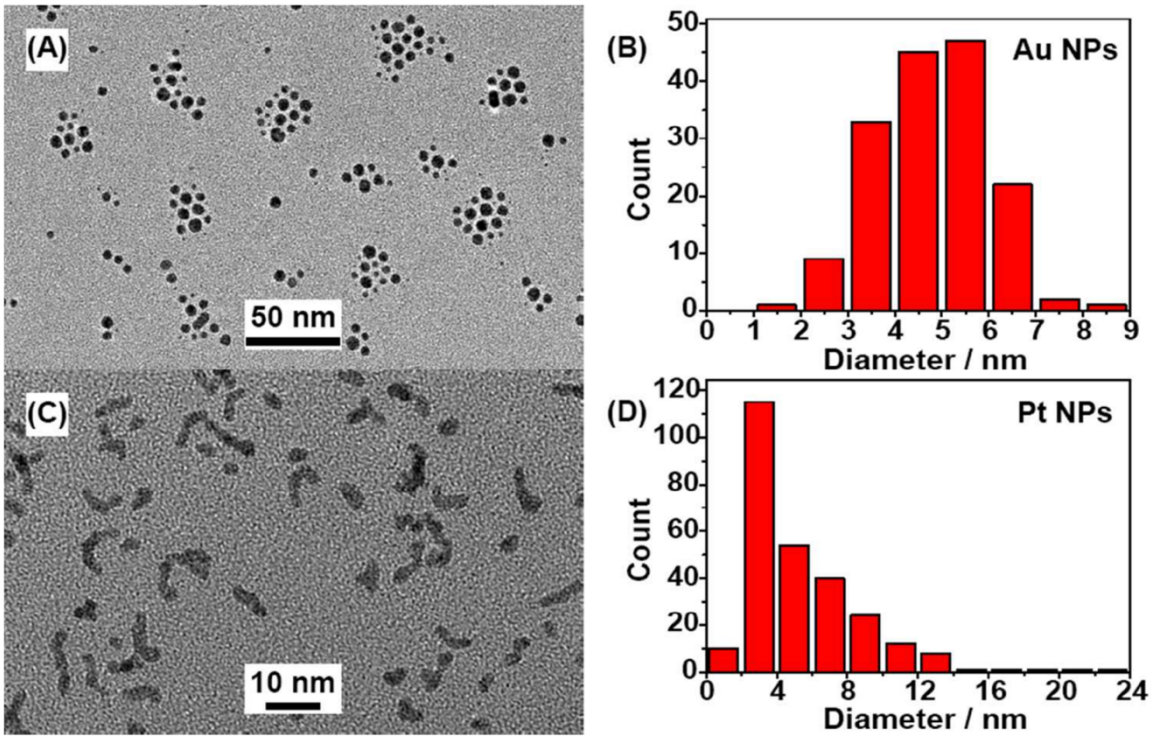

Figure 2.1. TEM images of Au and Pt nanoparticles and particle size distribution

TEM images of the gold nanoparticles (A) and the platinum nanoparticles (C) used in the fabrication of nanoparticle films with particle size distributions shown in (B) and (D).

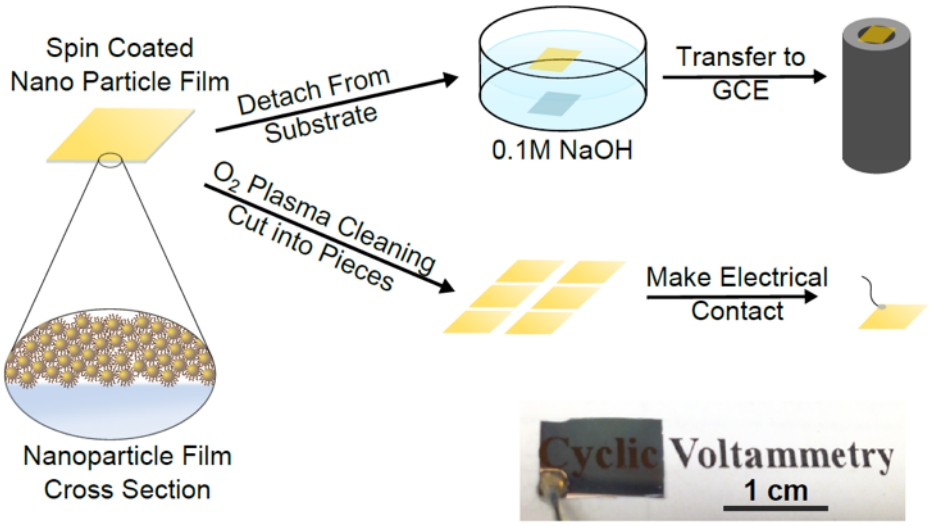

Figure 2.2. Schematic depicting the fabrication of NP film

The schematic depicts the difference uses of a NP film spin coated onto glass coverslip where the NP film can be detached from the substrate and transferred to an electrode or the film cleaned in oxygen plasma followed by cutting the substrate with the attached film into pieces to be used as individual electrodes. Also seen is an optical micrograph of a semi-transparent, glass supported NP film.

Figure 2.3. A Pt micro ring

The floating nanoparticle film was transferred to a substrate by a mirco ring. 0.5mm platinum wire was wound to a loop (~4 mm in diameter), as shown in the picture.

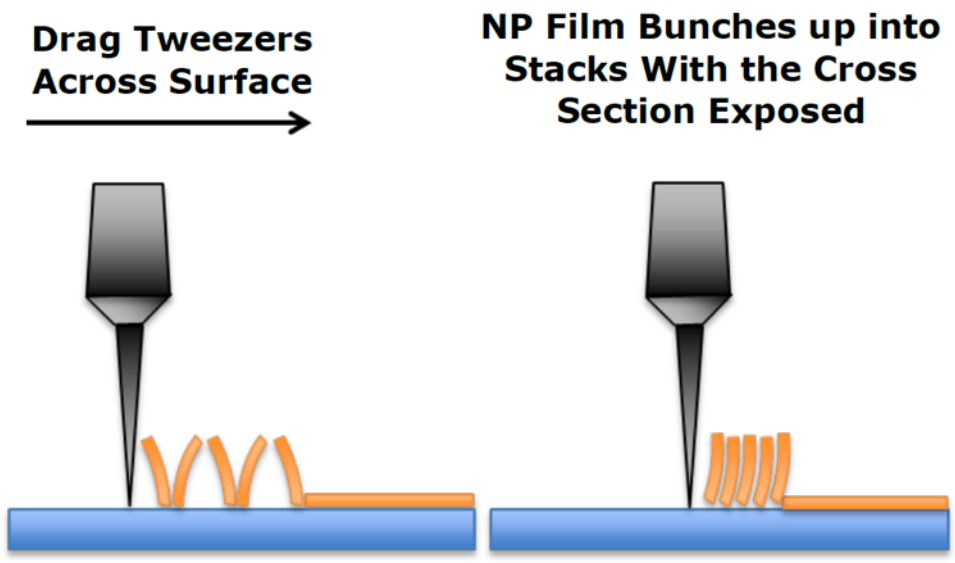

Figure 2.4. Schematic depicting sample preparation for SEM imaging

A sharp tweezer tip was lightly scratched across the film which resulted in broken and stacked film pieces. The exposed film cross sections were then imaged using SEM.

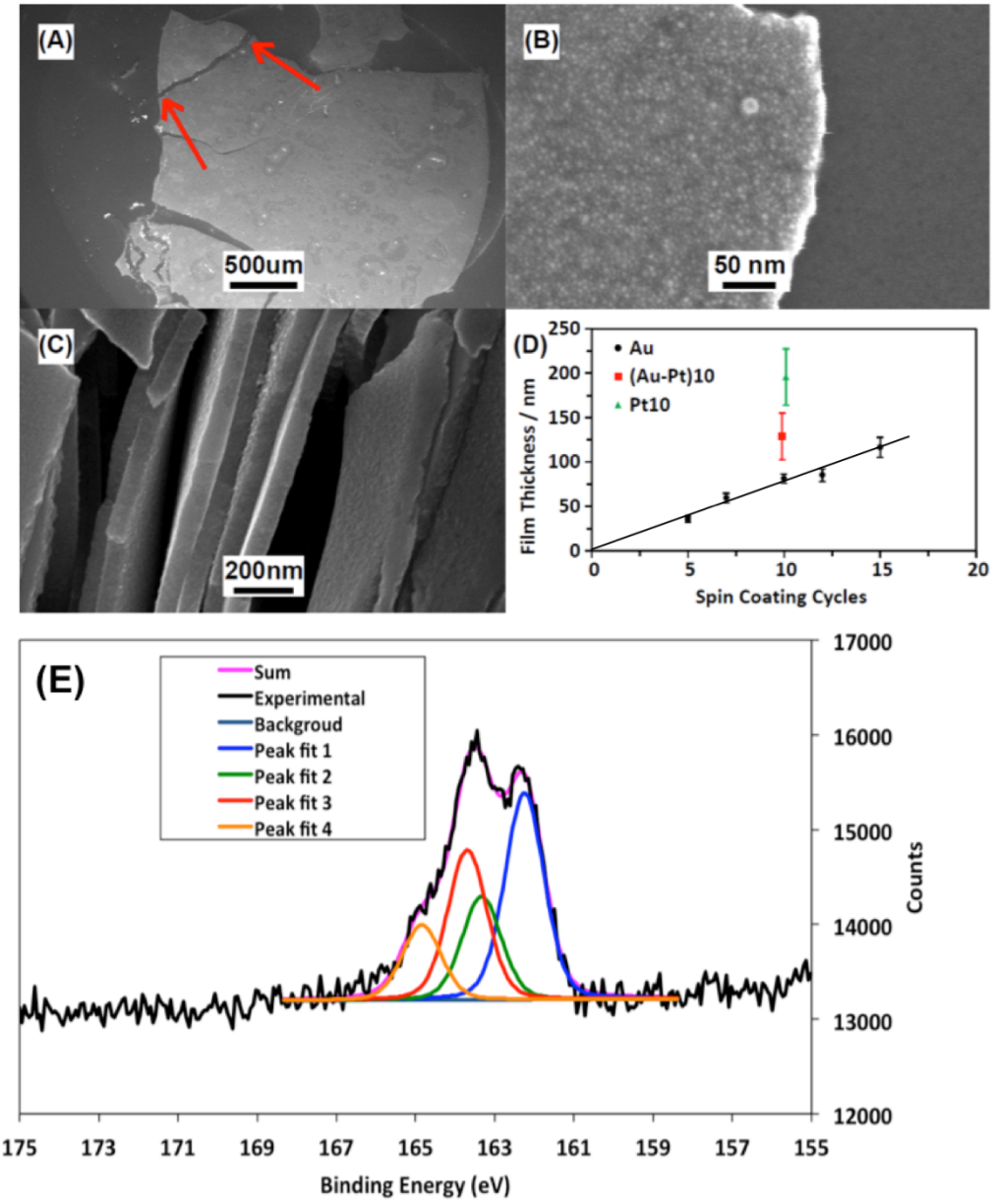

Figure 2.5. SEM imaging and XPS characterization

(A) SEM of a large $(Au)_{10}$ film on a bare silicon chip used to measure the film thickness. The red arrows point to the beginning and end of a scratch made in the film. (B) SEM image of a $(Au)_5$ film imaged at high magnification. (C) SEM of a $(Au)_{12}$ film showing the edges of the broken film. (D) Film thicknesses versus the number of spin coating cycles for gold films. The plot also includes data for $(Au\text{-}Pt)_{10}$ and $(Pt)_{10}$. (E) S_{2p} XPS spectra of $(Au)_{10}$ film. The black trace shows the experimental data. The colored lines show the deconvolution fits.

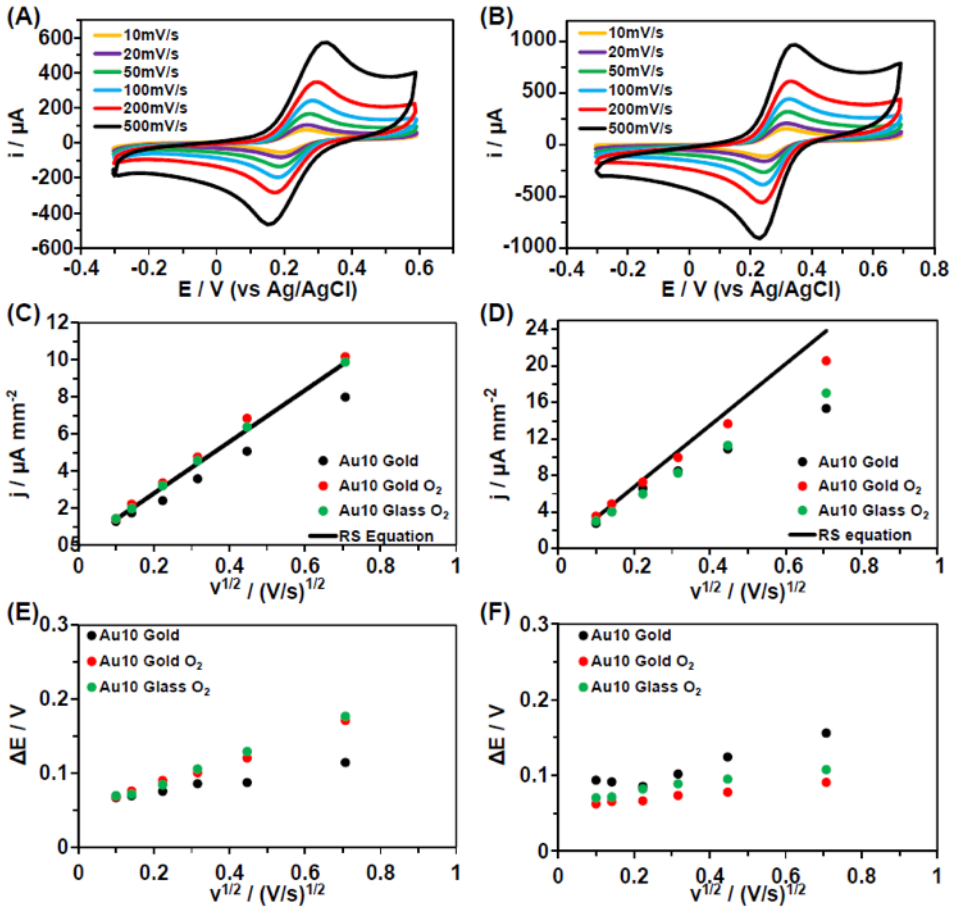

Figure 2.6. CVs of NP film in FcMeOH and $Fe(CN)_6^{4-}$

CVs of (A), (C), (E) 2 mM FcMeOH in 0.1 M KCl and (B), (D), (F) 5 mM $Fe(CN)_6^{4-}$ in 1.5 M KCl on Au NP films on different substrates. The example CVs shown in (A) and (B) were taken using a glass-supported $(Au)_{10}$. All the electrodes were cleaned with O_2 plasma for 12 min (the optimal time for the Au_{10} films). Three electrodes are graphed $(Au)_{10}$ gold ($(Au)_{10}$ film on 25 nm Au film) $(Au)_{10}$ O_2 ($(Au)_{10}$ film on 25 nm Au film with O_2 plasma cleaning) $(Au)_{10}$ glass O_2 ($(Au)_{10}$ film on bare glass with O_2 plasma cleaning)

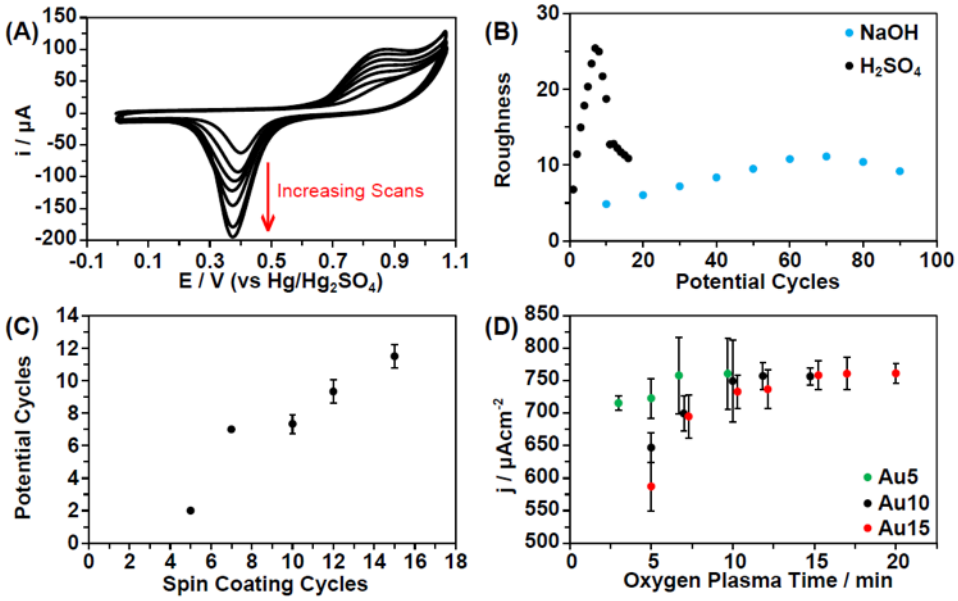

Figure 2.7. Film activation

(A) Potential cycling of an $(Au)_{10}$ film on glassy carbon in 0.5 M H_2SO_4 showing the increasing gold reduction peak, and (B) the resulting roughness factor vs. number of potential cycles plot for both 0.5 M H_2SO_4 and 0.1 M NaOH solutions. Scan rate was always 100mV/s. (C) Optimal number of potential cycles vs. number of spin coating cycles of the gold NP films. (D) Geometric current density of some glass-supported gold films exposed to O_2 plasma for different amounts of time (overlapping data points are offset for clarity).

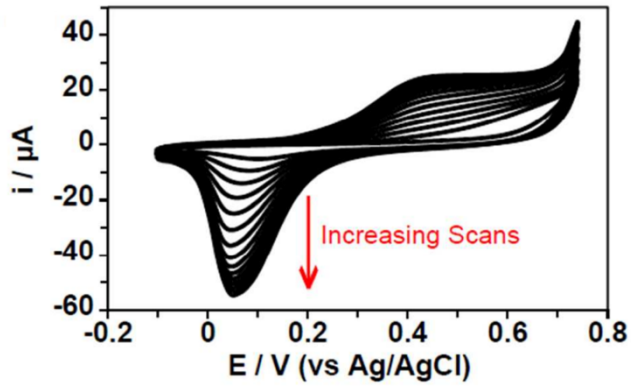

Figure 2.8. Potential cycling of $(Au)_{10}$ in NaOH solution

Potential cycling on an (Au)10 film on glassy carbon in 0.1 M NaOH solution at 100 mV/s scan rate used to activate the nanoparticle film and determine the roughness factor of the film.

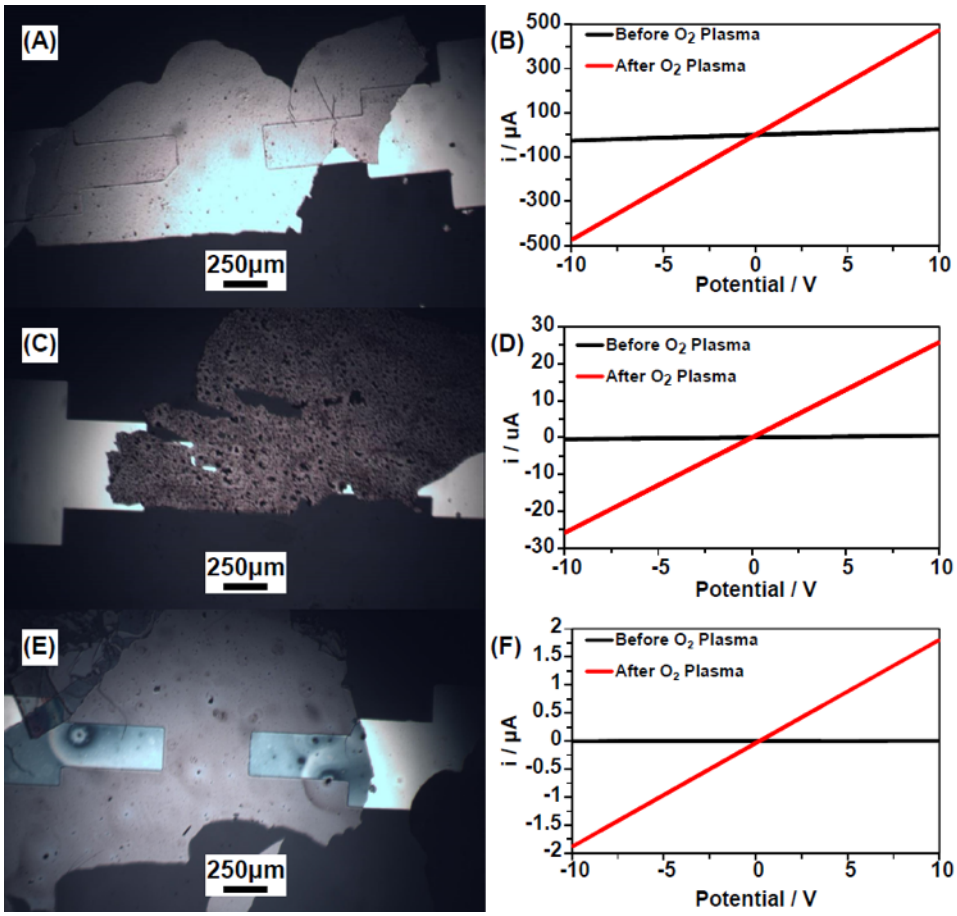

Figure 2.9. Film resistance test

Current-voltage responses from example films from $(Au)_{10}$ (A) (B), $(Au\text{-}Pt)_{10}$ (C) (D), and $(Pt)_{10}$ (E) (F) films measured before and after O_2 plasma treatment showing the relative change in film conductance after O_2 plasma treatment.

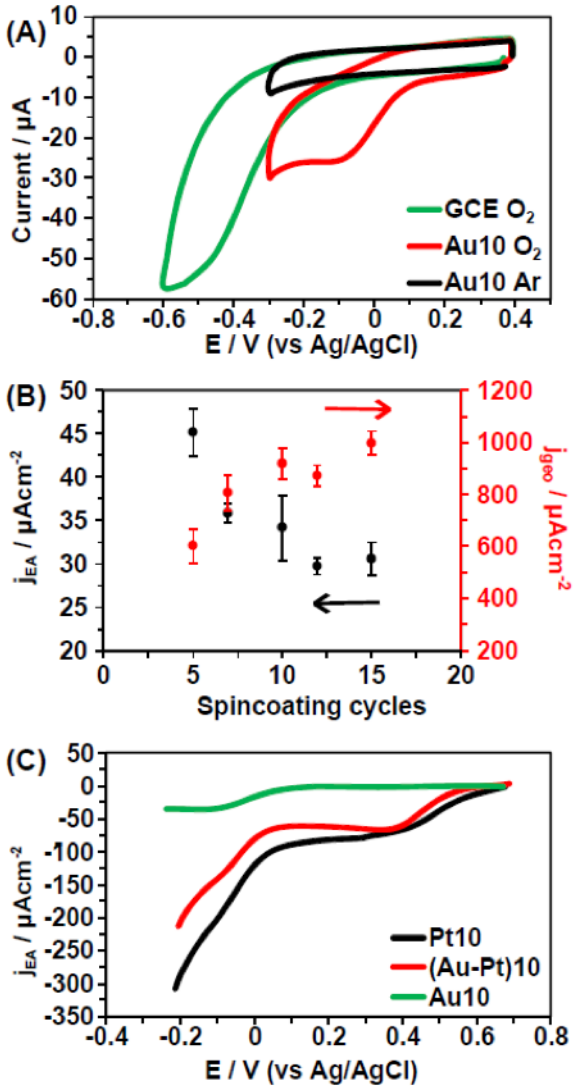

Figure 2.10. ORR CV of NP film

(A) CVs of $(Au)_{10}$ film on GCE in Ar purged and O_2 purged 0.5 M H_2SO_4. (B) ORR current density j_{geo} and j_{EA} in 0.5 M H_2SO_4 vs. number of spin cycles of the gold NP films. (C) CV of $(Au)_{10}$, $(Pt)_{10}$ and $(Au\text{-}Pt)_{10}$ films in 0.5 M H_2SO_4. The current is normalized by electroactive area. Scan rate was 100 mV/s for all CVs.

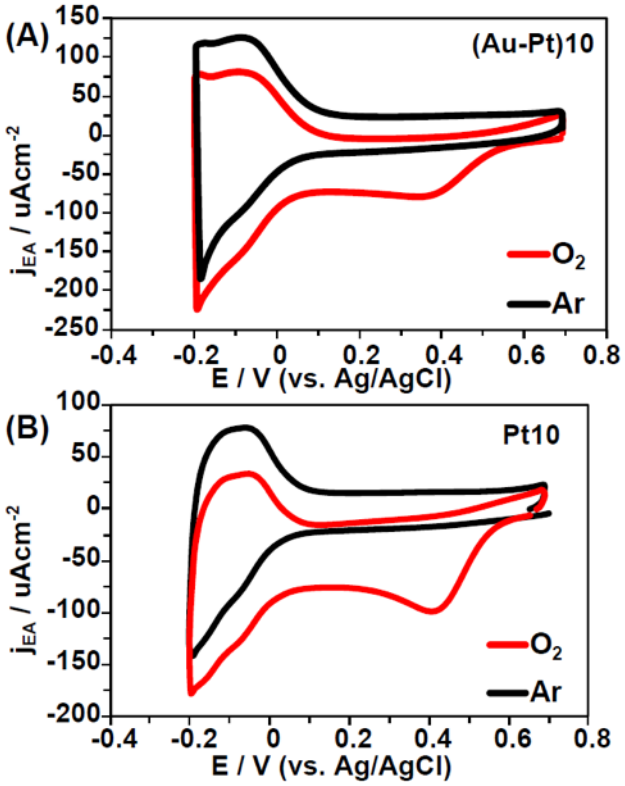

Figure 2.11. ORR CV of Pt-containing film in 0.5 M H_2SO_4

(A) Cyclic voltammetry of an $(Au\text{-}Pt)_{10}$ film on glassy carbon in O_2 and Ar purged 0.5 M H_2SO_4.

(B) Cyclic voltammetry of a $(Pt)_{10}$ film on glassy carbon in O_2 and Ar purged 0.5 M H_2SO_4. Scan rate was 100mV/s.

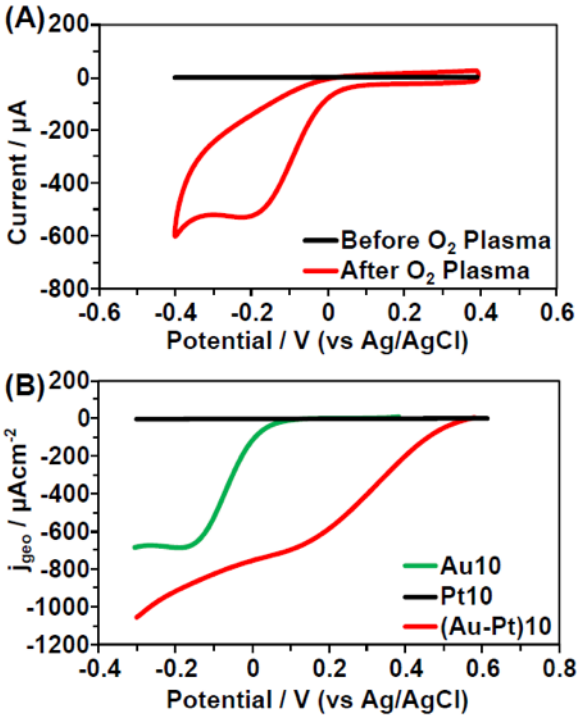

Figure 2.12. ORR CV of glass-supported NP film

(A) CV of $(Au)_{10}$ on glass in O_2 purged 0.5 M H_2SO_4 before and after 12 min of O_2 plasma treatment. (B) CV of $(Au)_{10}$, $(Pt)_{10}$ and $(Au\text{-}Pt)_{10}$ films in O_2 purged 0.5 M H_2SO_4. The current is normalized by geometric area. Scan rate was 100 mV/s.

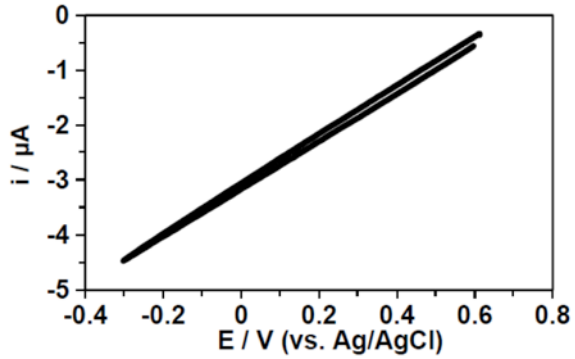

Figure 2.13. ORR CV of inactivated Pt NP film in H_2SO_4

Cyclic voltammetry of a $(Pt)_{10}$ film on glass in O_2 purged 0.5 M H_2SO_4. Scan rate was 100 mV/s.

2.7 REFERENCES

(1) Kumar, S.; Zou, S. Electro-oxidation of Carbon Monoxide and Methanol on Platinum-Overlayer-Coated Gold Nanoparticles: Effects of Film Thickness. *Langmuir* **2007**, 23, 7365-7371.

(2) Yang, R.; Leisch, J.; Strasser, P.; Toney, M. F. Structure of Dealloyed PtCu3 Thin Films and Catalyst Activity for Oxygen Reduction. *Chem. Mater.* **2010**, *22*, 4712-4720.

(3) Erlebacher, J.; Snyder, J. Dealloyed Nanoporous Metals for PEM Fuel Cell Catalysis. *ECS Trans.* **2009**, *25*, 603-612.

(4) Wang, S.; Jiang, S.; White, T. J.; Wang, X. Synthesis of Pt and Pd Nanosheaths on Multi-walled Carbon Nanotubes as Potential Electrocatalysts of Low Temperature Fuel Cells. *Electrochim. Acta.* **2010**, *55*, 7652-7658.

(5) Jia, J.; Wang, B.; Wu, A.; Cheng, G.; Li, Z.; Dong, S. A Method to Construct a Third-Generation Horseradish Peroxidase Biosensor: Self-Assembling Gold Nanoparticles to Three-Dimensional Sol-Gel Network. *Anal. Chem*. **2002**, *74*, 2217-2223.

(6) Yan, X.; Meng, F.; Cui, S.; Liu, J.; Gu, J.; Zou, Z. Effective and Rapid Electrochemical Detection of Hydrazine by Nanoporous Gold. *J. Electroanal. Chem*. **2011**, *661*, 44-48.

(7) Lang, X.; Chen, L.; Guan, P.; Fujita, T.; Chen, M. GeometricEffect on Surface Enhanced Raman Scattering of Nanoporous Gold: Improving Raman Scattering by Tailoring Ligament and Nanopore Ratios. *Appl. Phys. Lett.* **2009**, **94**, 213109-1-213109-3.

(8) Zhang, L.; Chen, L.; Liu, H.; Hou, Y.; Hirata, A.; Fujita, T.; Chen, M. Effect of Residual Silver on Surface-enhanced Raman Scattering of Dealloyed Nanoporous Gold. J *J. Phys. Chem. C* **2011**, *115*, 19583-19587.

(9) Pandey, P. A.; Bell, G. R.; Rourke, J. P.; Sanchez, A. M.; Elkin, M. D.; Hickey, B. J.; Wilson, N. R. Physical Vapor Deposition of Metal Nanoparticles on Chemically Modified Graphene: Observations on Metal-graphene Interactions. *Small* **2011**, *7*, 3202-3210.

(10) Palgrave, R. G.; Parkin, I. P. Aerosol Assisted Chemical Vapor Deposition Using Nanoparticle Precursors: A Route to Nanocomposite Thin Films. *J. Am. Chem. Soc.* **2006**, *128*, 1587-1597.

(11) Suh, J. Y.; Lopez, R.; Feldman, L. C.; Haglund, R. F., Jr. Semiconductor to Metal Phase Transition in the Nucleation and Growth of VO_2 Nanoparticles and Thin films. *J. Appl. Phys.* **2004**, *96*, 1209-1213.

(12) Polarz, S.; Smarsly, B. Nanoporous Materials. *J. Nanosci. Nanotechnol.* **2002**, *2*, 581-612.

(13) Zhao, B.; Collinson, M. M. Hierarchical Porous Gold Electrodes: Preparation, Characterization, and Electrochemical Behavior. *J. Electroanal. Chem.* **2012**, *684*, 53-59.

(14) Bartlett, P. N.; Baumberg, J. J.; Birkin, P. R.; Ghanem, M. A.; Netti, M. C. Highly Ordered Macroporous Gold and Platinum Films Formed by Electrochemical Deposition through Templates Assembled from Submicron Diameter Monodisperse Polystyrene Spheres. *Chem. Mater.* **2002**, *14*, 2199-2208.

(15) Ding, Y.; Kim, Y. J.; Erlebacher, J. Nanoporous Gold Leaf: "Ancient Technology. *Adv. Mater.* **2004**, *16*, 1897-1900.

(16) Sieradzki, K.; Dimitrov, N.; Movrin, D.; McCall, C.; Vasiljevic, N.; Erlebacher, J. The Dealloying Critical Potential. *J. Electrochem. Soc.* **2002,** *149*, 370-377.

(17) Zou, L.; Li, Y.; Cao, S.; Ye, B. Gold Nanoparticles/Polyaniline Langmuir−Blodgett Film Modified Glassy Carbon Electrode as Voltammetric Sensor for Detection of Epinephrine and Uric Acid. *Talanta* **2013**, *117*, 333-337.

(18) Zhang, F.; Srinivasan, M. P. Multilayered Gold-Nanoparticle/Polyimide Composite Thin Film through Layer-by-Layer Assembly. *Langmuir* **2007**, *23*, 10102-10108.

(19) Smirnov, E.; Peljo, P.; Scanlon, M. D.; Girault, H. H. Interfacial Redox Catalysis on Gold Nanofilms at Soft Interfaces. *ACS Nano*. **2015**, *9*, 6565-6575.

(20) Shin, H. C.; Dong, J.; Liu, M. Nanoporous Structures Prepared by an Electrochemical Deposition Process. *Adv. Mater.* **2003**, *15*, 1610-1614.

(21) Wang, H. J.; Ishihara, S.; Ariga, K.; Yamauchi, Y. All-Metal Layer-by-Layer Films: Bimetallic Alternate Layers with Accessible Mesopores for Enhanced Electrocatalysis. *J. Am. Chem. Soc*. **2012**, *134,* 10819-10821.

(22) Gorlin, Y.; Chung, C. J.; Nordlund, D.; Clemens, B. M.; Jaramillo, T. F. Mn3O4 Supported on Glassy Carbon: An Active Non-Precious Metal Catalyst for the Oxygen Reduction Reaction. *ACS Catal.* **2012**, *2*, 2687-2694.

(23) Wei, Q.; Zhao, Y.; Xu, C.; Wu, D.; Cai, Y.; He, J.; Li, H.; Du, B.; Yang, M. Nanoporous Gold Film Based Immunosensor for Label-free Detection of Cancer Biomarker. *Biosens. Bioelectron*. **2011**, *26*, 3714-3718.

(24) Gong, M.; Li, Y.; Wang, H.; Liang, Y.; Wu, J.; Zhou, J.; Wang, J.; Regier, T.; Wei, F.; Dai, H. An Advanced Ni−Fe Layered Double Hydroxide Electrocatalyst for Water Oxidation. J. *Am. Chem. Soc.* **2013**, *135*, 8452-8455.

(25) Alexeyeva, N.; Laaksonen, T.; Kontturi, K.; Mirkhalaf, F.; Schiffrin, D. J.; Tammeveski, K. Oxygen Reduction on Gold Nanoparticle/multi-walled Carbon Nanotubes Modified Glassy Carbon Electrodes in Acid Solution. *Electrochem. Commun*. **2006**, 8, 1475-1480.

(26) Jin, Y.; Shen, Y.; Dong, S. Electrochemical Design of Ultrathin Platinum-Coated Gold Nanoparticle Monolayer Films as a Novel Nanostructured Electrocatalyst for Oxygen Reduction. *J. Phys. Chem. B* **2004**, *108*, 8142-8147.

(27) Ballarin, B.; Cassani, M. C.; Scavetta, E.; Tonelli, D. Self-assembled Gold Nanoparticles Modified ITO Electrodes: The Monolayer Binder Molecule Effect. *Electrochem. Acta* **2008**, *53*, 8034-8044.

(28) Hammond, P. T. Form and Function in Multilayer Assembly: New Applications at the Nanoscale. *Adv. Mater.* **2004**, *16*, 1271-1293.

(29) Schmidt, D. J.; Hammond, P. T. Electrochemically Erasable Hydrogen-Bonded Thin Films. *Chem. Commun*. **2010**, *46*, 7358-7360.

(30) Zhang, Y.; Guan, Y.; Yang, S.; Xu, J.; Han, C. Fabrication of Hollow Capsules Based on Hydrogen Bonding. *Adv. Mater*. **2003**, *15*, 832-835.

(31) Decher, G. Fuzzy Nanoassemblies: Toward Layered Polymeric Multicomposites. *Science* **1997**, *277*, 1232-1237.

(32) Major, J. S.; Blanchard, G. J. Covalently Bound Polymer Multilayers for Efficient Metal Ion Sorption. *Langmuir* **2001**, *17*, 1163-1168.

(33) Such, G. K.; Quinn, J. F.; Quinn, A.; Tjipto, E.; Caruso, F. Assembly of Ultrathin Polymer Multilayer Films by Click Chemistry. *J. Am. Chem. Soc*. **2006**, *128*, 9318–9319.

(34) Shipway, A. N.; Lahav, M.; Blonder, R.; Willner, I. BisBipyridinium Cyclophane Receptor-Au Nanoparticle Superstructures for Electrochemical Sensing Applications. *Chem. Mater.* **1999**, *11*, 13-15.

(35) Riskin, M.; Tel-Vered, R.; Bourenko, T; Granot, E.; Willner, I. Imprinting of Molecular Recognition Sites through Electropolymerization of Functionalized Au Nanoparticles: Development of an Electrochemical TNT Sensor Based on π-Donor−Acceptor Interactions. *J. Am. Chem. Soc.* **2008**, *130*, 9726-9733.

(36) Bahshi, L.; Frasconi, M.; Tel-Vered, R.; Yehezkeli, O.; Willner, I. Following the Biocatalytic Activities of Glucose Oxidase by Electrochemically Cross-Linked Enzyme−Pt Nanoparticles Composite Electrodes. *Anal. Chem.* **2008**, *80*, 8253-8259.

(37) Guo W.; Pi Y.; Song H.; Tang W.; Sun. J. Layer-by-layer Assembled Gold Nanoparticles Modified Anode and its Application in Microbial Fuel Cells. *Colloids Surf. A* **2012**, *415*, 105-111.

(38) Guo, W.; Cui, Y.; Song, H.; Sun, J. Layer-by-layer Construction of Graphene-based Microbial Fuel Cell for Improved Power Generation and Methyl Orange Removal. *Bioprocess Biosyst. Eng.* **2014**, *37*, 1749-1758.

(39) Kim, Y.; Zhu, J.; Yeom, B.; Prima, M. D.; Su, X.; Kim, J. G.; Yoo, S., J.; Uher, C.; Kotov, N. Stretchable Nanoparticle Conductors with Self-organized Conductive Pathways. *Nature* **2013**, *500*, 59-64.

(40) Hammond, P. T. Form and Function in Multilayer Assembly: New Applications at the Nanoscale. *Adv. Mater.* **2004**, *16*, 1271-1293.

(41) Yu, Y.; Huang, S.; Li, Y.; Steinmann, S. N.; Yang, W.; Cao, L. Layer-Dependent Electrocatalysis of MoS_2 for Hydrogen Evolution. *Nano Lett.* **2014**, *14*, 553–558.

(42) Schlicke, H.; Schroder J. H.; Trebbin M.; Petrov A.; Ijeh M.; Weller H.; Vossmeyer T. Freestanding Films of Crosslinked Gold Nanoparticles Prepared via Layer-by-layer Spin-coating. *Nanotechnology* **2011**, *22*, 305303-305311.

(43) Adams, K. L.; Jena, B. K.; Percival, S. J.; Zhang, B. Highly-Sensitive Detection of Exocytotic Dopamine Release using a GoldNanoparticle-Network Microelectrode. *Anal. Chem.* **2011**, *83*, 920-927.

(44) Brown, K. R.; Fox, A. P.; Natan, M. J. Morphology-Dependent Electrochemistry of Cytochrome c at Au Colloid-Modified SnO_2 Electrodes. *J. Am. Chem. Soc.* **1996**, *118*, 1154-1157.

(45) Liu, G. Z.; Luais, E.; Gooding, J. J. The Fabrication of Stable Gold Nanoparticle-Modified Interfaces for Electrochemistry. *Langmuir* **2011**, *27*, 4176-4183.

(46) Wang, J. Electrochemical Biosensing based on Noble Metal Nanoparticles. *Microchimica Acta* **2012**, *177*, 245-270.

(47) Li, Y.; Cox, J. T.; Zhang, B. Electrochemical Response and Electrocatalysis at single Au Nanoparticles. *J. Am. Chem. Soc.* **2010**, *132*, 3047-3052.

(48) Peng, S.; Lee, Y.; Wang, C.; Yin, H.; Dai, S.; Sun, S. A Facile Synthesis of Monodisperse Au Nanoparticles and their Catalysis of CO Oxidation. *Nano Res.* **2008**, *1*, 229–234.

(49) Miyabayashi, K.; Nishihara, H.; Miyake, M. Platinum Nanoparticles Modified with Alkylamine Derivatives as an Active and Stable Catalyst for Oxygen Reduction Reaction. *Langmuir* **2014**, *30*, 2936–2942.

(50) Watson, D. C.; Martinez, R. V.; Fontana, Y.; Russo-Averchi, E.; Heiss, M.; Morral, A. F.; Whitesides, G. M.; Loncar, M. Nanoskiving Core−Shell Nanowires: A New Fabrication Method for Nano-optics. *Nano Lett.* **2014**, *14*, 524−531.

(51) Hines, M. A.; Todd, J. A.; Guyot-Sionnest, P. Conformation of Alkanethiols on Au, Ag(111), and Pt(111) Electrodes: A Vibrational Spectroscopy Study. *Langmuir* **1995**, *11*, 493-497.

(52) Castner, D. G.; Hinds, K.; Grainger, D. W. X-ray Photoelectron Spectroscopy Sulfur 2p Study of Organic Thiol and Disulfide Binding Interactions with Gold Surfaces. *Langmuir*, **1996**, *12*, 5083-5086.

(53) Bard, A. J.; Faulkner, L. R. Elecrochemical Methods, 2nd ed.; John Wiley & Sons: New York, 2001.

(54) Anicet, N.; Bourdillon, C.; Moiroux, J.; Saveant, J. M. Electron Transfer in Organized Assemblies of Biomolecules. Step-by-Step Avidin/Biotin Construction and Dynamic Characteristics of a Spatially Ordered Multilayer Enzyme Electrode. *J. Phys. Chem. B* **1998**, *102*, 9844-9849.

(55) Moorcroft, M. J.; Lawrence, N. S.; Coles, B. A.; Compton, R. G.; Trevani, L. N. High Temperature Electrochemical Studies using a Channel Flow Cell Heated by Radio Frequency Radiation. *J. Electroanal. Chem.* **2001**, *506*, 28-33.

(56) Cannes, C.; Kanoufi, F.; Bard, A. J. Cyclic Voltammetry and Scanning Electrochemical Microscopy of Ferrocenemethanol at Monolayer and Bilayer-modified Gold Electrodes. *J. Electroanal. Chem.* **2003**, *547*, 83-91.

(57) Pfeiffer, C.; Rehbock, C.; Hühn, D.; Carrillo-Carrion, C.; Aberasturi, D.; Merk, V.; Barcikowski, S.; Parak. W. J. Interaction of Colloidal Nanoparticles with their Local Environment: the (ionic) Nanoenvironment around Nanoparticles is Different from Bulk and Determines the Physico-chemical Properties of the Nanoparticles. *J. R. Soc. Interface* **2014**, *11,* 20130931.

(58) Smith, T. The Hydrophilic Nature of a Clean Gold Surface. *J. Colloid and Interface Sci.* **1980**, *75*, 51-55.

(59) Chen, P.; McCreery, R. L. Control of Electron Transfer Kinetics at Glassy Carbon Electrodes by Specific Surface Modification. *Anal. Chem.* **1996**, *68*, 3958-3965.

(60) Strong, L.; Whitesides, G. M. Structures of Self-Assembled Monolayer Films of Organosulfur Compounds Adsorbed on Gold Single Crystals: Electron Diffraction Studies. *Langmuir* **1988**, *4*, 546-558.

(61) Yang, D.; Wilde, C. P.; Morin, M. Studies of the Electrochemical Removal and Efficient Re-formation of a Monolayer of Hexadecanethiol Self -Assembled at an Au(111) Single Crystal in Aqueous Solutions. *Langmuir* **1997**, *13*, 243-249.

(62) Burke, L. D.; Cunnane, V. J. Possible Importance of Adions in Both the Binding of Lewis Bases and the Electrocatalytic Oxidation of Dissolved Organics at Gold Electrodes in Aqueous Media. *J. Electroanal. Chem.* **1986**, *210*, 69-94.

(63) Sheridan, A. K.; Ngamukot, P.; Bartlett, P. N.; Wilkinson, J. S. Waveguide Surface Plasmon Resonance Sensing: Electrochemical Desorption of Alkane Thiol Monolayers. *Sens. Actuators, B: Chem.* **2006**, *117*, 253-260.

(64) Cui, H.-F.; Ye, J.-S.; Zhang, W.-D.; Wang, J.; Sheu, F.S. Electrocatalytic Reduction of Oxygen by a Platinum Nanoparticle/Carbon Nanotube Composite Electrode. *J. Electroanal. Chem.* **2005**, *577*, 295-302.

(65) Campbell, C. T.; Sellers J. R. V. Anchored Metal Nanoparticles: Effects of Support and Size on their Energy, Sintering Resistance and Reactivity. *Farad. Discuss.* **2013**, *162*, 9-30.

(66) Hernandez J.; Solla-Gullo, J.; Herrero, E.; Aldaz, A.; Feliu, J. M. Electrochemistry of Shape-Controlled Catalysts: Oxygen Reduction Reaction on Cubic Gold Nanoparticles. *J. Phys. Chem. C*. **2007**, *111*, 14078-14083.

(67) Ye, H.; Crooks, R. M. Contribution Effect of Elemental Composition of PtPd Bimetallic Nanoparticles Containing an Average of 180 Atoms on the Kinetics of the Electrochemical Oxygen Reduction Reaction. *J. Am. Chem. Soc.* **2007**, *129*, 3627-3633.

(68) Fu, S.; Yang, G.; Zhou, Y.; Pan, H-B.; Wai, C. M.; Dan D.; Lin Y. Ultrasonic Enhanced Synthesis of Multi-walled Carbon Nanotube Supported Pt−Co Bimetallic Nanoparticles as Catalysts for the Oxygen Reduction Reaction. *RSC Adv.* **2015**, *5*, 32685-32689.

Chapter 3. CHARACTERIZATION OF THE APPARENT ELECTROACTIVE AREA OF JANUS NANOPARTICLES USING SINGLE-NANOPARTICLE COLLISION

This chapter is mostly adapted from the manuscript: Han, C.; Luo, Y.; Gunderson, C.; Zhao, J.; Zhang, B. " Characterization of the Apparent Electroactive Area of Janus Au-SiO_2 Nanoparticles Using Single-Nanoparticle Collision", in preparation.

3.1 ABSTRACT

Here we report the electrochemical characterization of Janus Au-silica nanoparticles at the single particle level with single-nanoparticle collision method. By holding a constant potential on an inert carbon ultramicroelectrode (UME), current transient can be induced and detected when a single Janus nanoparticle lands on the electrode surface and catalyzes the reaction of the redox indicator. Different molecules such as hydrazine and proton were examined in the Janus nanoparticle collision experiment. By comparing the diffusion-limited current steps of Janus nanoparticles to the current of Au nanoparticles, we were able to calculate the electroactive area of Au-SiO_2 nanoparticles. Through the simulation of the hydrazine concentration profile on the Au-SiO_2 nanoparticle, the geometry was correlated with electroactivity. This work demonstrates that nanoparticle collision experiment can be a simple and efficient technique to characterize single Janus nanoparticles and study the structure-activity relationship quantitatively.

3.2 INTRODUCTION

Janus nanoparticles are known as a kind of multifunctional nanocomposites that have two sides with different chemical and physical properties.[1] Attributing to their dimensions and asymmetric geometry, they are able to present novel properties including optical, electronic,

magnetic, and surface properties.[2] For example, amphiphilic Janus nanoparticles can mimic the behavior of colloidal surfactant molecules and show tunable self-assembly characteristics.[3,4] The asymmetrical chemical structures of Janus nanoparticles are able to exhibit enhanced catalytic activity.[5,6] The asymmetric catalytic properties of Janus nanoparticles can be used in nanomotors and nanojets.[7-9] And by modifying two sides with difference functional groups, one side can act as target-specific receptors while the other side contributes to sensing events.[10,11] Moreover, surface plasmon resonance exhibited by metallic Janus nanoparticles allows their application in optical field.[12,13] Therefore, these excellent qualities make Janus nanoparticles a unique type of material and they show a great potential for future applications.

A variety of methods have been developed to synthesize Janus nanoparticles.[14] However, more work is still needed for unambiguous structural characterization and quantifying their Janus characteristics. The most commonly employed techniques are microscopy methods such as electron microcopy and scanning probe microscopy, and macroscopic methods such as FTIR spectroscopy, contact angle measurements, UV-visible spectroscopy, and NMR measurements.[15] Electron microcopy and scanning probe microscopy can give accurate morphology information, but it is not very effective with the presence of polydispersed nanoparticles. Moreover, due to the low contrast of organic materials it is challenging to characterize polymer-coated nanoparticles. Macroscopic methods mentioned above measure properties attributed to Janus nanoparticles, but they exhibit results from the ensemble and often cannot differentiate Janus nanoparticles from other kind of non-symmetric nanoparticles. Therefore, new techniques are needed to be employed or combined with others to better identify and quantify both single Janus nanoparticle and patchy Janus nanoparticles.

The method of nanoparticle collision or nanoparticle impact is one of the most effective approaches to investigate electrochemical behavior of single nanoparticles. [16] An ultramicroelectrode is commonly used to measure the transient current signal induced by a single particle when it adsorbs on the electrode surface. The detected transient current signal could be a decay in its faradaic signal when the particle is electrochemically inert and blocks the flux of a redox mediator,[17,18] or a current increase when the particle is catalytically active and enhance the faradaic reaction of a redox mediator[19,20], or the particle is reacting itself [21-23]. In this study, Janus Au-SiO_2 nanoparticles were electrochemically characterized by single-nanoparticle collision method.

The detection system we use involves the hydrazine oxidation and proton reduction on a carbon fiber electrode to detect Janus Au-SiO_2 nanoparticles. The inert carbon fiber electrode gives low background current at low potentials. As shown in Figure 3.1, when a single Au-SiO_2 nanoparticle lands on the electrode surface and the Au side is in contact with the electrode, the Au surface can catalyze hydrazine electro-oxidation, which results in a transient current signal in the current-time trace. Since the SiO_2 part hinders hydrazine from diffusing to the Au surface, the Au-SiO_2 particles would result in a smaller current signal than bare Au nanoparticles. The detection current reflects the electroactive area of the Janus nanoparticle and the exposed Au surface area. The geometry of the Janus particle can be further calculated from the electroactive area. This method is simple and high-throughput compared to other characterization methods.

3.3 Experimental Section

3.3.1 *Chemicals and Materials*

All chemicals and materials were used as received from the manufacturers. Potassium chloride (KCl, Mallinckrodt Baker), hydrazine (anhydrous 98%, Sigma Aldrich), monobasic

potassium phosphate (KH_2PO_4, J.T. Baker), dibasic potassium phosphate (K_2HPO_4, J.T. Baker), 2-allylphenol (Sigma Aldrich), citric acid monohydrate (Fisher Scientific), gold (III) chloride trihydrate (≥99.9% trace metals basis, Sigma Aldrich), poly (acrylic acid) (Sigma Aldrich), 3-mercaptopropionic acid (≥ 99%, Sigma Aldrich), tetraethyl orthosilicate (≥ 99.0%, Sigma Aldrich), 2-propanol (ACS reagent, ≥99%, Sigma Aldrich), sodium citrate dehydrate (Fisher Scientific), ammonium hydroxide (28.0-30.0%, J. T. Baker). All aqueous solutions were prepared using deionized water (>18 MΩ cm) obtained through a Barnstead Nanopure water purification system.

3.3.2 *Preparation of Au Nanoparticles*

The Au nanoparticles were prepared in University of Connecticut. We adopted Frens' method to synthesize the 40 nm Au nanoparticles.[24] First, 99 mL of DI water was added into the 250 mL flask, followed by the addition of 1.06 mL of $HAuCl_4$ solution (0.0254 M in DI water). The mixture was brought to boil under heating. Once the solution boils, 1.0 mL of the sodium citrate solution (0.0388 M in DI water) was immediately added to the flask. The solution was allowed for 15 min' heating under 160 ^oC and then cooled to room temperature.

3.3.3 *Preparation of Au-SiO_2 Nanoparticles*

The Au-SiO_2 nanoparticles were prepared in University of Connecticut. We adopted the method proposed by Chen et al. to synthesize Janus particles.[25] 3 mL of as prepared Au nanoparticle solution were concentrated to 0.5 ml by centrifugation. The concentrated Au nanoparticle solution was added to a mixture of 2.4 mL of 2-proponal and 0.1 mL of DI water. 20 μL of 3-mercaptopopionic acid (5 mM in ethanol) and 20 μL of polyacrylic acid (0.645 mM in water) were then added to the solution. The mixture was allowed to stir for 30 min. 600 μL of

tetraethyl orthosilicate (8.9 mM in ethanol) and 90 μL of ammonium hydroxide were added afterwards. The reaction was kept under room temperature for overnight. Before use the Janus nanoparticles were mixed with DI water with 1:1 ratio and centrifuged at 4500 rpm for 15 min. After removing the supernatant, the Janus nanoparticles left were dissolved in DI water again.

3.3.4 *Transmission Electron Microscope (TEM) Imaging*

Au and Janus Au-SiO_2 nanoparticles were transferred to carbon-coated TEM grid (Electron Microscopy Sciences) for TEM imaging. FEI Tecnai G2 Spirit BioTWIN in University of Connecticut was used to acquire the TEM images under 80 kV, as shown in Figure 3.2.

3.3.5 *Fabrication of the Carbon Fiber Ultramicroelectrodes*

The preparation of carbon fiber ultramicroelectrodes was described in detail elsewhere.[26] Briefly, a piece of 5 μm diameter carbon fiber was sealed in a borosilicate capillary by thermal pulling on a pipette puller (Sutter Instrument P-97). Then electrical contact was made by using a tungsten wire and silver paste (DuPont). The carbon fiber extended out of the capillary was further insulated by electrochemical polymerization of 2-allylphenol in a 0.90 mM solution in a 1:1 H_2O : CH_3OH solution (pH = 9.0 – 9.2). A + 4 V D.C. voltage was applied to the exposed carbon fiber vs. a Pt wire counter electrode for ~6 min. The electrode was then heated to 150 ^oC for 30 min in an oven to cure the polymer. The electrode was cut with a sharp scalpel before each collision experiment to revel a fresh surface.

3.3.6 *Electrochemical Measurements*

All the electrochemical experiments were performed by using a Axopatch 200B integrating patch-clamp amplifier (Molecular Devices). Amperometry data were recorded on a Dell PC through a Digidata 1440 digitizer (Molecular Devices). The Axopatch was used in V-clamp mode

with whole cell β = 1 and the low-pass filter set to 1 kHz. Amperometric traces were recorded using pClamp 10.4 Axoscope software (Molecular Devices) with a 50 kHz rate of data recording. All experiments were performed using a two-electrode setup placed in a lab-built Faraday cage. Homemade Ag/AgCl electrodes, which were fabricated by dipping a silver wire (0.1 mm diameter, Alfa Aesar) in ferric chloride, were used as reference electrodes for all electrochemical measurement. nanoparticle collision experiments were performed in an aqueous solution of 15 mM hydrazine with 15 mM phosphate buffer (PB, pH 7.4) using final nanoparticle concentrations of 2.1 pM.

3.3.7 *Numeric Simulation*

All simulations were done using COMSOL 3.5a Multiphysics software (COMSOL Inc., Burlington, MA). Details of the simulation, including geometry and parameters, can be found in Figure 3.9.

3.4 Results and Discussion

3.4.1 *Electrochemical Detection through Single Nanoparticle Collision*

Figure 3.3a displays characteristic amperomeric traces of Janus Au-SiO_2 nanoparticle detection recorded at 0.6 V vs. Ag/AgCl on a 5 μm carbon fiber electrode in solutions that contain 15 mM hydrazine, 5 mM PB (pH = 7.4) and 2.1 pM particles. In the absence of nanoparticles, a decaying baseline current was recorded when +0.6 V was applied on the carbon electrode (Figure 3.3c). The baseline current keeps decaying due to the deactivation of carbon surface in the solution.[14] After adding 2.1 pM Au-SiO_2 nanoparticles, however, current steps followed by slow current decay were observed in the current-time trace (left panel in Figure 3.3a). Each current step corresponds to the collision and sticking event of a single particle, catalyzing the electro-oxidation

reaction of hydrazine molecules on the Au surface and slowly getting deactivated. The right panel of Figure 3.3a is a histogram showing the distribution of the current step height from 227 recorded particle events. A small population around 70 pA is likely due to bare Au NP aggregates in the Janus NP batch. The average current step height from Gaussian fitting was 21.73 ± 0.55 pA. The Au-SiO_2 particles were prepared by growing SiO_2 on pre-synthesized 40 nm Au nanoparticles.[27] The same batch of Au nanoparticles were also used in single-nanoparticle collision experiment in order to study the effect of SiO_2 coating on the Janus nanoparticles to its electrocatalytic activity. For Au nanoparticles (Figure 3.3b), larger current steps with faster current decay were detected. The right panel of Figure 3.3b shows the distribution of the current step height from 495 recorded particle events. The average value of current steps from Gaussian fitting is 38.76 ± 2.17 pA. Moreover, the current time trace shows a much higher detection frequency. We attributed the difference in electrochemical behavior such as current shape, current step and frequency to the SiO_2 part of the Janus NPs. The average current step height of Au-SiO_2 particles is smaller compared with that of Au particles because SiO_2 is not catalytically active and blocks hydrazine from diffusing to unexposed Au surface. The difference in current shape also indicates that Au particles deactivate faster due to a larger exposed electroactive area. Since the Janus nanoparticles collide onto the electrode surface in a random way, we only detect transient current signals when the exposed Au side is in contact with the electrode surface, resulting in a lower detection frequency. The magnitude of the current step can also be affected by the orientation of SiO_2 when the exposed Au surface is in contact with the electrode surface. This is attributed to different amount of hydrazine molecules diffusing to exposed Au surface, which will be discussed later in the numeric simulation part.

Besides hydrazine, we are curious about the catalytic activity of Janus nanoparticles toward other redox indicators, such as protons. In order to avoid nanoparticle aggregation in the solution, 50 mM sodium dihydrogencitrate ($NaC_6H_7O_7$) was used as the proton source in the collision experiment.[20] As shown in the left panel of Figure 3.4c, at -0.8V vs. Ag/AgCl, with no particles present in the solution, no transient current signal was observed. Upon addition of Au nanoparticles, as displayed in Figure 3.4b, sharp reductive current spikes instead of steady current steps were detected in the current-time trace, similar as reported in the literature.[28] Here a 5 kHz low pass filter was used instead of 1 kHz in order to avoid the influence from filter. The average current spike magnitude is 21.71 ± 8.79 pA, and the charge transfer during this process can be calculated from the integration of peak area, which is 198.99 ± 83.15 fC. The time duration of the current spike is only 0.5 - 1 ms, which might be due to rapid deactivation of nanoparticles due to H atom adsorption after collision.[29] With Au-SiO_2 nanoparticle present in the solution **(**Figure 3.4a**)**, sharp reductive spikes were still observed but the magnitude is much smaller compared to those induced by Au nanoparticles (16.68 ± 4.85 pA), as shown in right panel of Figure 3.4. Also, the charge integrated from the peak area is also smaller (47.39 ± 5.44 pA), indicating that Au-SiO_2 nanoparticles have a lower electroactive area towards proton reduction than Au nanoparticles. Assuming there is a monolayer of H atom adsorption on the Au surface, we can estimate that ~76% of the Au area was retained by the Janus Au-SiO_2 nanoparticles compared to Au nanoparticles. Since we were able to get steady-state current from Janus nanoparticle collisions in hydrazine solution, we focused on hydrazine oxidation on nanoparticles in the following discussion.

By measuring the height of the catalytic current steps, as the current histogram shows (right panels in Figure 3.3a), we were able to evaluate the electrocatalytic activity of Au-SiO_2 nanoparticles. However, the catalytic current could be influenced by both applied potential and

particle orientation. The observed catalytic current distributions under different applied potentials are shown in Figure 3.5a. Average current step heights were extracted from these histograms by Gauss fitting and plotted in Figure 3.6a represented by the red dots. The average current step heights of Au nanoparticles were plotted in the same figure represented by the black dots. In this way the "CV (cyclic voltammogram)" of single Au-SiO_2 and Au nanoparticles on carbon electrode in 15 mM hydrazine solution were obtained. There is no obvious current signal observed induced by Au-SiO_2 nanoparticles at 0.3 V or lower potential, as shown in Figure 3.7, because the Axopatch is not sensitive enough to detect smaller catalytic current.

From the "CV" from single-nanoparticle collision experiment we found that the current steps of Au and Au-SiO_2 did not reach steady state current until 0.6 V, which is 0.2 V higher than what our group reported for other Au nanoparticles.[30] This is due to different catalytic activity among different nanoparticles. It could be affected by particle shape, crystal facets and ligands on the particle surface. However, the fact that the catalytic current of Au nanoparticles and Au-SiO_2 nanoparticles both reach steady state at 0.6 V indicates that after SiO_2 growth on the Au particles, the exposed Au part still retains its catalytic activity.

Assuming the hydrazine oxidation on Au surface is only limited by diffusion and the catalytic current on carbon electrode can be neglected, we calculate the theoretical steady-state current on a spherical Au nanoparticle from this equation,

$$i_{ss} = 4\pi \ln(2) nFDC^{*}r \qquad (3.2)$$

where i_{ss} is the diffusion limited current on the nanoparticle, n = 4 is the number of electrons, F is the Faraday's constant, D is the diffusion coefficient of hydrazine (1.39×10^{-5} cm^2/s)[31], C* is the bulk concentration of hydrazine, r is the radius of the particle. For a 40 nm Au nanoparticle in 15 mM hydrazine, based on diffusion limitation the theoretically predicted current would be 1386

pA, which is larger than the average current step we measured in the Au nanoparticle collision experiment. One reason is that part of the active sites of particles could be blocked by surface ligands.[32] Another reason is that hydrazine oxidation also occurs on carbon electrode surface at a relatively high potential and decrease the actual hydrazine concentration on nanoparticle surface. The average current step of Janus nanoparticle is always smaller than the current on Au nanoparticles under different applied potentials, indicating that Janus nanoparticles has less electroactive area in catalyzing hydrazine oxidation than Au nanoparticles. The lower current on Janus nanoparticle is attributed to less exposed Au area.

We divided the current of Au-SiO_2 by the current of Au to calculate $\%_{iAu\text{-}SiO2}/i_{Au}$. (Figure 3.6b) The purpose is to evaluate how much catalytic activity the Janus nanoparticle has. Under the same experimental conditions, the diffusion limited current on Janus nanoparticles is 55% of the current on Au nanoparticles, indicating the exposed Au part of Janus nanoparticle retains 55% electrochemical activity of the Au nanoparticle. This number is smaller than the result obtained from proton reduction (76%), which reflects an interesting fact: some of the exposed Au area that can adsorb H may not be able to oxidize hydrazine molecules. In the next step, we tried to study the morphology of nanoparticles by calculating the theoretical diffusion-limited current on the Janus nanoparticle on the electrode surface with finite element model (FEM) simulation, as discussed in the numeric simulation section. The detection frequency in the collision experiments is related with the diffusion of nanoparticles to the electrode surface.[23] Theoretical calculation of collision frequency from diffusive flux is shown in Appendix. The theoretical collision frequency of 40 nm Au nanoparticles due to diffusion is 0.17 Hz, which is lower than the actual detection frequency in our Au particle collision experiments (Figure 3.6c). This is because the negatively charged nanoparticles can be attracted to the positively-biased electrode and results in an

enhancement in the collision frequency, which has been reported in literature.[33] From Figure 3.6c, one can see that both Au and Au-SiO_2 nanoparticles generally show a generally increasing trend in collision frequency as the applied potential is increased, which also indicates the effect of electric field. Moreover, the collision frequency of Au-SiO_2 particles is always less than half than the frequency of Au nanoparticles. One reason is the slower diffusion rate of Au-SiO_2 nanoparticles in the solution compared to Au nanoparticles due to their larger size.[34] More importantly, the Au-SiO_2 nanoparticle collision events could not be detected when the exposed Au surface is not in contact with electrode surface. This indicates that the orientation of Janus particles plays an important role in electrochemical detection.

3.4.2 *Numeric Simulation*

The electroactivity could be correlated with the geometry of the Janus nanoparticle by simulating the electrochemical response of a Janus nanoparticle on electrode surface with COMSOL software. We only consider the situation where the exposed Au surface is in contact with the electrode surface because otherwise there is no current response. Due to the different diffusion regimes of hydrazine on Janus nanoparticle with different orientations, we consider two extreme conditions when the SiO_2 side is facing up (orientation A) and down (orientation B) respectively, as displayed in in Figure 3.8a and b. We expect the Au-SiO_2 particle collision events at orientation B would generate the maximum current while the collision events at orientation A would produce the minimum current. Therefore, the current generated by Janus nanoparticle collision should be in the range of these two values.

The steady-state diffusion limited current at orientation A was simulated using a 2-D axisymmetric model (Figure 3.9a). The steady-state diffusion limited current at orientation B was simulated using a 3-D model (Figure 3.9b). The geometry and boundary conditions of these two

models can be found in Figure 3.9. To simplify the simulation, we assume the Janus nanoparticle is composed of two spheres, and h is a parameter defined as the overlapping distance between the SiO_2 sphere and Au sphere, which reflects the extent of Au surface being covered by SiO_2. The size of Au and SiO_2 spheres are determined from TEM images (Figure 3.10). A variety of diffusion limited catalytic currents from hydrazine oxidation can be obtained by adjusting the parameter h, and the simulated results are shown in Table 3.3. The percent ratio of the simulated current on a Au-SiO_2 particle to the simulated diffusion limited current of a Au particle is also include in Table 3.3. According to the single-nanoparticle collision experiment, the measured catalytic current on Janus nanoparticles is 55% of the catalytic current on Au nanoparticles. Comparing simulation results with experimental results, the overlapping distance h should be around 28 nm to obtain a percent ratio closest to 55%, therefore the Janus nanoparticle exposed 30% of the entire Au particle surface. In this way the geometry of Janus nanoparticle can be quantified.

3.5 CONCLUSIONS

In summary, we have presented the characterization of single Janus Au-SiO_2 nanoparticles by the single-nanoparticle collision method. The electrochemical behavior was found to differ between the Au nanoparticles and the Janus nanoparticles that are synthesized from Au particles. We can calculate the electroactive area of the Janus nanoparticles and exposed Au particle area by comparing the diffusion limited current obtained on Au-SiO_2 nanoparticles with that on Au nanoparticles. The single-nanoparticle collision method is an effective and high-throughput way to assess the electroactivity of Janus nanoparticles in single nanoparticle level. This method improves our understanding in fundamental knowledge of Janus nanoparticles and help to extend its application in electrochemistry.

3.6 APPENDIX

Estimate of collision frequency from diffusive flux

For the 40 nm Au nanoparticle, collision frequency on the 5 μm carbon electrode can be estimated by calculating the diffusion flux.

$f = 4DCr = 4\times(1.1\times10^{-7}\ cm^2/s)\times(2.1\times10^{-15}\ mol/cm^3)\times(6.02\times10^{23}/mol)\times2.5\times 10^{-4}cm = 0.17\ particles/s$

Here D is the diffusion coefficient of the nanoparticles, C is the concentration of nanoparticles, r is the electrode radius.

The diffusion coefficient of nanoparticles can be calculated from Stokes-Einstein equation.

$$D = \frac{kT}{6\pi\eta r_{NP}}$$

where k is the Boltzmann constant, T is the absolute temperature, η is the viscosity of water (8.94×10^{-4} Pa· s at 25 ° C), and r_{NP} is the radius of the NP. The diffusion coefficient of the Au NP according to Stokes-Einstein equation is 1.1×10^{-7} cm^2/s.

3.7 TABLES AND FIGURES

Table 3.3. Simulated diffusion-limited current of Au and Au-SiO_2 nanoparticles

Simulated steady-state diffusion limited current of a Janus NP on a carbon fiber surface with different orientation and different geometric structure. Here h is the overlapping distance between the SiO_2 and Au NP.

h / nm	A (SiO_2 up) / pA	%Au	B (SiO_2 down) / pA	%i(SiO_2)/i(Au)
25	841.65	59.75%	879.72	62.45%
26	818.30	58.09%	852.47	60.52%
27	787.34	55.89%	821.76	58.34%
28	755.02	53.60%	791.39	56.18%
29	720.43	51.15%	756.8	53.73%
30	684.2	48.57%	724.38	51.43%

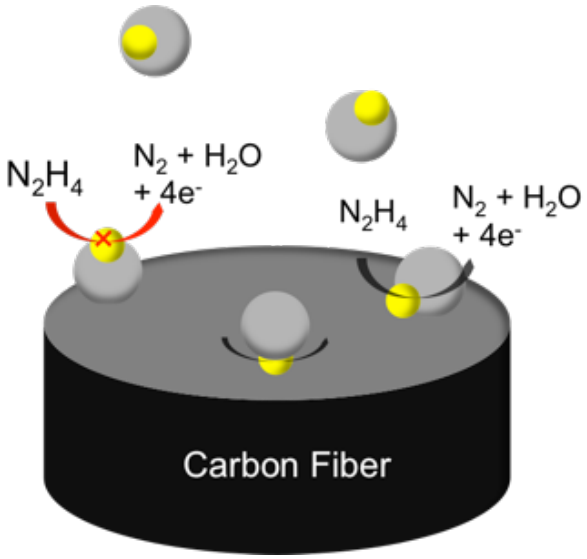

Figure 3.1. Schematic of Au-SiO_2 nanoparticles collision

Schematic depicting a Janus nanoparticle collision on a carbon fiber UME in hydrazine with different orientations.

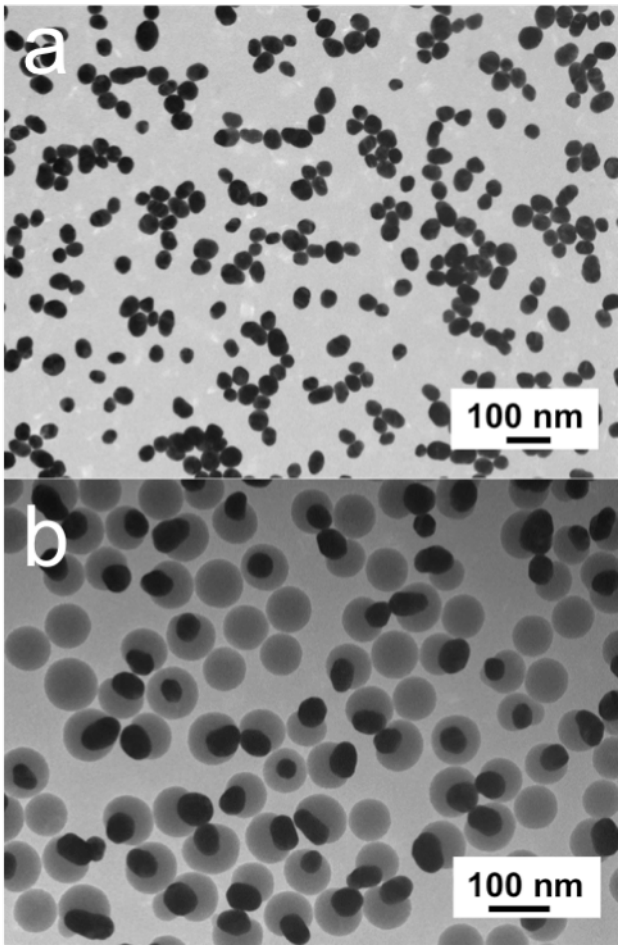

Figure 3.2. TEM imaging of Au and Au-SiO_2 nanoparticles

TEM images of (a) Au nanoparticles and (b) Au-SiO_2 nanoparticles.

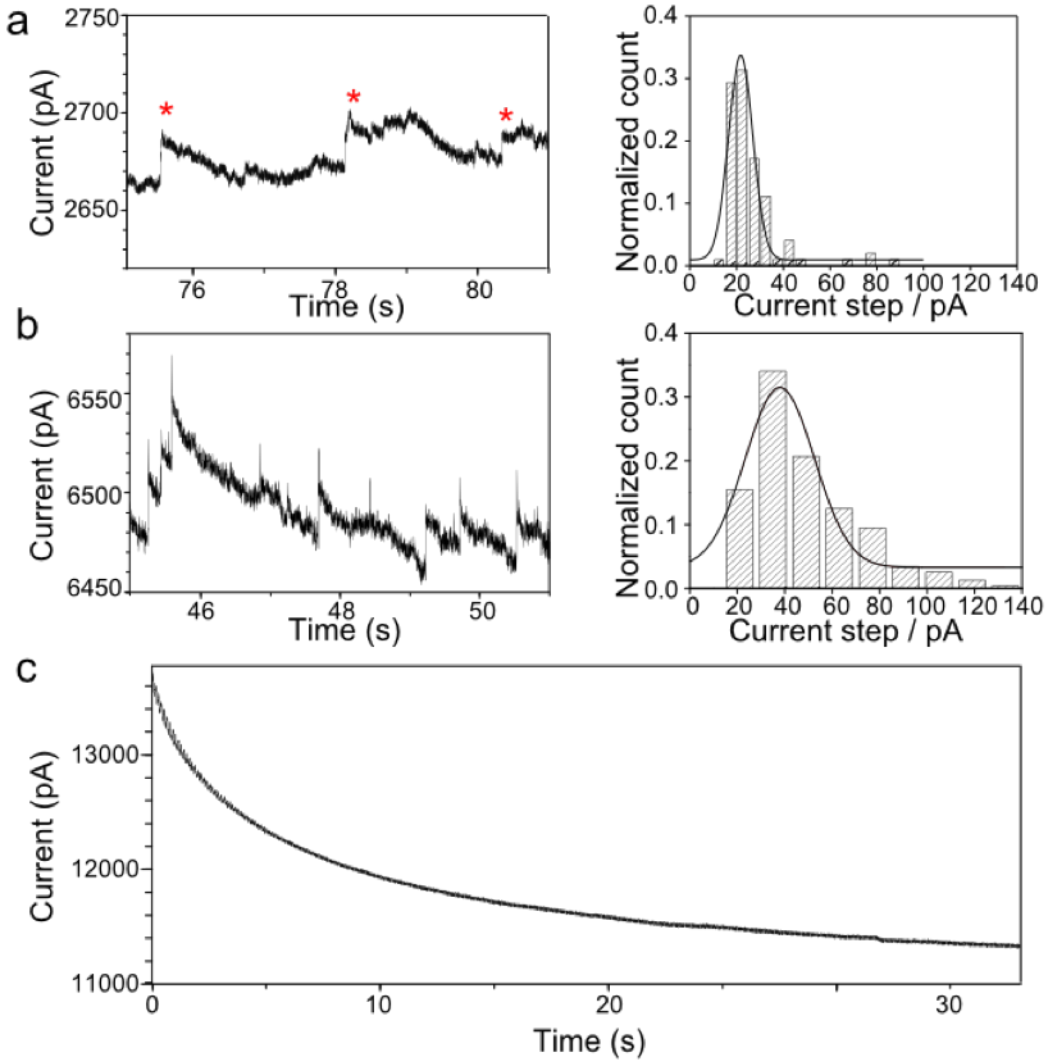

Figure 3.3. Current-time traces showing nanoparticle collision in hydrazine solution (Left panels) Representative current-time traces showing individual nanoparticle collision events recorded on a 5 µm CFE holding at 0.6 V vs. Ag/AgCl in solutions containing 15 mM hydrazine, 5 mM PB (pH 7.4) and (a) 2.1 pM Au-SiO2 nanoparticles (b) 2.1 pM Au nanoparticles. (Right panels) The corresponding histograms of current steps with Gaussian fitting. The counts were divided by total number of counts to get the normalized counts. (c) Current-time trace recorded on a 5 µm CFE holding at 0.6 V vs. Ag/AgCl in solutions containing 15 mM hydrazine and 5 mM PB.

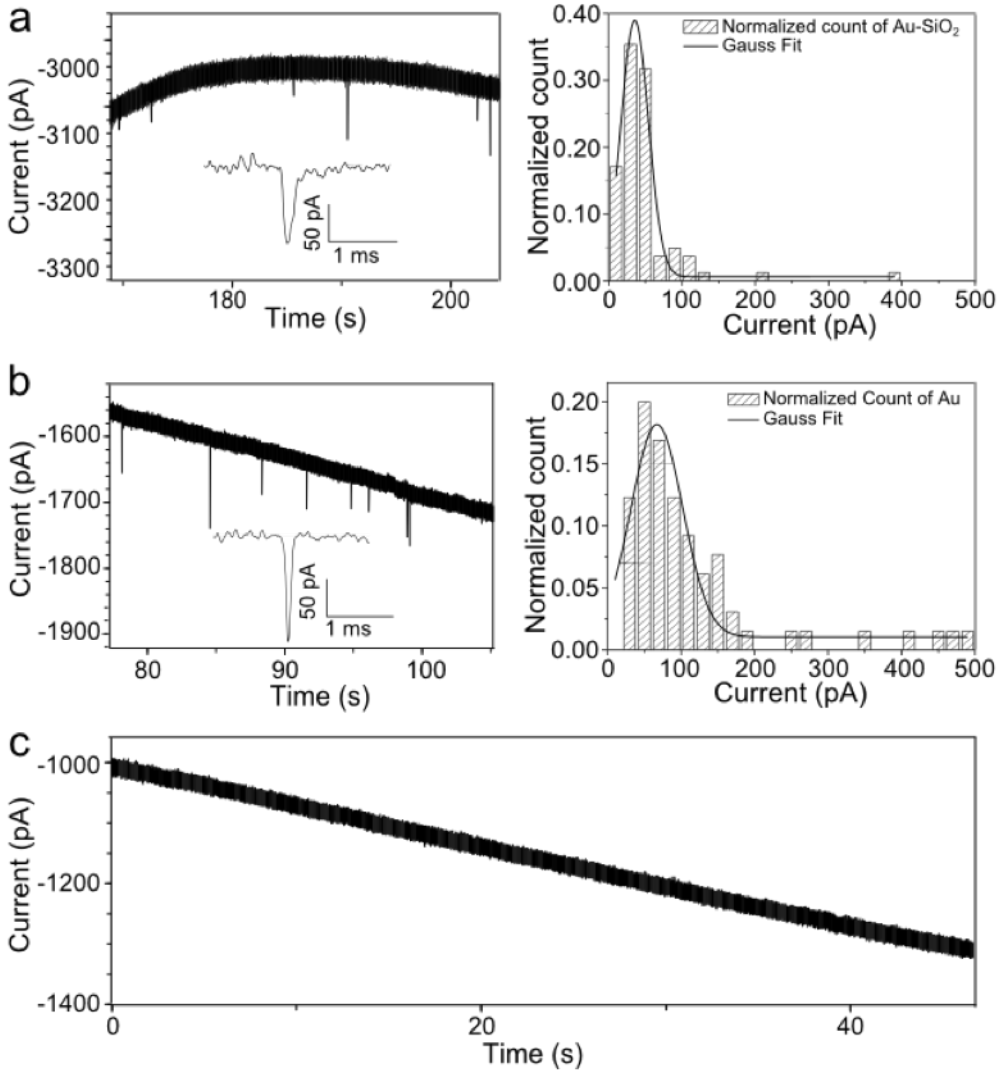

Figure 3.4. Current-time traces showing nanoparticle collision in $NaC_6H_7O_7$ solution (Left panels) Representative current-time traces showing individual nanoparticle collision events recorded on a 5 μm CFE holding at -0.8 V vs. Ag/AgCl in solutions containing 50 mM sodium dihydrogencitrate and (a) 2.1 pM Au-SiO_2 nanoparticles (b) 2.1 pM Au nanoparticles. (Right panels) The corresponding histograms of current steps with Gaussian fitting. The counts were divided by total number of counts to get the normalized counts. c) Current-time trace recorded on a 5 μm CFE holding at -0.8 V vs. Ag/AgCl in solutions containing 50 mM sodium dihydrogencitrate.

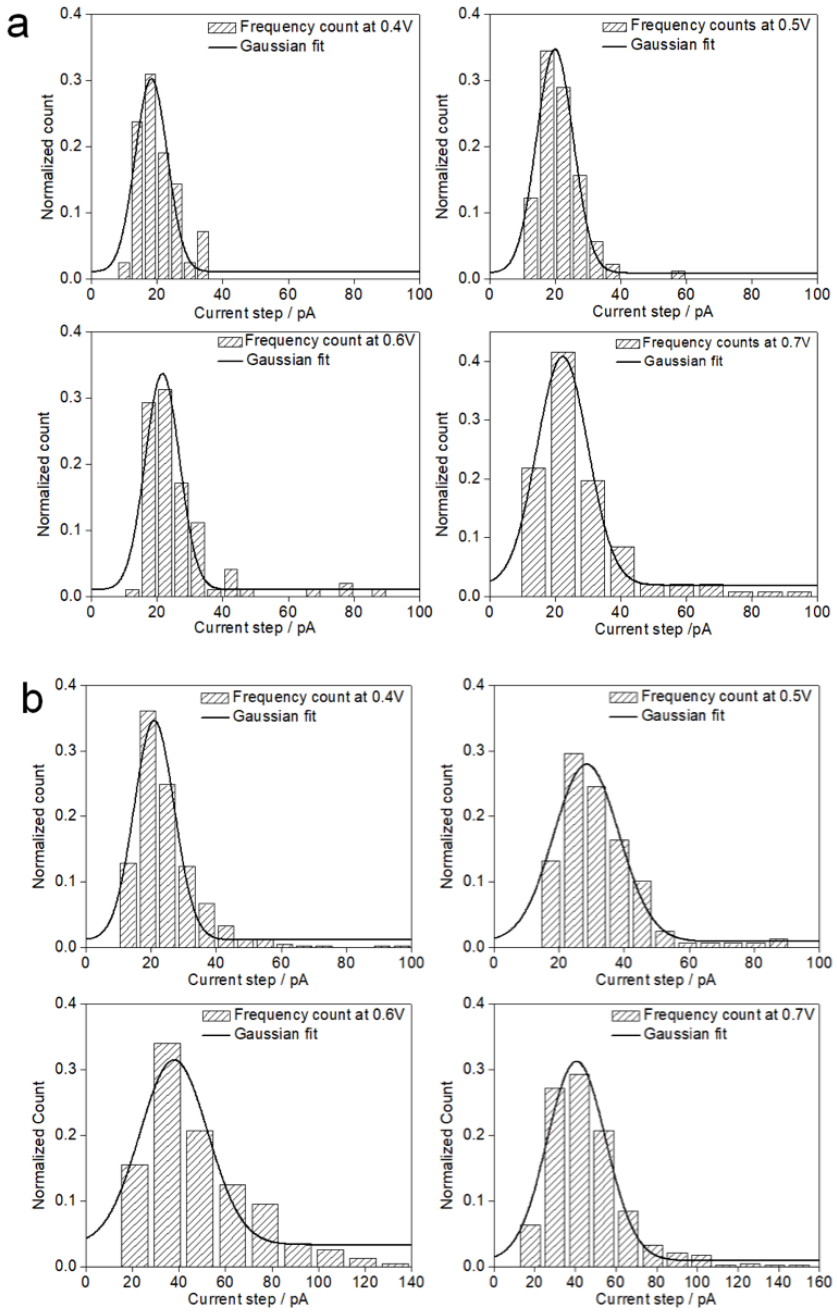

Figure 3.5. Current steps of Au and Au-SiO_2 nanoparticle at different potentials

Current distributions of (a) Au-SiO_2 nanoparticles and (b) Au nanoparticles at different potentials.

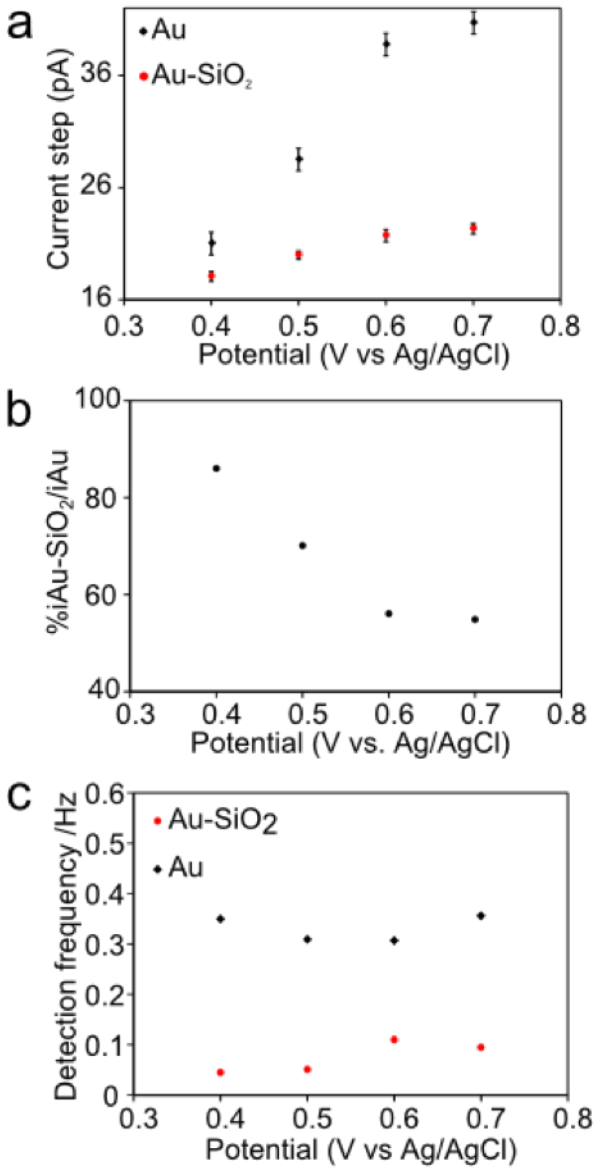

Figure 3.6. Current steps and detection frequency of Au and Au-SiO_2 nanoparticles (a) Average current steps of Au (black dots) and Au-SiO_2 (red dots) nanoparticles vs. applied potential. The average values and error bars are from Gaussian fitting. (b) Percent ratio of average current step of Au-SiO_2 nanoparticles to current step of Au nanoparticles vs. applied potential. (c) The collision frequency of Au-SiO_2 nanoparticles and Au nanoparticles vs. applied potential. The concentrations of Au-SiO_2 nanoparticles and Au nanoparticles in the solution are both 2.1 pM. The error bars are standard errors.

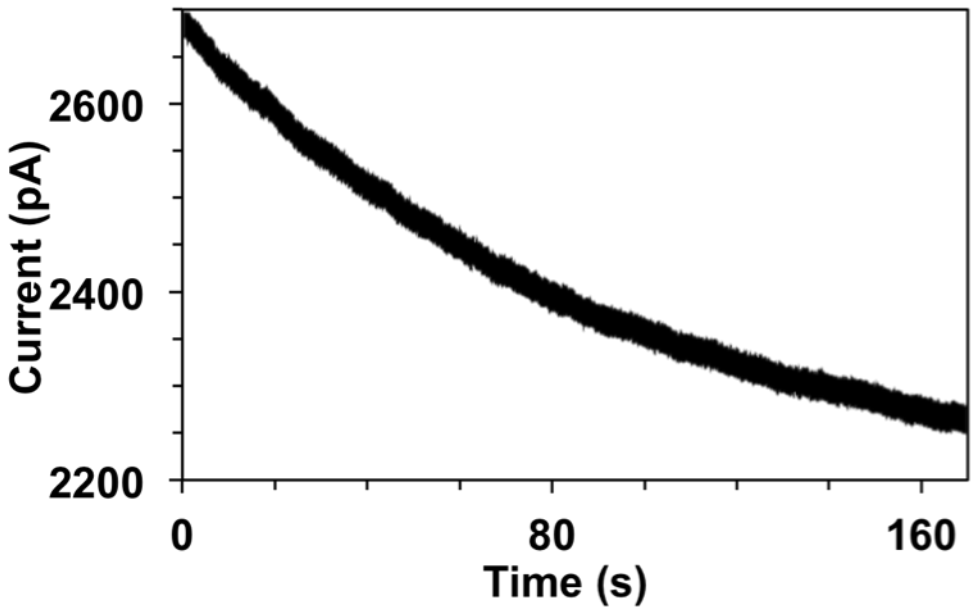

Figure 3.7. Current-time trace recorded with Au-SiO_2 at 0.3 V

Representative current-time trace recorded on a 5 μm carbon fiber electrode holding at 0.3 V vs. Ag/AgCl. The solution contains 15 mM hydrazine, 5 mM phosphate buffer at pH 7.4, and 12.5 pM Au-SiO_2 nanoparticles. No obvious current steps could be detected.

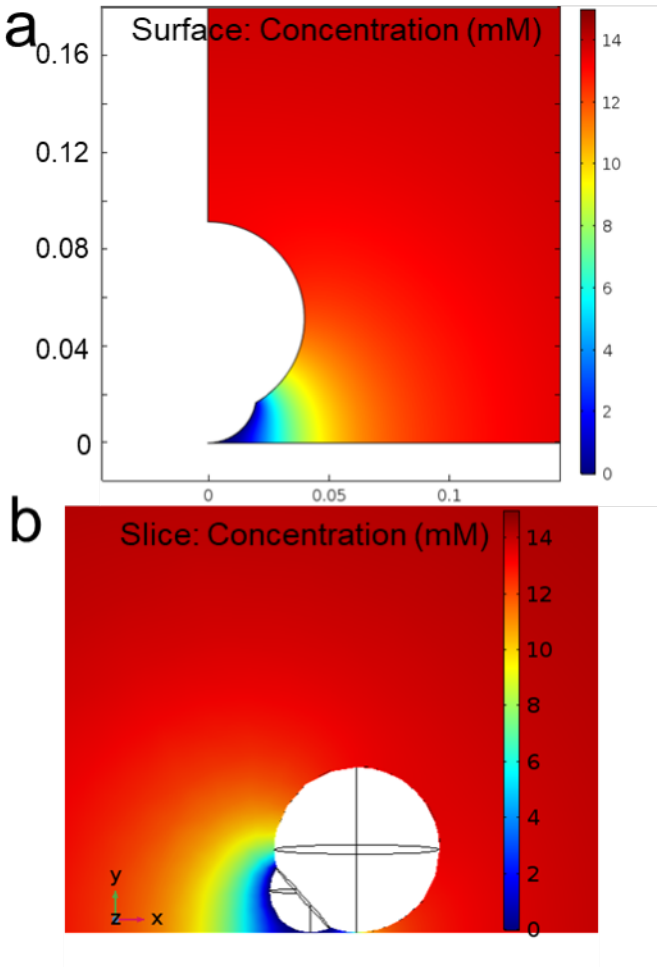

Figure 3.8. Simulated concentration profiles of hydrazine on a single Au-SiO_2 nanoparticle Simulated steady-state concentration profile of hydrazine on a single Au-SiO_2 nanoparticle (h = 28 nm) with two different orientations on the carbon electrode surface: (a) SiO_2 side facing up (b) SiO_2 side down. The radius of Au and SiO_2 spheres is 20 nm and 40 nm, respectively.

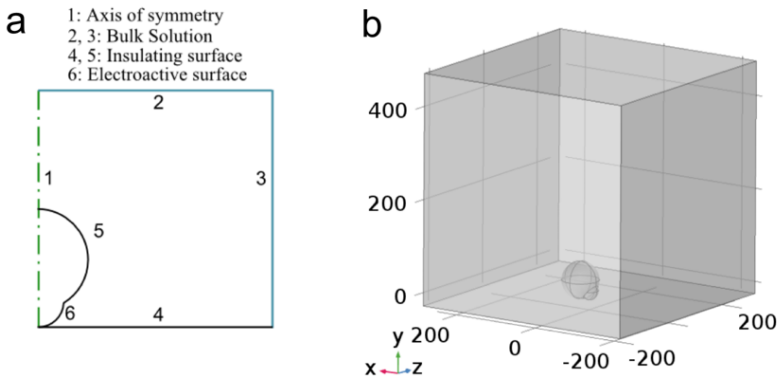

Figure 3.9. Numeric simulation model of a Au-SiO_2 particle on electrode surface

(A) 2D axial-symmetry geometry of the nanoparticle used in the finite-element simulation. (B) 3D model showing the different surfaces where only the Au surface is electroactive. The dimensions are not in scale. The geometry and boundary conditions for the simulation of the diffusion-limited faradaic current on a Au-SiO_2 nanoparticle are as following.

A 2D axial-geometry system (cylindrical coordinate) was used to simulate hydrazine oxidation on the exposed Au surface when the SiO_2 side is facing up. The geometry is shown in Figure 3.9a. In the case where the SiO_2 is facing down and Au is still making contact with the electrode surface, since the structure is not symmetrical, we built a 3D model as shown in Figure 3.9**b**. To simplify the simulation, the Au-SiO_2 particle was assumed to be composed of two spheres that represent Au and SiO_2. The radius of Au sphere was set to be 20 nm and the radius of SiO_2 sphere was set to be 40 nm. The overlapping distance between Au and SiO_2 sphere (h) was varied and the corresponding current was shown in Table S1. To meet the semi-infinite condition of the experiment, the boundary of the bulk solution in the model was extended to a distance of 20 μm away from the electrode surface. The Au surface and SiO_2 surface were defined as uncharged insulating boundary with no flux, to simplify the simulation. The surface concentration of hydrazine on exposed Au surface was set to be 0 mM. The concentration of hydrazine in the bulk was set to be 15 mM.

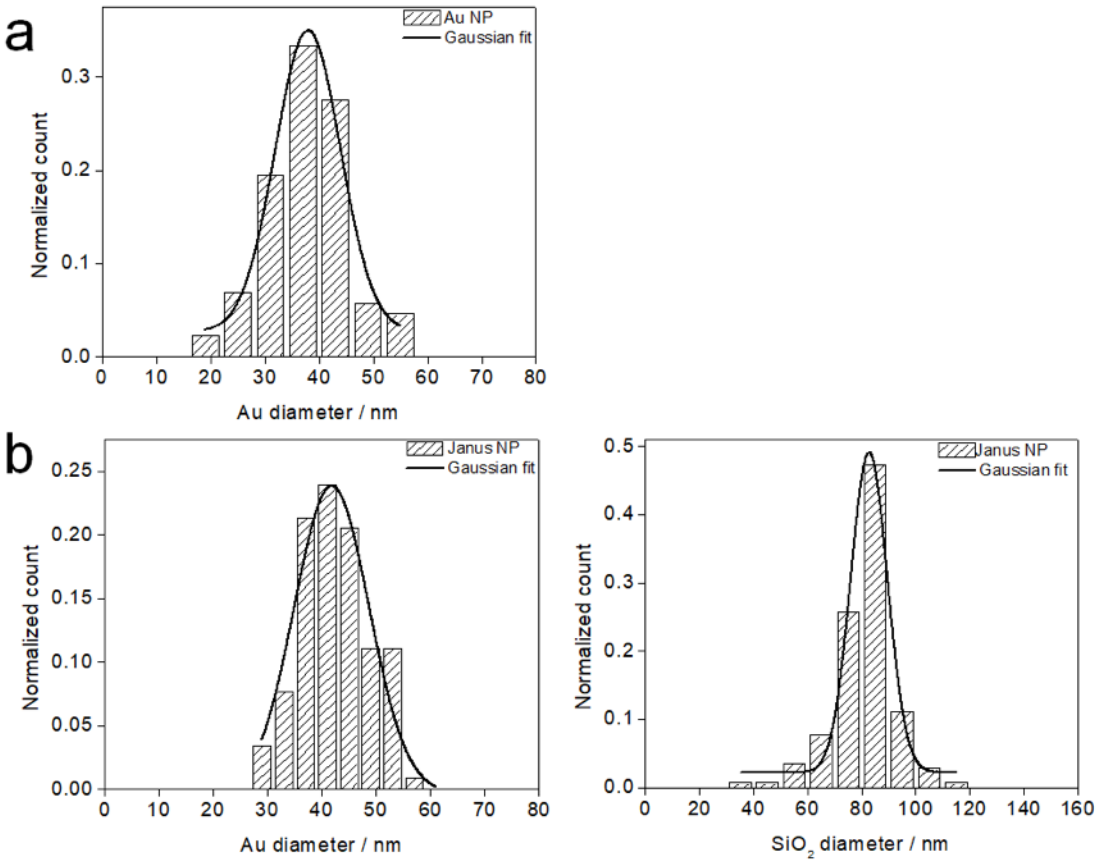

Figure 3.10. Size distributions of Au and Au-SiO_2 nanoparticles

Size distributions of (a) Au nanoparticles and (b) Au component and SiO_2 component of Au-SiO_2 nanoparticles. The average size of the Au particle is 38.00 ± 0.48 nm. The average diameter of the Au sphere component of Au-SiO_2 particle is 41.85 ± 0.72 nm, the SiO_2 sphere has an average diameter of 82.84 ± 0.45 nm.

3.8 REFERENCES

(1) Zhang, J.; Grzybowski, B. A.; Granick, S. Janus Particle Synthesis, Assembly, and Application. *Langmuir* **2017**, *33*, 6964-6977.

(2) Kaewsaneha, C.; Tangboriboonrat, P.; Polpanich, D.; Eissa, M.; Elaissari, A. Janus colloidal particles: preparation, properties, and biomedical applications. *ACS Appl. Mater. Interfaces* **2013**, *5*, 1857-1869.

(3) Jiang, Z.; He, J.; Deshmukh, S. A.; Kanjanaboos, P.; Kamath, G.; Wang, Y.; Sankaranarayanan, S. K. R. S.; Wang, J.; Jaeger, H. M.; Lin, X. M. Subnanometre ligand-shell asymmetry leads to Janus-like nanoparticle membranes. *Nat. Mater*. **2015**, *14*, 912-917.

(4) Grzelczak, M.; Vermant, J.; Furst, E. M.; Liz-Marzán, L. M. Directed self-assembly of nanoparticles. *ACS Nano*. **2010**, *4*, 3591-3605.

(5) Pradhan, S.; Ghosh, D.; Chen, S. Janus Nanostructures Based on Au−TiO_2 Heterodimers and Their Photocatalytic Activity in the Oxidation of Methanol. *ACS Appl. Mater. Interfaces* **2009**, *1*, 2060-2065.

(6) Kuttiyiel, K. A.; Sasaki, K.; Park, G.-G.; Vukmirovic, M. B.; Wu, L.; Zhu, Y.; Chen, J. G.; Adzic, R. R. Janus structured Pt–FeNC nanoparticles as a catalyst for the oxygen reduction reaction. *Chem. Commun.* **2017**, *53*, 1660-1663.

(7) Qin, W.; Peng, T.; Gao, Y.; Wang, F.; Hu, X.; Wang, K.; Shi, J.; Li, D.; Ren, J.; Fan, C. Catalysis-driven self-thermophoresis of Janus plasmonic nanomotors. *Angew. Chem. Int. Ed.* **2017**, *56*, 515-518.

(8) Peng, F.; Tu, Y.; van Hest, J. C. M.; Wilson, D. A. Self- Guided Supramolecular Cargo- Loaded Nanomotors with Chemotactic Behavior towards Cells. *Angew. Chem.* **2015**, *127*, 11828-11831.

(9) Wilson, D. A.; Nolte, R. J. M.; van Hest, J. C. M. Autonomous movement of platinum-loaded stomatocytes. *Nat. Chem.* **2012**, *4*, 268-274.

(10) Sanchez, A.; Díez, P.; Martínez-Ruíz, P.; Villalonga, R.; Pingarron, J. M. Janus Au-mesoporous silica nanoparticles as electrochemical biorecognition-signaling system. *Electrochem. Commun.* **2013**, *30*, 51-54.

(11) Biji, P.; Patnaik, A. Interfacial Janus gold nanoclusters as excellent phase-and orientation-specific dopamine sensors. *Analyst*, **2012**, *137*, 4795-4801.

(12) Sotiriou, G. A.; Hirt, A. M.; Lozach, P. Y.; Teleki, A.; Krumeich, F.; Pratsinis, S. E. Hybrid, silica-coated, Janus-like plasmonic-magnetic nanoparticles. *Chem. Mater.* **2011**, *23*, 1985-1992.

(13) Hu, H.; Ji, F.; Xu, Y.; Yu, J.; Liu, Q.; Chen, L.; Chen, Q.; Wen, P.; Lifshitz, Y.; Wang, Y.; Zhang, Q.; Lee, S.-T. Reversible and precise self-assembly of Janus metal-organosilica nanoparticles through a linker-free approach. *ACS Nano.* **2016**, *10*, 7323-7330.

(14) Walther, A.; Müller, A. H. E. Janus particles: synthesis, self-assembly, physical properties, and applications. *Chem. Rev.* **2013**, *113*, 5194-5261.

(15) Pradhan, S.; Xu, L.; Chen, S. Janus nanoparticles by interfacial engineering. *Adv. Funct. Mater.* **2007**, *17*, 2385-2392.

(16) Oja, S. M.; Fan, Y.; Armstrong, C. M.; Defnet, P.; Zhang, B. Nanoscale electrochemistry revisited. *Anal. Chem.* **2016**, *88*, 414-430.

(17) Quinn, M.; van't Hof, P. G.; Lemay, S. G. Time-resolved electrochemical detection of discrete adsorption events. *J. Am. Chem. Soc.* **2004**, *126*, 8360-8361.

(18) Kim, B.-K.; Boika, A.; Kim, J.; Dick, J. E. Bard, A. J. Characterizing Emulsions by Observation of Single Droplet Collisions-Attoliter Electrochemical Reactors. *J. Am. Chem. Soc.* **2014**, *136*, 4849-4852.

(19) Xiao, X.; Bard, A. J. Observing single nanoparticle collisions at an ultramicroelectrode by electrocatalytic amplification. *J. Am. Chem. Soc.* **2007**, *129*, 9610-9612.

(20) Xiao, X.; Fan, F. R. F.; Zhou, J.; Bard, A. J. Current transients in single nanoparticle collision events. *J. Am. Chem. Soc.* **2008**, *130*, 16669-16677.

(21) Oja, S. M.; Robinson, D. A.; Vitti, N. J. V.; Edward, M. A.; Liu, Y.; White, H. S.; Zhang, B. Observation of multipeak collision behavior during the electro-oxidation of single Ag nanoparticles. *J. Am. Chem. Soc.* **2017**, *139*, 708-718.

(22) Hao, R.; Fan. Y.; Zhang, B. Imaging Dynamic Collision and Oxidation of Single Silver Nanoparticles at the Electrode/Solution Interface. *J. Am. Chem. Soc.* **2017**, *139*, 12274-12282.

(23) Lebegue, E.; Anderson, C. M.; Dick, J. E.; Webb, L. J.; Bard, A. J. Electrochemical detection of single phospholipid vesicle collisions at a Pt ultramicroelectrode. *Langmuir* **2015**, *31*, 11734-11739.

(24) Frens, G. Controlled nucleation for the regulation of the particle size in monodisperse gold suspensions. *Nature Phys. Sci.* **1973**, *241*, 20-22.

(25) Chen, T.; Chen, G.; Xing, S.; Wu, T.; Chen, H. Scalable Routes to Janus Au−SiO_2 and Ternary Ag−Au−SiO_2 Nanoparticles. *Chem. Mater.* **2010**, *22*, 3826-3828.

(26) Strein, T. G.; Ewing, A. G. Characterization of submicron-sized carbon electrodes insulated with a phenol-allylphenol copolymer. *Anal. Chem.* **1992**, *64*, 1368-1373.

(27) Luo, Y.; Geng, S.; Dube, L.; Zhao, J. Tuning the Valency of Heterogeneous Au–Silica Nanostructure via Controlled Ostwald Ripening Process. *J. Phys. Chem. C.* **2018**, *122*, 18077-18085.

(28) Kahk, J. M.; Rees, N. V.; Pillay, J.; Tshikhudo, R.; Vilakazi, S.; Compton, R. G. Electron transfer kinetics at single nanoparticles. *Nano Today*, **2012**, *7*, 174-179.

(29) Kwon, S. J.; Zhou, H.; Fan, F.-R. F.; Vorobyev, V.; Zhang, B.; Bard, A. J. Stochastic electrochemistry with electrocatalytic nanoparticles at inert ultramicroelectrodes—theory and experiments. *Phys. Chem. Chem. Phys.* **2011**, *13*, 5394-5402.

(30) Percival, S. J.; Zhang, B. Fast-Scan Cyclic Voltammetry Allows Determination of Electron-Transfer Kinetic Constants in Single Nanoparticle Collision. *J. Phys. Chem. C.* **2016**, *120*, 20536-20546.

(31) Karp, S.; Meites, L. The voltammetric characteristics and mechanism of electroöxidation of hydrazine. *J. Am. Chem. Soc.* **1962**, *84*, 906-912.

(32) Guo, Z.; Percival, S. J.; Zhang, B. Chemically resolved transient collision events of single electrocatalytic nanoparticles. *J. Am. Chem. Soc.* **2014**, *136*, 8879-8882.

(33) Park, J. H.; Boika, A.; Park, H. S.; Lee, H. C.; Bard, A. J. Single collision events of conductive nanoparticles driven by migration. *J. Phys. Chem. C.* **2013**, *117*, 6651-6657.

(34) Boika, A.; Thorgaard, S. N.; Bard, A. J. Monitoring the electrophoretic migration and adsorption of single insulating nanoparticles at ultramicroelectrodes. *J. Phys. Chem. B*. **2013**, *117*, 4371-4380.

Chapter 4. OBSERVING TRANSIENT BIPOLAR ELECTROCHEMICAL COUPLING OF SINGLE NANOPARTICLES TRANSLOCATING THROUGH A NANOPORE

This chapter is mostly adapted from the manuscript: Han, C.; Hao, R.; Fan, Y.; Zhang, B. "Observing Transient Bipolar Electrochemical Coupling on Single Nanoparticles Translocating through a Nanopore", in revision.

4.1 ABSTRACT

We report the observation of transient bipolar electrochemical coupling on freely-moving 40 nm silver nanoparticles. The use of an asymmetric nanoelectrochemical environment at the nanopore orifice, e.g., an acid inside the pipette and halide ions in the bulk, enabled us to observe unusually large current blockages of single Ag nanoparticles. We attribute these current blockages to the formation of H_2 nanobubbles on the surface of translocation of Ag nanoparticles due to the coupled faradaic reactions, in which the reduction of protons and water is coupled to the oxidation of Ag and water under potentials higher than 1 V. The appearance of large current blockages was strongly dependent on voltage and the choice of anions in the bulk solution. The correlation between large current blockages with the oxidation of Ag nanoparticles and their nanopore translocation was further confirmed by simultaneous fluorescence and electric recordings. This study demonstrates that transient bipolar electrochemistry can take place on small metal nanoparticles below 50 nm when they pass through nanopores where the electric field is highly localized. The use of a nanopore and the resistive-pulse sensing method to study transient bipolar electrochemistry of nanoparticles may be extended to the future studies in ultrafast

electrochemistry, nanocatalyst screening, and gas nucleation on nanoparticles.

4.2 INTRODUCTION

The ability to observe and study stochastic transient faradaic responses of single molecules and nanoparticles is important to a wide range of applications ranging from developing a deeper understanding of the chemical and physical processes at the electrode/solution interface to designing highly advanced biochemical sensors. One of the key challenges, however, has been the direct recording of ultrasmall faradaic signals from a large electric noise with sufficient bandwidth.[1,2] To this end, several innovative approaches have been taken to amplify the signal of single molecules and nanoparticles. These include the use of redox cycling to allow repeated oxidation and reduction of a same molecule on two closely-spaced nanoelectrodes,[3-6] the use of a nanopore to measure a change in its ionic conductance caused by the passage of a molecule[7-9] or nanoparticle,[10-13] and the use of various optical methods for signal amplification. Popular optical methods include dark-field scattering microscopy,[14-16] fluorescence,[17-21] and surface plasmon resonance.[22-24]

The method of nanoparticle collision[25] or nanoparticle impact electrochemistry[26] is particularly useful in studying transient electrochemical events of single nanoparticles and even single molecules. Depending on the system of interest, one can use an ultramicroelectrode (UME) to measure a decay in its faradaic signal when an electrochemically inactive particle adsorbs on the electrode blocking the flux of a redox mediator.[27,28] Alternatively, a current increase can be seen when a catalytically[29,30] (or electrochemically[31-33]) active particle lands on the electrode enhancing the faradaic reaction of a redox mediator (or reacting itself in the case of an electroactive particle).

Bipolar electrochemistry is the study of electrochemical processes on a piece of conductive

material placed inside an electrolyte solution without making direct ohmic contact to the driving electrodes.[34] Faradaic reactions are driven on the two extremities of the same bipolar electrode when a sufficiently high voltage is applied from a pair of driving electrodes. The concept of bipolar electrochemistry has been widely used in numerous fields ranging from electrochemical analysis in microfluidic channels,[35-37] electrocatalytic screening,[38,39] electrochemical imaging,[40-42] and motions of self-powered micro-objects.[43,44] Kuhn and others have used bipolar electrochemistry and electrodeposition to fabricate asymmetric particles.[45-47] Such experiments, however, often require the use of micron-sized objects in order to exert sufficient potential drop across the particle length.[46,48] Stockmann et al. have reported an interesting study in which they observed collision events of single Pt nanoparticle at the interface between two immiscible solutions.[49]

Here, we report the observation of transient bipolar electrochemical coupling on individual 40 nm silver nanoparticles during their translocation through a quartz nanopipette. This study uses the method of resistive-pulse sensing in which one uses a micron-sized or nanometer-sized pore to observe fast translocation events of individual nanoparticles or even small molecules.[7] In resistive-pulse sensing, the transient presence of a nanoparticle at the pore orifice during its translocation induces a large increase in the pore's ionic resistance, which is detected as a sudden current drop.[12] The nanopore current returns to the baseline after the particle leaves the nanopore.

This study exploits the highly focusing power of a nanopipette pore for the applied voltage: when a small voltage (e.g., 2 V) is applied between two driving electrodes placed in and outside of the pipette, the majority of the applied voltage is dropped across the pipette pore.[11] Therefore, when a conductive nanoparticle, e.g., 40 nm Ag, moves to the vicinity of the pore orifice, a sufficiently high voltage is dropped across the nanoparticle so that two separate redox reactions can be coupled on the two extremities of the same nanoparticle. Here, we use quartz pipettes of

~63 nm in diameter to study translocation events of 40 nm Ag nanoparticle under a small constant DC voltage ≤ 2.5 V. By establishing an asymmetric chemical environment at the pipette pore orifice, e.g., placing an HCl-filled nanopipette into a solution of 10 mM KCl, and applying a proper DC voltage across the pipette pore, we observed unusually large current blockages, which we attribute to the translocation of single Ag nanoparticles inducing transiently coupled electrochemical reactions. Here, we believe the reduction of protons and water is coupled to the oxidation of Ag along with possible electrocatalytic oxidation of water under high potentials.[50] Reduction of protons and water generates molecular H_2, which nucleates into small nanobubbles in a highly confined space where molecular diffusion may be significantly hindered. Various conditions, e.g., different voltages and different anionic species, were studied toward large current blockage events. Simultaneous fluorescence and electric recordings were also performed to confirm that the large blocking events were correlated with the oxidation of individual Ag nanoparticles and their translocation through pipette pore.

To the best of our knowledge, this is the first time transient bipolar electrochemical response is observed on single freely diffusing nanoparticles below 50 nm during their nanopore translocation. Bipolar electrochemical coupling is obtained on small Ag particles due to the highly focusing power of a nanopipette pore to the applied voltage, which enables sufficient voltage drop across a single nanoparticle. Moreover, the use of the resistive-pulse method and the generation of a gas nanobubble allow the impact of the redox coupling to be greatly amplified. The use of a nanopore and resistive-pulse sensing to study transient bipolar electrochemistry of nanoparticles may have wide implications for future research in ultrafast electrochemical phenomena, high-throughput nanocatalyst screening, gas nucleation on nanoparticle surfaces, and preparation and use of Janus nanoparticles by asymmetric electrodeposition.

4.3 EXPERIMENTAL SECTION

4.3.1 *Chemicals and Materials*

All the following chemicals and materials were used as received from the manufacturers. Potassium chloride (KCl, Fisher Chemical, 99.1%), hydrochloric acid (HCl, Fisher Scientific, 1N), perchloric acid ($HClO_4$, Sigma-Aldrich, 70%), sodium perchlorate monohydrate ($NaClO_4 \cdot H_2O$, Fluka Analytical, >99.0%), sodium bromide (NaBr, Aldrich, >99%), 40 ± 4 nm diameter Ag nanoparticles and 42 ± 5 nm diameter gold nanoparticles (sodium citrate capped, dispersed in 2 mM citrate, nanoComposix). All aqueous solutions were prepared using deionized water (>18 MΩ cm) from a Barnstead Nanopure water purification system.

4.3.2 *Fabrication and Characterization of Nanopipettes*

Quartz nanopipettes of ~63 nm diameter were prepared by pulling quartz capillaries (0.5 mm I.D./1.0 mm O.D., with filament) on a P-2000 laser puller (Sutter) with a two-line pulling program: heat = 725, filament = 4, velocity = 20, delay = 128, pull = 0; heat = 670, filament = 4, velocity = 90, delay = 140, pull = 100. The diameter of the pipette pore was calculated from the ionic resistance measured in 0.1 M KCl solution at room temperature (Figure 4.1a).[51,52] The average size of the pipettes was calculated to be 63.3 ± 1.8 nm from a group of 19 nanopipettes.

4.3.3 *Scanning Electron Microscopy (SEM) Characterization*

SEM imaging (Figure 4.1b) was performed on a FEI XL830 Dual Beam system operating at a 5 kV accelerating potential. The sample was coated with a thin layer of carbon by sputtering.

4.3.4 *Cell Configuration and Data Acquisition*

All the electrochemical experiments were performed using a Dagan potentiostat (Chem-

Clamp, Dagan). Amperometry data were recorded on a Dell PC through a Digidata 1322A digitizer (Axon Instruments). The low-pass filter was set to 3 kHz. Amperometric traces were recorded using Axoscope 10.4 software (Molecular Devices) with a 50 kHz rate of data recording. All experiments were performed using a two-electrode setup placed in a lab-built Faraday cage. All potentials reported herein are with respect to a Ag quasi reference electrode inside the capillary versus a Pt quasi reference electrode in the bulk solution on the exterior of the pipette pore.

4.3.5 *Fluorescence Imaging*

A nanopipette filled with 0.1 M HCl was immersed in a drop of solution containing 10 mM NaBr and 0.8 pM 40 nm Ag nanoparticles and placed nearly horizontally (angle between the nanopipette and coverslip was about 10°) on a coverslip on an Olympus IX70 inverted microscope for observation (Figure 4.2). Nanoparticle translocation events were captured with fluorescence imaging. The excitation source was a solid-state 532 nm green laser (CrystaLaser) emitting at 10 mW configured for epifluorescence. The fluorescence signal was collected by a 60× 1.49 NA objective (Olympus Apo N) and optically filtered using an ET610/75m emission filter (Chroma Technology). An additional 1.5× magnification on the microscope was used. An Electron Multiplying Charge-Coupled Device (EMCCD) camera (iXon 897, Andor) cooled to -85 °C and Andor SOLIS software were used to record all images. Images were recorded using an exposure time of 50 ms (frame rate: 19.81 Hz), as indicated in the article. An amplifier gain of 20 as well as a preamplifier gain of 5.1 were used. The voltage was generated and current measured using a Dagan Chem-Clamp connected to a Digidata 1322A digitizer operating at 50 kHz.

4.3.6 *Finite Element Simulations*

Numerical simulations of the distributions of the electric field and the electrostatic potential of a 60 nm pipette pore, the nanopore's ionic current with a nanoparticle placed at various locations, and the nanopore's ionic current with a nanoparticle/nanobubble ensemble were performed using COMSOL Multiphysics 5.2a (COMSOL Inc., Burlington, MA).

4.4 Results and Discussion

4.4.1 *Nanoparticle Translocation and Potential-Dependent Bipolar Coupling*

We used a nanopore-based approach (Figure 4.3) to study transient bipolar electrochemical response of single metal nanoparticles. A conductive nanoparticle translocating though a nanopore may behave like a nanometer-sized bipolar electrode under a properly aligned and sufficiently high electrostatic potential drop across the pore orifice. The nanoparticle may couple two separate redox reactions on its two extremities when the total voltage drop across that nanoparticle is equal to or exceeds a voltage requirement for coupling these reactions. This voltage, as previously described by us,[53] can be roughly estimated by the difference of the formal potentials of the two coupled redox reactions. Here, on the same Ag nanoparticle, the reduction of redox species, ***Ox'***, from inside the pipette is electrically coupled to the oxidation of another redox species, ***Red***, from the other side in the bulk solution.

We used a laser-pulled quartz nanopipette with an opening of ~63 nm determined from its ionic resistance to study Ag nanoparticles of 40 nm in diameter. The quartz pipette was filled with an aqueous solution of 100 mM HCl, and placed in a salt solution, e.g., 10 mM KCl, containing Ag nanoparticles at 8 pM. The relatively low salt concentration in the external solution was used

to reduce particle aggregation. The use of 100 mM HCl inside the pipette, on the other hand, is to provide a high concentration of protons, which will be electrochemically reduced to form a H_2 nanobubble when a Ag nanoparticle is transiently present at the pore orifice. Nanoparticle translocation from the bulk into the pipette pore was driven primarily by electrophoresis: a positive potential was applied from inside the pipette vs outside, which drives the citrate-capped, negatively charged Ag nanoparticles into the pipette. Individual translocation events were seen as sharp current spikes in the current-time trace, as shown in Figure 4.4a.

In the absence of Ag nanoparticles, a stable baseline current of 7.4 nA was recorded when a +1 V potential was applied across the pipette (Figure 4.5a), as expected. When 8.0 pM Ag nanoparticles was added in the bulk solution, however, sharp current spikes were observed in the current-time (*i*-*t*) trace, as shown in the left panel of Figure 4.4a. The number of current spikes detected per unit time (or particle detection frequency) increases linearly with particle concentration, which suggests that these current spikes were caused by particle translocation events. A representative current spike is given in Figure 4.4a as the inset. The average peak width at base was 30.5 ± 11.9 ms. The asymmetric triangular peak shape reflects the geometries of the conical pipette pore: the current drops sharply when the nanoparticle initially enters the narrow opening; the slow current increase is due to the particle moving toward the wider region of the pipette.[10] The average peak amplitude (ratio between the current blockage and the open pore current) was 4.1 ± 0.4% of the baseline current, as shown in the right panel of Figure 4.4a, in fair agreement with simulation (~5.5%, Figure 4.6). The smaller current blockage may be caused by additional conductance due to the surface charges on the pore walls and Ag nanoparticles, which was not considered in the simulation. Although the applied potential bias is not sufficient to form

a nanobubble (vide infra), the bipolar faradaic reactions draw additional current to the nanoparticle/nanopore, enhancing the apparent conductance of the nanopore.

Interestingly, we observed unusually large current spikes when the voltage bias was further increased. Figure 4.4b (left panel) is a 30-s i-t trace recorded when the applied voltage was increased to +2 V. The baseline current was around 24 nA due to the use of a larger voltage. In addition to the small current spikes (~4.1% of the open pore current), there were several very large current spikes reaching 30% of the open pore current. The right panel of Figure 4.4b is a histogram showing the distribution of the peak amplitude from 261 recorded particle events. Although more than half of the peaks are below 10% of the baseline current, a significant fraction of the events showed peak amplitude greater than 20% of the baseline. Many of these events have current drops even greater than 30% of the open pore current!

The appearance of large current blockage continued when the applied voltage was further increased to +2.5 V, as displayed in Figure 4.4c. Under such conditions, we observed very large current blockage events blocking >80% of the open pore current (Figure 4.4c). Moreover, we have observed a systematic change in the shape of the translocation peak with voltage (insets of Figure 4.4a, b, and c). Compared with peaks at 1 V, peaks at higher voltages are more symmetric in shape showing both a slow current decay and a slow increase after reaching the lowest current. These large blocking events were unexpected considering the same particles, solutions, and nanopores were used and the only parameter changed was an increase in the applied voltage. In resistive-pulse sensing, the ratio between the current blockage and the open pore current would not change when the applied voltage is changed because the current signal is mainly determined by the ratio between the volume of the particle and that of the nanopore ($V_{particle}/V_{pore}$).[54,12] As will be discussed in greater details in a later section, we believe the increase in peak amplitude and the change in the

peak shape are both resulted from the coupled electrochemical reactions on the translocating Ag nanoparticles increasing their apparent volume inside the nanopore.

4.4.2 *Anion-Dependent Bipolar Coupling*

The appearance of large current blockage is strongly dependent on the choice of the anionic species in the bulk solution. We found the use of halide anions, such as Cl^-, Br^-, which can promote Ag oxidation and dissolution by forming insoluble products with Ag^+, significantly increases the chance of observing such events. Figure 4.7 shows a direct comparison of three anionic species, ClO_4^-, Cl^-, and Br^-, all of which were at 10 mM, in their ability to promote large current blockages during translocation of 40 nm Ag nanoparticles through 63 nm pipette pore. The only difference between these three experiments was the anionic species present in the outer solution. As shown in Figure 4.7a, we were unable to observe large blockage events when ClO_4^- ions were used. On the other hand, large current blockages were observed with both Cl^- and Br^-. Moreover, more than 30% of the total translocation events in the Br^--containing solution had peak amplitude greater than 40% of the open pore current. Some of these peaks were even greater than 80% of the open pore current as seen from Figure 4.7c (right panel). The increased number of large blockage events in the Br^--containing solution and their large magnitude are consistent with our hypothesis that the reactivity of selected anionic species with Ag^+ may play a key role in observing such events.

We have analyzed the detailed characteristics of at least 50 individual large peaks (having current blockage >10% of the open pore current) in each condition and the results are presented in Figure 4.8. We used a typical current spike (Figure 4.8a) measured at +2 V in 10 mM Cl^- to define three key parameters: the decay time (the time it takes to reach the minimum current from the baseline), the rise time (the time it takes to return from the current minimum to the baseline), and the peak current. More representative large current spikes can be found in Figure 4.9. As shown in

Figure 4.8b, while the average current blockage was in agreement with nanoparticle size-based prediction (Figure 4.6) in ClO_4^- under both potentials, it increased drastically when Cl^- and Br^- were present in the bulk solution. Moreover, Br^- shows an increasing effect in enabling larger current blockages under each potential tested. The peak shape of the current spikes also changed dramatically when Cl^- and Br^- were used. A nanoparticle translocating into a conical pipette pore should generate an asymmetric triangle peak where the current drops sharply to the minimum followed by a slow increase to the initial baseline (inset of Figure 4.4a).[11] Interestingly, in the presence of Cl^- and Br^-, the current pulses became somewhat more symmetric showing a more sluggish current decay to the peak current followed by a slow increase back to the baseline. Moreover, both the decay time and the rise time were significantly longer than that in ClO_4^- under each potential. This trend is clearly seen from the change in the average decay time and the rise time (Figure 4.8c and d). There is a remarkably large contrast between the average decay times in these three solutions (Figure 4.8c): It took <1 ms and ~3 ms for a 40 nm Ag particle to enter the pipette pore in ClO_4^--containing solution at 2.0 and 2.5 V, respectively; When Cl^- ions were used, however, it took more than 25 ms and 65 ms for the particle to enter the pore at 2 and 2.5 V, respectively. Although not as dramatic as Cl^-, Br^- did cause the decay time to increase by a factor of at least 3 depending on the applied potential. Similarly, there was less of an effect when we examined the rise time caused by the addition of Cl^- and Br^- (Figure 4.8d).

It is well known that a transient current spike in conventional resistive-pulse sensing experiments is caused by an analyte particle excluding a certain volume of solution when it translocates through the sensing zone or a nanopore.[12] The magnitude of the current pulse is largely determined by the volume ratio between the analyte particle and the nanopore. Although the surface charge on the particle may affect the peak amplitude, its contribution is usually less

significant unless very low salt concentrations (e.g., μM) are used.[55] Based on our observation of the unusually large current blockage, it is reasonable to believe that there were certain (electro)chemical reactions taken place on the nanoparticle surface, which were triggered by the particle's translocation through a pipette pore and causing a large increase in the particle's apparent volume. We believe that the reduction of protons and water on one side of an Ag nanoparticle is coupled to the oxidation of silver on the other side of the same nanoparticle. In the presence of Cl^- or Br^- ions, Ag may be oxidized to form AgCl or AgBr (and Ag_2O), which may further catalyze the oxidation of H_2O molecules.[50] The reduction of protons and water leads to the formation of H_2 molecules, which nucleate and form a H_2 nanobubble increasing the apparent volume of the Ag nanoparticle causing a large current blockage. Although formation of insoluble silver halide species, such like AgCl and AgBr, could also affect the nanopore's ionic current, this effect may only cause a slight increase in the nanoparticle's apparent volume and a small change in the current blockage.

4.4.3 *Numeric Simulation and Analysis*

Based on this assumption, we can estimate the size of the nanobubble corresponding to a specific current spike using numerical simulation. We assume that a 40 nm Ag nanoparticle is located right at the orifice (the most sensitive zone) of a 60 nm pipette pore and a nanobubble of various sizes is formed on the top surface of the particle, as shown in Figure 4.10. Interestingly, the current blockage only increases slightly with bubble size when the bubble is smaller than 68 nm (corresponding to 20% current blockage). However, it increases drastically when the bubble grows larger than 70 nm. For example, a 74 nm nanobubble would cause a current blockage of 40% of the open pore current. A 76 nm bubble would cause an 80% current blockage. We note that this simulation is just a simple size estimation of the nanobubble because we do not know the exact

configuration of the particle/bubble ensemble. It is likely that the bubble sizes will be different when another geometry is adopted in simulation.

As illustrated in Figure 4.3, when Cl^- is present in the bulk, of all the possible reactions taken place on the Ag nanoparticle, the two most probable faradaic reactions coupled on the same particles are as following,

$$2H^+ + 2e^- \rightarrow H_2(g) \quad (4.1)$$

$$Ag + Cl^- \rightarrow AgCl(s) + e^- \quad (4.2)$$

Reaction 1 takes place on the surface of the nanoparticle toward the inside of the pipette and has a standard potential E^o of 0 V vs NHE. Reaction 2 is the oxidation of Ag in the presence of Cl- and proceeds on the other surface of nanoparticle, which has an E^o of 0.22 V vs NHE. Using the Nernst equation,[56] one can estimate the equilibrium potentials for reactions 1 and 2 to be -0.059 V and 0.338 V vs NHE, respectively, at experimental conditions. Therefore, the voltage needed to drive reactions 1 and 2 on the same particle would be 0.338 V– (-0.059 V) = 0.40 V at this condition. This voltage requirement can be met when a relatively large voltage is applied between the two driving electrodes, e.g., ≥ 2.0 V, because the majority of the voltage drop is concentrated near the pipette pore. To further iterate this key point, Figure 4.11 illustrates the simulated spatial distributions of the electric field and electrostatic potential near to the pipette pore in the absence of a nanoparticle, which shows that out of the 2.0 V total applied voltage, ~1.2 V voltage is dropped within a distance of ~200 nm near to the nanopore orifice. One can also estimate the voltage across a 40 nm Ag particle using the length of the particle and the electric field (*Voltage = Length × Field Strength*). At the peak value of the electric field ~14×10^6 V/m (Figure 4.11), the estimated voltage across a 40 nm particle is 0.56 V. This voltage focusing effect may become even more significant

when a nanoparticle is present at the pore orifice leading to an even higher voltage drop across the particle due to an increased pore resistance.

When Br^- is used in the bulk, equation 4.2 becomes $Ag + Br^- \rightarrow AgBr\ (s) + e^-$, which has an E^o of 0.071 V vs NHE and an equilibrium potential of 0.19 V vs NHE at experimental conditions. Therefore, the voltage needed to drive proton reduction and Ag oxidation on the same particle would be 0.19 V– (-0.059 V) = 0.25 V at this condition. This voltage requirement can be satisfied even more easily compared to when Cl^- is used. Although the majority of the oxidized Ag should form AgCl or AgBr, some Ag may form Ag_2O which can further catalyze the oxidation of water molecules as previously reported by our group.[50] In another recent paper,[57] our group showed that H_2 nanobubbles could be formed in electrocatalytic water splitting under ~700 mV, far before reaching water's thermodynamic reduction potential. Therefore, it is reasonable to believe that water molecules may also be reduced and oxidized on the cathodic and anodic pole, respectively, during particle translocation.

It is interesting to note that only a small fraction of the resistive pulses showed current blockage greater than 20% of the open pore current at 2.0 V. When the applied voltage was increased to 2.5 V, more of such large blocking events were seen, which was caused by a higher voltage dropped across the two extremities of the same Ag nanoparticle driving the coupled redox reactions at a higher rate. The fact that not every particle translocation event leads to a large current blockage may indicate that either Ag nanoparticles are quite heterogeneous in their electrochemical activity or they may be different in their ability to nucleate a stable H_2 nanobubble during particle translocation. The effective redox coupling and bubble generation may require nanoparticles of certain size, shape, or electrochemical reactivity to be present at the pore orifice.

A noticeable change was observed in the i-t trace as we changed the identity of the anionic species from ClO_4^-, which does not form an insoluble complex with Ag^+, to Cl^- and Br^- (Figure 4.7), which react with Ag^+ to form AgCl and AgBr. When ClO_4^- is used, equation 4.2 becomes $Ag = Ag^+ + e^-$, which has an E^o of 0.80 V vs NHE, ~0.58 V higher than when Cl^- is used and ~0.73 V higher than when Br^- is used. As such, the voltage drop across a single Ag nanoparticle may not be sufficient to drive the oxidation of Ag and reduction of protons to a high-enough rate to cause bubble generation. Indeed, the increased number of large blocking events in Br^--containing solutions (Figure 4.7) is in agreement with our analysis of the bipolar electrochemical coupling.

With the understanding that the large current blockage is caused by formation of a H_2 nanobubble on the surface the Ag nanoparticle, it is interesting to re-examine the effect of halide ions on the decay time and the rise time. As shown in Figure 4.8 and described in a previous section, both the decay time and the rise time increased dramatically when Cl^- and Br^- were used compared to ClO_4^-. The short decay time with ClO_4^- reflects insufficient bipolar electrochemical coupling while the longer decay time with Cl^- and Br^- is likely due to formation of a nanobubble on the nanoparticle surface increasing the apparent volume. The increased nanoparticle/nanobubble size further slows down the translocation process. In both Cl^- and Br^--containing solution, the applied potential seems to strongly affect the translocation kinetics. For example, the translocation process was nearly three times faster at 2.5 V than at 2.0 V when Cl^- was used. This may suggest that a larger nanobubble is formed on the nanoparticle which further slows down the translocation process. Interestingly, we observed that the decay time in the Br^--containing solution is about 3 to 6 times shorter than in the Cl^--containing solution. Although we do not fully understand this phenomenon at this moment, we believe that it may be related to possible differences in

nanobubble nucleation and catalytic water oxidation on Ag surfaces partially covered by AgCl and AgBr.

4.4.4 *Control Experiments*

Besides voltage and halide ions, we have run several other experiments to study large current blockage events. First, we used gold nanoparticles for the same experiments. Unlike Ag, gold nanoparticles did not cause large blocking events with or without halide ions present in the bulk solution (Figure 4.12). We believe this is due to the large standard potential for gold oxidation (E^o = 1.83 V vs NHE). As another control, when the 100 mM HCl in the pipette was replaced by 100 mM KCl, no large blocking events greater than 10% of the open pore current was observed in 10 mM KCl (Figure 4.13a). Interestingly, there were a few events with current magnitude larger than 10% observed when 10 mM KBr was used in the bulk (Figure 4.13b). Although the exact reasons to this phenomenon is still under investigation, we cannot exclude the possibility of the reduction of water molecules ($2H_2O + 2e^- = H_2 + 2OH^-$) on the cathodic pole of the Ag nanoparticle (facing the inside of the pipette). Nevertheless, results Figure 4.13 suggest that protons are necessary to induce large current blockage events especially when Cl^- was used in the bulk.

4.4.5 *Simultaneous Optical Experiment and Electrical Recording*

To further verify that the large current blocking responses were indeed caused by nanoparticle translocation, we conducted simultaneous current recording and fluorescence imaging of the same quartz nanopipette pore in Ag nanoparticles and the results are presented in Figure 4.14. We used 40 nm Ag nanoparticles and 10 mM Br^- in the external solution and a 63 nm nanopipette containing 100 mM HCl as previously used. Figure 4.14c shows the position of the pipette orifice in bright field. We expect that AgBr and Ag_2O will be formed during particle translocation, which can be

probed by fluorescence microscopy because they are readily decomposed to form highly fluorescent small Ag clusters under laser illumination.[58,59]

Under a 2-V driving voltage, one can see individual current pulses including several small spikes and one large spike on this 30-s i-t trace (Figure 4.14a and Video S1). Fluorescence bursts could be observed at the pipette orifice, which correlated well in time with current spikes, as shown in Figure 4.14b. Careful investigation of the fluorescence and electrochemical recordings has revealed several interesting observations. First, we were unable to record noticeable fluorescent signal for many of the small current pulses. We believe this is due to ultrafast nanoparticle motion into the pipette when there was either no apparent bipolar coupling or the bipolar coupling was not sufficiently strong to induce bubble formation. A key difference between the optical and the current recordings was the recording speed. Unlike fast current recording, which had a sampling rate of 50,000 samples/s, fluorescence imaging was performed at ~20 frames/s in our current setting. Therefore, we anticipate that some of the fast translocation events would not be captured in optical recording. Second, the large current blockages usually appeared along with a much longer fluorescence burst. Moreover, there was sometimes a significant time delay between the fluorescence burst and the appearance of the large current pulse. For example, in Figure 4.14a and b, one can see that there was a large burst of fluorescence signal near the pore orifice, which lasted ~2.5 s prior to the detection of the large current spike marked as 3 in Figure 4.14a. It is reasonable to expect that the large current signal appeared only when the nanoparticle or the nanoparticle/nanobubble ensemble was in close vicinity to the pipette orifice. However, the fluorescence signal may be observed when the nanoparticle starts to be oxidized generating AgBr and Ag_2O in the bipolar coupling, which can happen from some finite distances. The time delay between the fluorescence burse and the current spike may reflect the time it took for the

nanoparticle to diffuse around prior to entering the nanopore orifice. During this period, more H_2 molecules may be generated on the surface of the nanoparticle to form a nanobubble, leading to the detection of a large current blockage.

4.4.6 *Biphasic Current Spike*

We have observed interesting biphasic current pulses when Br- was used in the bulk solution. These biphasic current spikes became more noticeable when voltage was increased to 2.5 V (Figure 4.15) from 2.0 V (Figure 4.7c). As shown in Figure 4.15, some of these current pulses were as large as 80% of the open pore current and showed an initial current increase, ~2-3 nA, on top of the 43 nm baseline current, followed by an abrupt decay to the minimum value. The current then slowly returned to the baseline. Biphasic current pulses have been reported in previous studies of nanoparticle translocation.[60] The slight current increase in a biphasic pulse is often believed to be caused by the nanoparticle-enhanced ion accumulation inside the nanopore. The slight current increase, in our conditions, is unlikely due to the effect of surface charge because the local environment near to the pipette orifice would likely be quite acidic considering the use of 100 mM H^+ in the pipette. It is unlikely that the H_2 nanobubble would bring a significant amount of charge and the surfaces of the Ag nanoparticles and the glass walls should be at or close to neutral due to protonation of the citrate ligands[61] and silanol groups at low pH. Instead, we believe that the slight current increase was caused by possible electrocatalytic water oxidation on the anodic pole of the Ag nanoparticle (facing the bulk solution) when part of the Ag nanoparticle was oxidized into AgBr and Ag_2O and water reduction on the opposite side of the particle. Ag_2O can catalyze electrocatalytic water oxidation.[50] The gaseous product molecules in these reactions should partially account for the formation of the nanobubble on the Ag. Meanwhile, the faradaic current signal due to water oxidation and reduction would also add onto the overall ionic current through

the nanopore causing an initial increase in the nanoparticle's translocation signal. This current increases as the nanoparticles gets closer and closer to the nanopore orifice due to an increased potential driving force causing H_2 molecules being generated at a faster rate. This continues until the local concentration of H_2 molecules reaches a critical value leading to the nucleation of a H_2 nanobubble. The nucleation and fast growth of the nanobubble leads to quick increase in the nanopore's ionic resistance leading to the large current decrease.

4.5 CONCLUSIONS

In summary, we have observed unusually large current blockage events associated with translocation of single Ag nanoparticles through a quartz pipette pore. Current blockages greater than 10 times that predicted based on particle size were observed in a uniquely designed bipolar electrochemical experiment, which facilitated the oxidation of Ag and reduction of protons on the two extremities of a same particle. In the presence of a high voltage across a pipette pore, an acidic environment inside the pipette pore, and halide ions outside the pore, a freely diffusing Ag nanoparticle in the vicinity of the nanopore orifice may act as a bipolar nanoelectrode oxidizing itself and water on one side of the particle and reducing the protons and water on the other. Reduction of protons and water generates molecular H_2 leading to the formation of a H_2 nanobubble which is responsible for the unusually large current blockage. This study represents the first evidence that transient bipolar electrochemistry can happen on small metal nanoparticles below 50 nm. The use of nanopore and resistive-pulse sensing may be extended to future nanoparticle studies in ultrafast electrochemistry, nanocatalyst screening, and gas nucleation on nanoparticles.

4.6 FIGURES

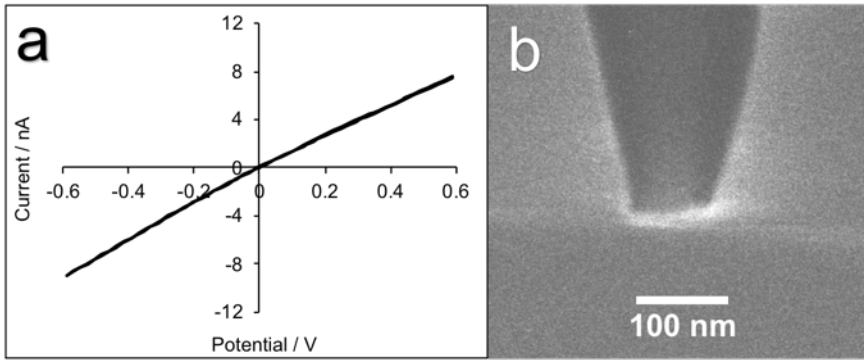

Figure 4.1. SEM image and i-V Curve of a nanopipette

(a) A representative i-V curve of a 66 nm diameter pipette nanopore in 100 mM KCl. The scan rate was 100 mV/s. The pipette pore diameter was calculated from the ionic resistance. (b) SEM image of a quartz nanopipette with a diameter ~60 nm. The potential in (a) was applied between two Ag/AgCl quasi-reference electrodes (QREs).

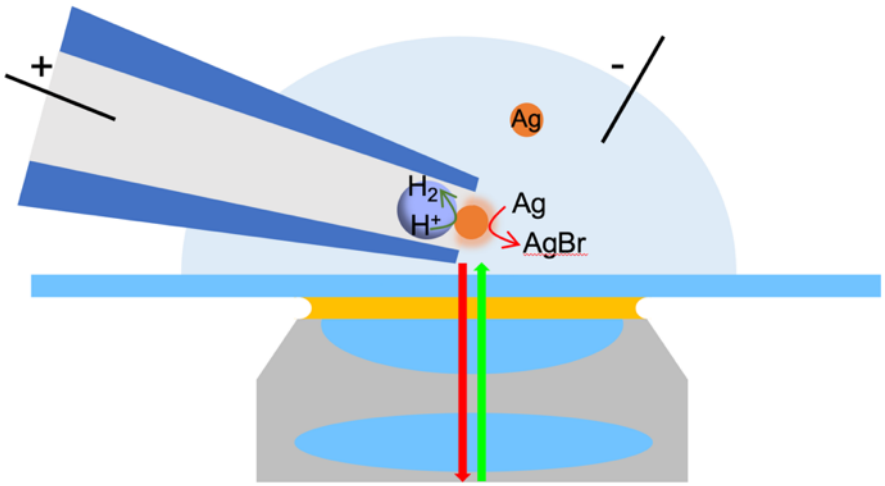

Figure 4.2. Schematic of the optical configuration

Schematic of the optical/electrochemical setup used to observe and detect translocation of single Ag nanoparticles through a nanopipette.

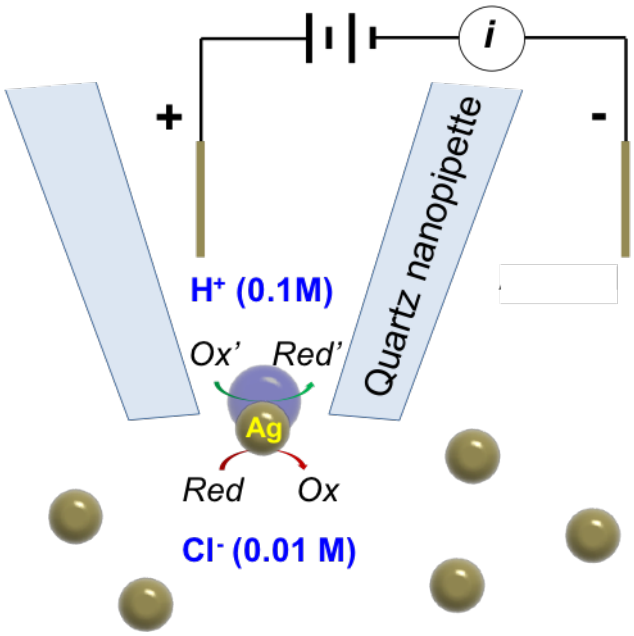

Figure 4.3. Schematic of electrochemical setup

Schematic illustration showing the nanopore-based approach to observe transient bipolar electrochemical response of single silver nanoparticle.

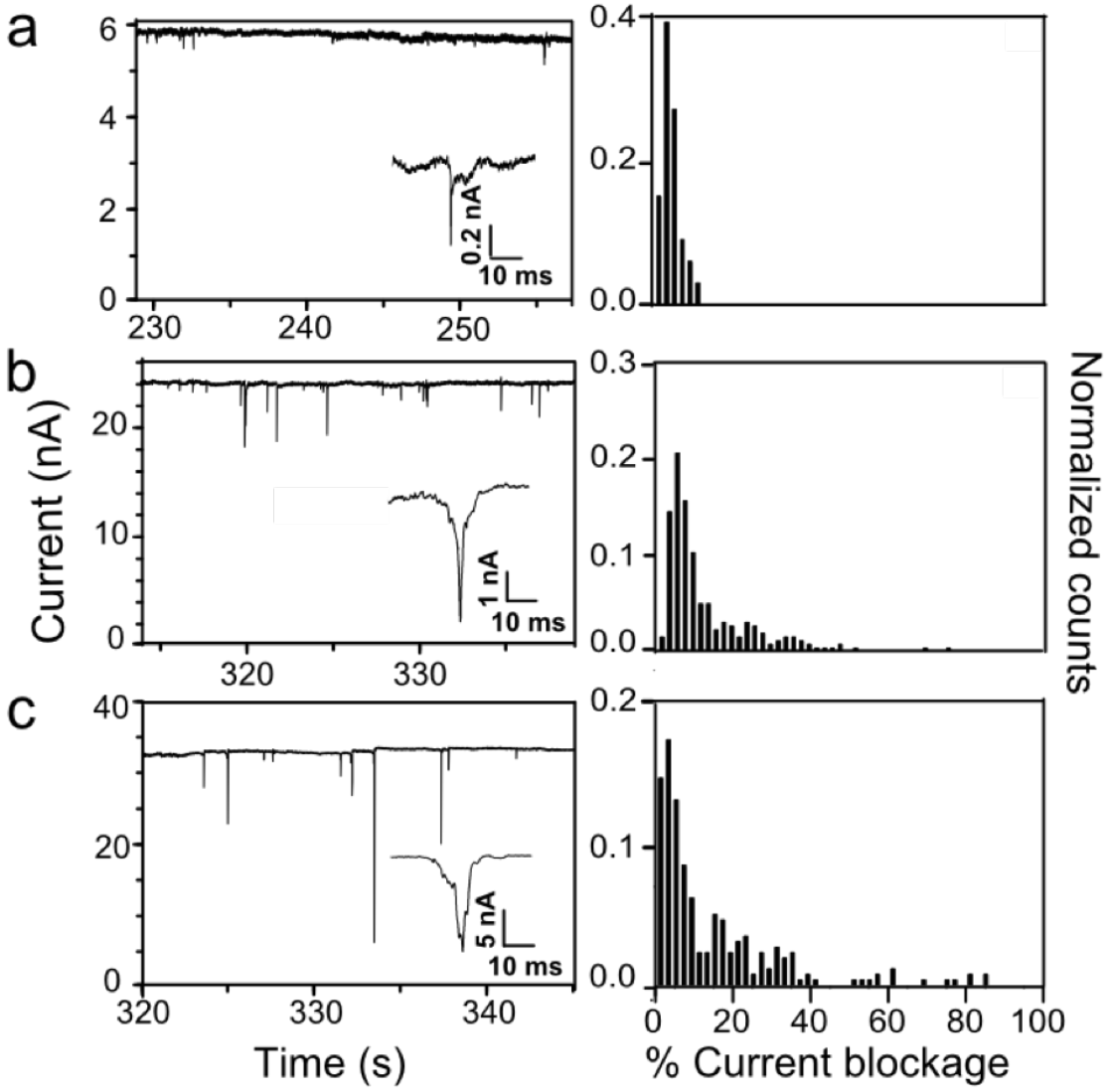

Figure 4.4. Potential-dependence of bipolar coupling

(Left panels) Representative current-time traces showing individual silver nanoparticles translocation events recorded at (a) 1 V, (b) 2 V and (c) 2.5 V. Insets are representative current spikes observed at each voltage bias. (Right panels) The corresponding histograms of %current blockage of the current spikes at (a) 1 V, (b) 2 V and (c) 2.5V. The counts were divided by total number of counts to get the normalized counts. Data were collected from ~20 nanopipettes with the similar geometries and pore sizes. The solution inside the pipette was 0.1 M HCl while the outside solution contains 10 mM KCl and 8 pM 40 nm Ag nanoparticles.

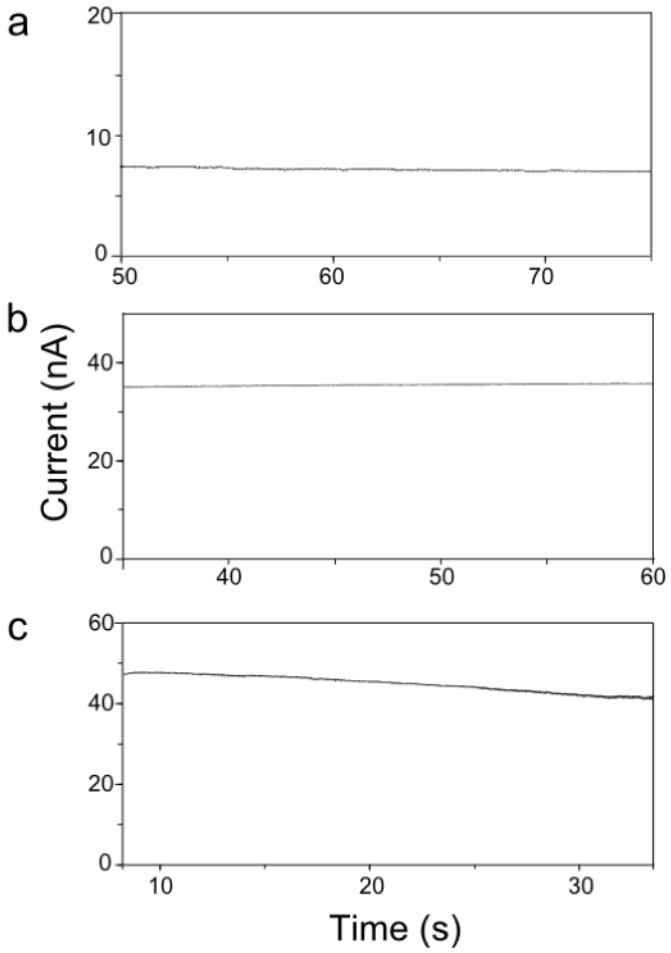

Figure 4.5. i-t traces recorded without nanoparticles at different potentials

Current-time traces recorded on a ~60 nm quartz nanopipette at (a) +1 V (b) +2 V and (c) +2.5 V applied potential with no Ag nanoparticles present in the solution. The solution inside the pipette was 0.1 M HCl while the outside solution contained 10 mM KCl.

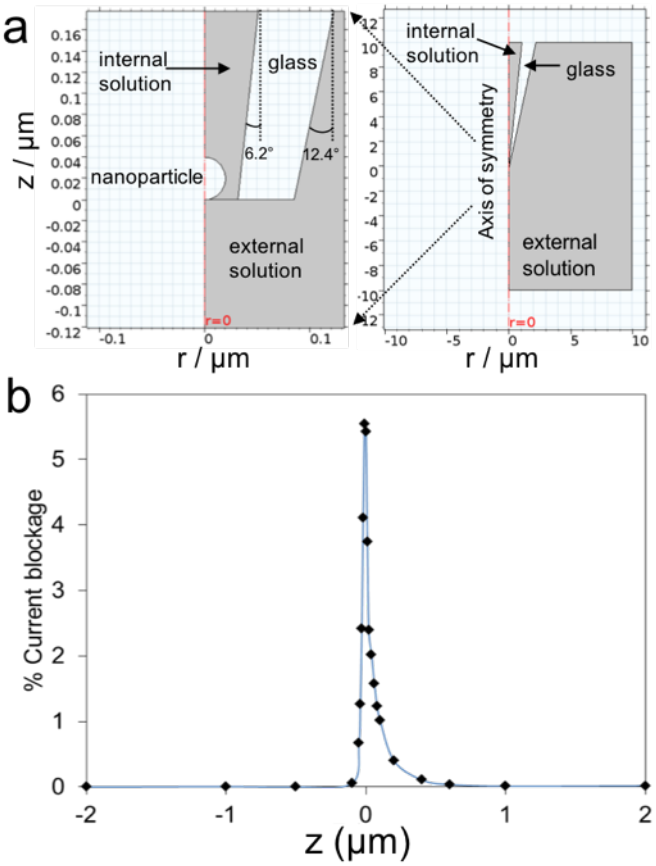

Figure 4.6. Numeric simulation of a nanoparticle in a nanopore

(a) The 2D axial-symmetry geometry of the nanopipette and nanoparticle used in the finite-element simulation. The right panel shows the entire geometry of the model while the zoom-in figure on the left shows the details at the nanopipette opening. (b) Simulated values of % current blockage as a function of the center z position of the 40 nm particle during its translocation through a 60-nm-diameter conical pore along the z axis. Values of $z < 0$ correspond to outside of the nanopipette, while values of $z > 0$ correspond to the inside. The geometry and boundary conditions for a simulation of the ionic current passing through a nanopore during a nanoparticle translocation are as following.

The geometry of the finite-element model is based on a two-dimensional (2D) axial-symmetry system (cylindrical coordinate). The pore orifice was centered at $r = 0$, $z = 0$. A 40-nm

diameter particle was placed near the pore orifice, as the zoomed-in picture shows (left part in Figure 4.6a). The radius of the nanopore was set to be 30 nm. The angle of the pipette was set according to the geometry from the SEM image in Figure 4.1b. To meet the semi-infinite condition of the experiment, the boundary of the bulk solution in the model was extended to a distance z = 10 μm away from the pore opening. The glass walls of the nanopipette and the nanoparticle surface were defined as an uncharged insulating boundary with no flux, to simplify the simulation. The electrolyte solution parameters were chosen to reflect 100 mM HCl as the internal solution, and 10 mM KCl as the external solution. A concentration boundary was set at the pore opening to distinguish the internal and external electrolyte solution. The ionic current was modeled by Nernst-Planck equation. The z position of the nanoparticle was varied from z = -2 μm to z = +2 μm to show that it moved in z direction along the centerline of the pipette, the corresponding ionic current in the presence of the nanoparticle was simulated and divided by baseline current to calculate %current blockage, as shown in Figure 4.6b. Applied voltage: +2 V inside pipette vs. outside.

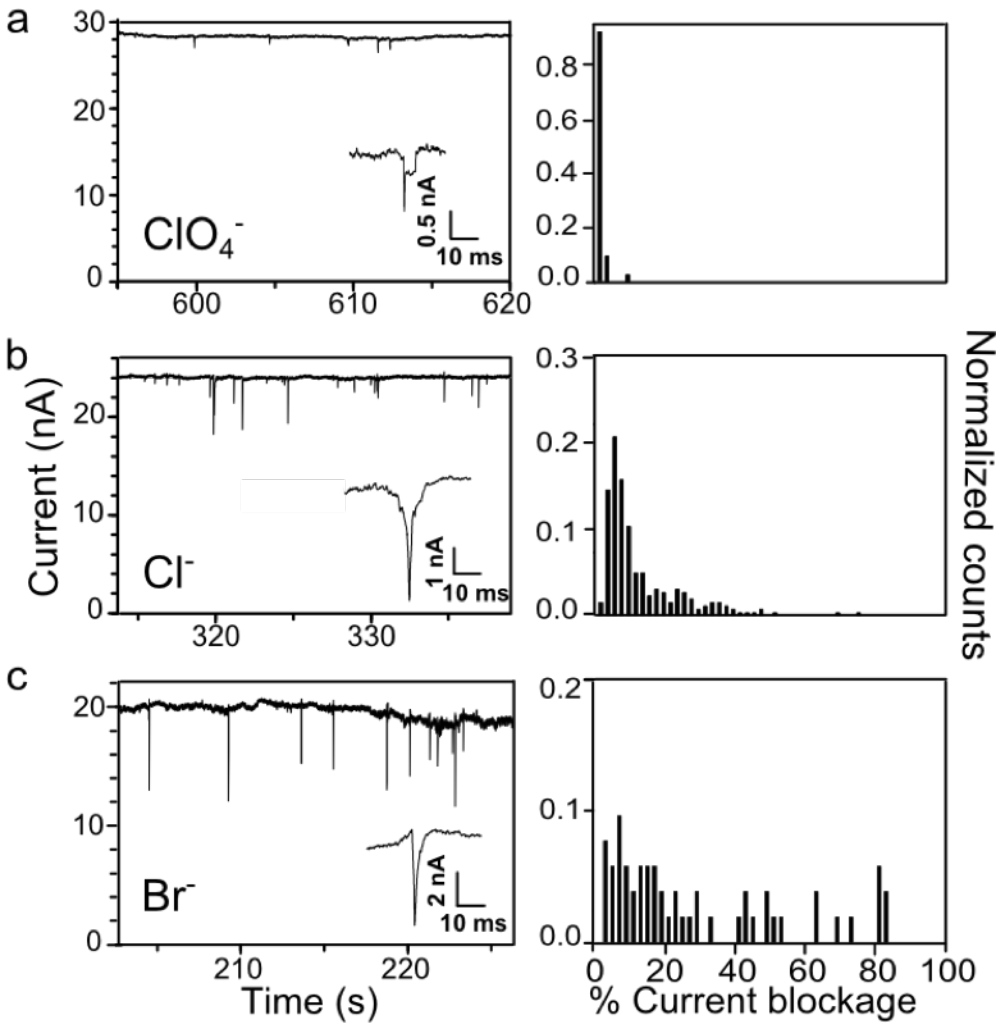

Figure 4.7. Anion-dependence of bipolar coupling.

(Left panels) Representative current-time traces showing individual silver nanoparticle translocation events recorded at 2 V from a nanopipette with (a) 100 mM $HClO_4$ inside and 10 mM $NaClO_4$ outside, (b) 100 mM HCl inside and 10 mM KCl outside, and (c) 100 mM HCl and 10 mM NaBr outside. All solutions outside also contained 8 pM 40 nm Ag nanoparticles. Insets are representative current spikes observed at each experimental condition. (Right panels) The corresponding histograms of %current blockage of the current spikes. The counts were divided by total number of counts to get the normalized counts.

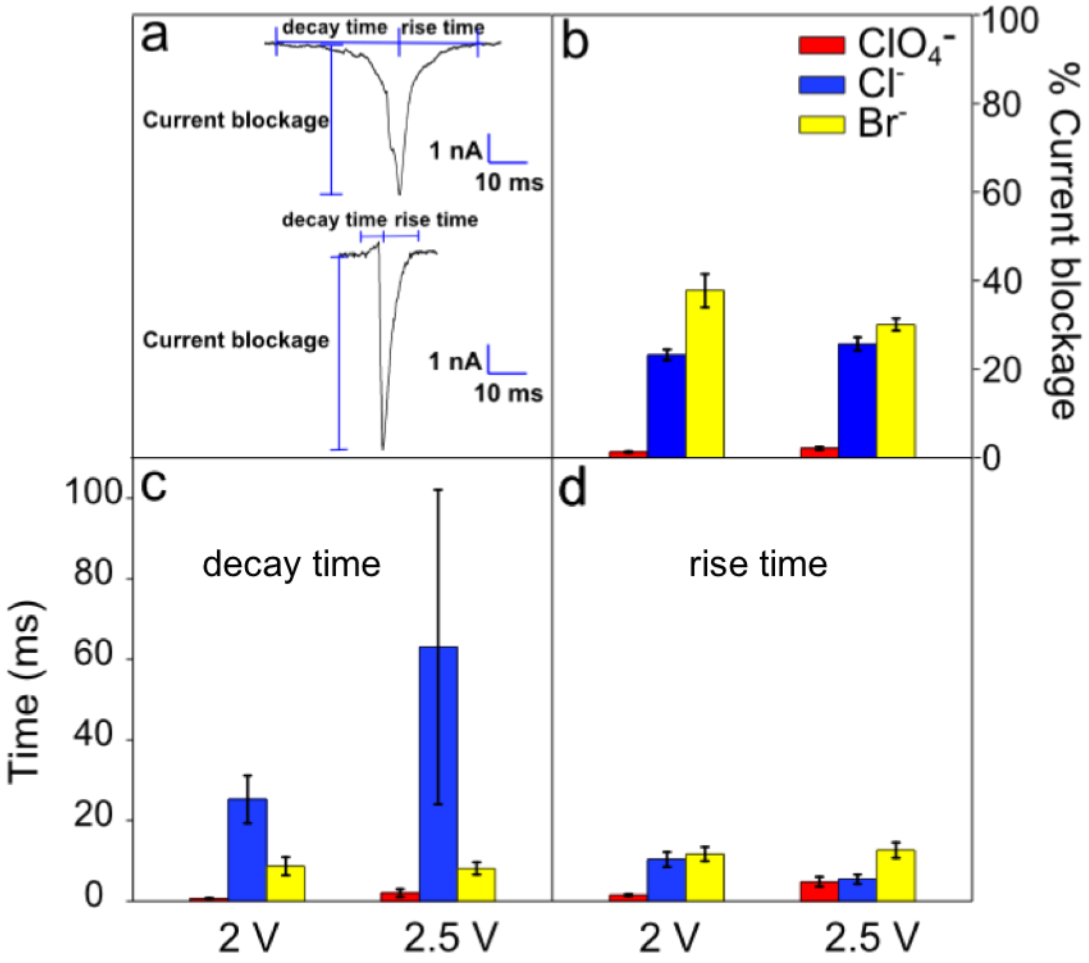

Figure 4.8. The effect of potential and anions on large current spikes

Characteristics of the current spikes observed at different experimental conditions. (a) Two representative large current spikes showing decay time, rise time, and peak recorded at 2 V with 10 mM Cl^- and 10 mM Br^- respectively in the bulk solution. (b) Average % current blockage with different anionic species present in the bulk solution at 2 V and 2.5 V potentials bias. (c) Average current decay times of the large current spikes observed with different anionic species at different potentials. (d) Average current rise times of the large current spikes observed with different anionic species at different potentials. Statistics were obtained from only the large (> 10% current blockage) current spikes. The error bars are the standard errors.

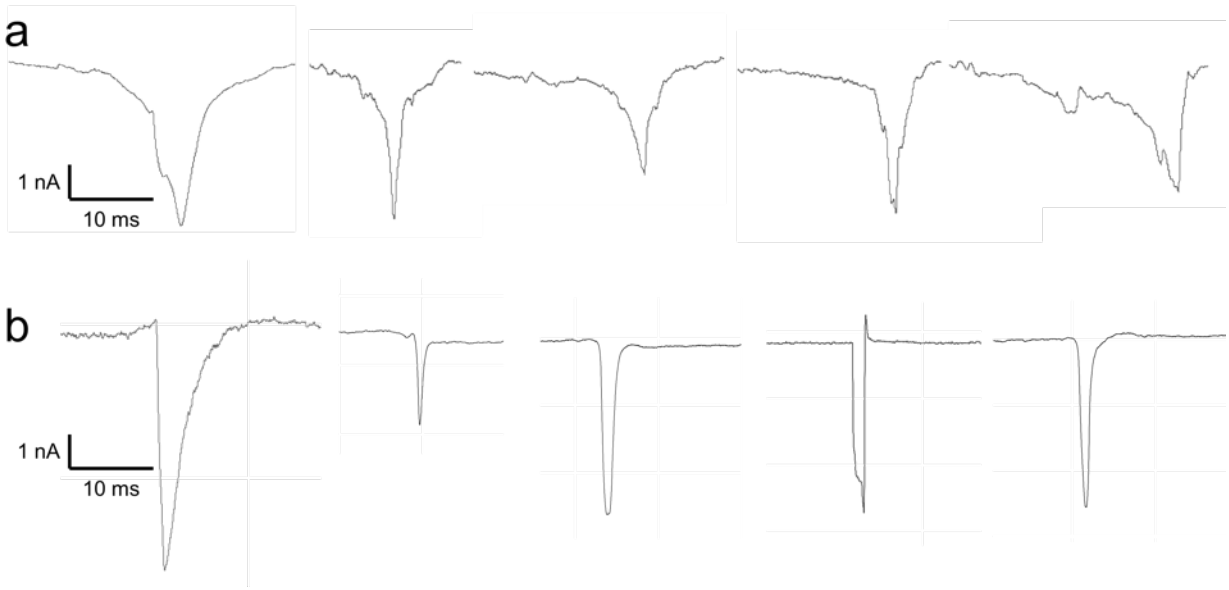

Figure 4.9. Representative large current spikes recorded at 2 V

Representative large current spikes recorded at +2 V on a 60-nm nanopipette containing 100 mM HCl in a solution of 10 mM KCl and 8 pM 40 nm Ag nanoparticles (a), and 10 mM NaBr and 8 pM 40 nm Ag nanoparticles (b).

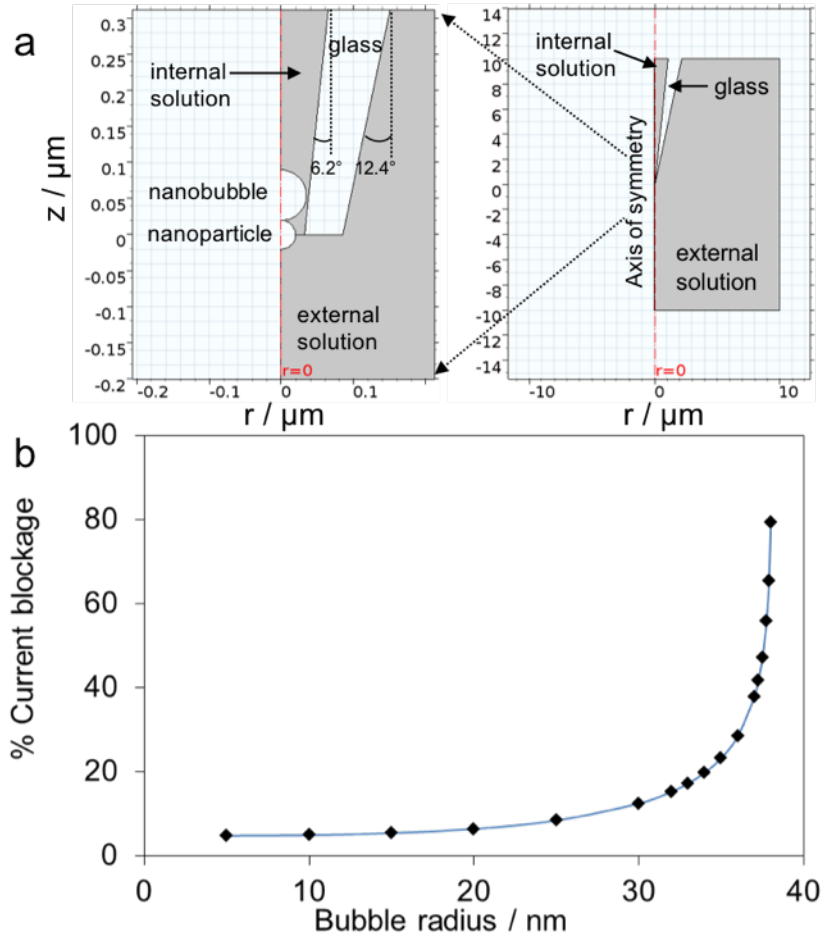

Figure 4.10. Numeric simulation of a nanoparticle and nanobubble in a nanopore (a) The 2D axial-symmetry geometry of the nanopipette, nanoparticle and nanobubble used to simulate the current blockage due to the generation of a nanobubble on the surface of a Ag nanoparticle. The right panel shows the entire geometry of the model while the zoom-in figure on the left shows the detail at the pipette opening. (b) Simulated values of % current blockage as a function of the radius of nanobubble attached to a 40-nm-diameter silver nanoparticle at the nanopore opening. The geometry and boundary conditions used for a simulation of the ionic current passing through a nanopore during a nanobubble formation on a nanoparticle are as following.

In the simulation, the geometry and boundary conditions were the same as in Figure 4.6, except that a nanobubble was placed on top of the nanoparticle. To simplify the simulation, we assume that the nanobubble was formed on the nanoparticle surface when the center of the particle was at r = 0, z = 0. The nanobubble surface was also defined as an uncharged insulating boundary with no flux. The radius of the bubble was set to vary from 5 nm to 38 nm. The corresponding ionic current in the presence of the nanoparticle and nanobubble was simulated and divided by baseline current to calculate % current blockage, as shown in Figure 4.10b.

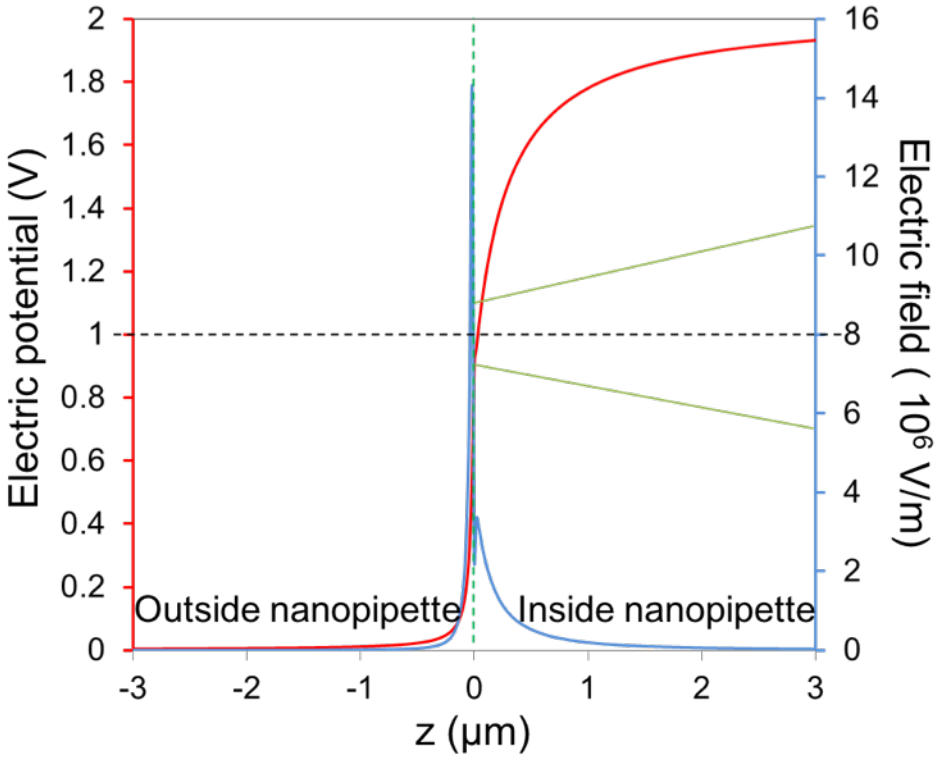

Figure 4.11. Simulated electric field and potential near a nanopore.

Simulated spatial distributions of the electric field (blue line) and electrostatic potential (red line) along the central pore axis in the absence of a nanoparticle. The yellow line segments indicate the position of the nanopipette. z = 0 corresponds to the location of the pore opening. Values of z < 0 correspond to outside of the nanopipette, while values of z > 0 correspond to the inside solution. Applied voltage: +2 V inside pipette vs. outside. In this simulation, the geometry and boundary conditions were the same as those shown in Figure 4.6, except that the nanoparticle was excluded from the orifice. The electric potential and electric field along the z axis (centerline of the pipette) was simulated and plotted as a function of z values, as shown in Figure 4.11.

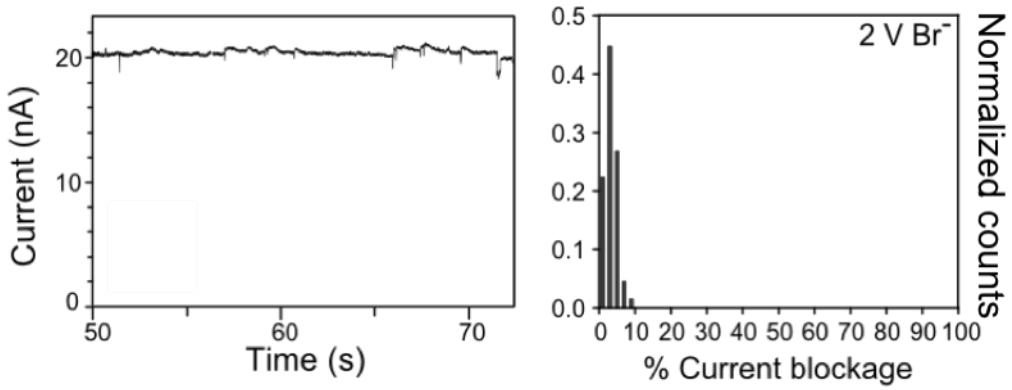

Figure 4.12. Representative i-t trace recorded with Au nanoparticles

(Left panel) A representative current-time trace showing individual translocation events of 42-nm Au nanoparticles recorded at +2 V. (Right panel) The corresponding histograms of %current blockage of the current spikes at +2 V. The counts were normalized to the total number of detected events. The solution inside the pipette was 0.1 M HCl while the outside solution contained 10 mM NaBr and 8 pM 40 nm Au nanoparticles.

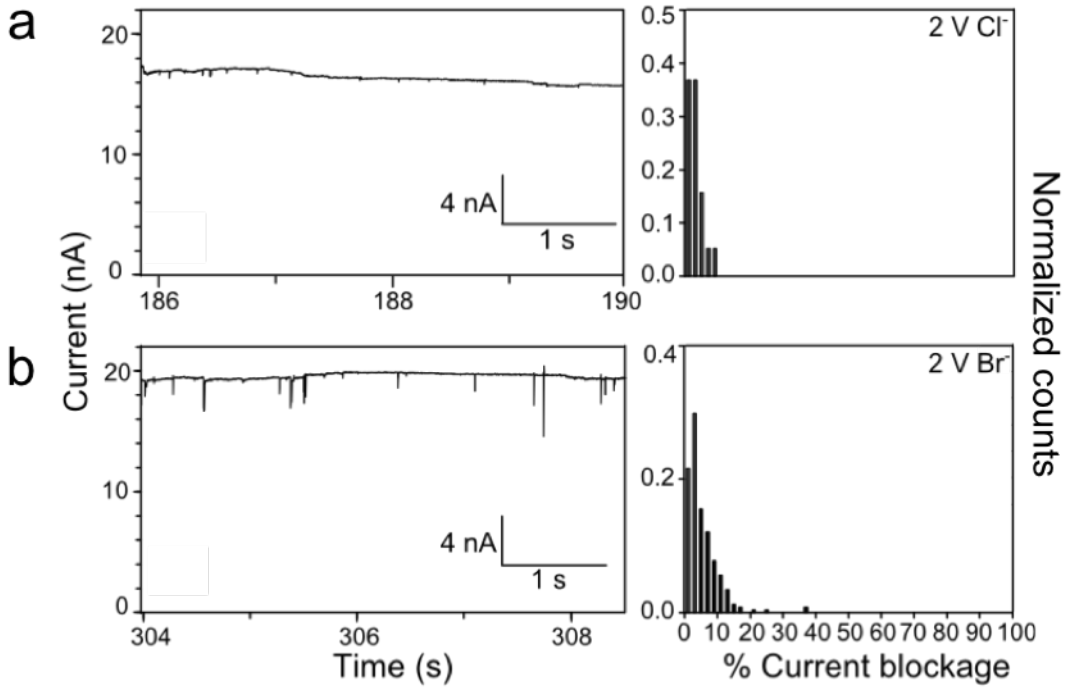

Figure 4.13. Representative i-t traces recorded with no H^+ in the pipette. (Left panels) Representative current-time traces showing individual translocation events of silver nanoparticles recorded at +2 V on a 60-nm nanopipette with (a) 100 mM KCl inside and 10 mM KCl outside, (b) 100 mM KCl inside and 10 mM NaBr outside. The outside solutions in both cases also contained 8 pM 40 nm Ag nanoparticles. (Right panels) The corresponding histograms of %current blockage of the current spikes. The counts were normalized to the total number of detected events.

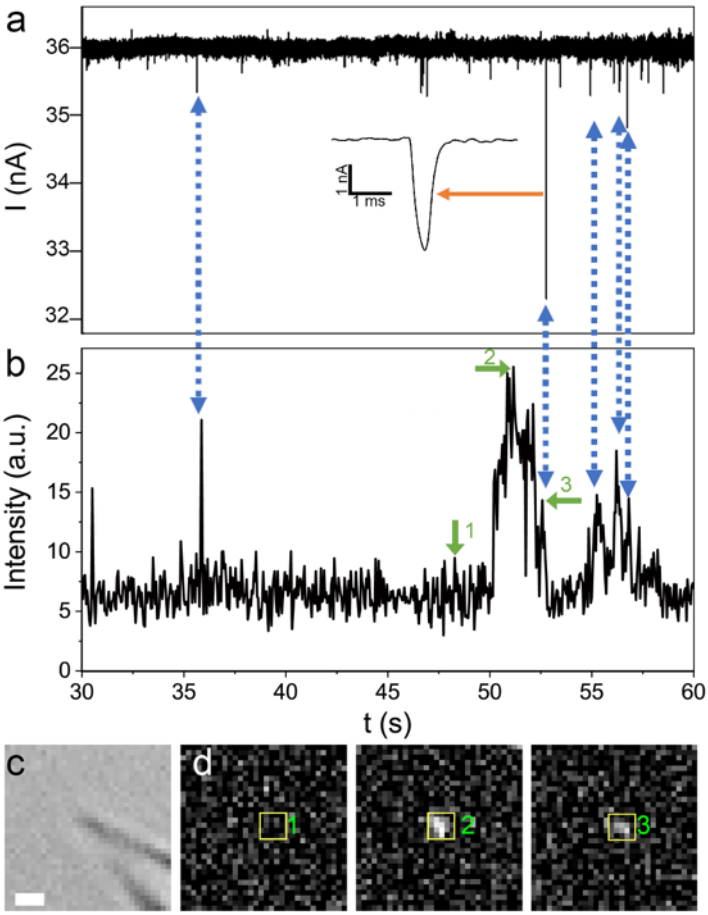

Figure 4.14. Simultaneous optical and electrochemical experiment.

Simultaneous current recording and fluorescence imaging of individual 40 nm Ag nanoparticle events. (a) A current-time trace showing individual current spikes at 2 V. The inset shows a zoom-in image of a large current spike within the trace. (b) The fluorescence intensity-time trace recorded simultaneously with the current-time trace shown in a. (c) Bright-field image of the tip of a nanopipette used for simultaneous electrical and fluorescence recording; (d) Fluorescence images of a Ag nanoparticle translocating through the nanopore at different time points as indicated by the green arrows in the fluorescence intensity-time trace in b. Scale bar represents 1 μm; Conditions: 100 mM HCl inside pipette, 10 mM NaBr and 0.8 pM 40nm Ag nanoparticles outside pipette.

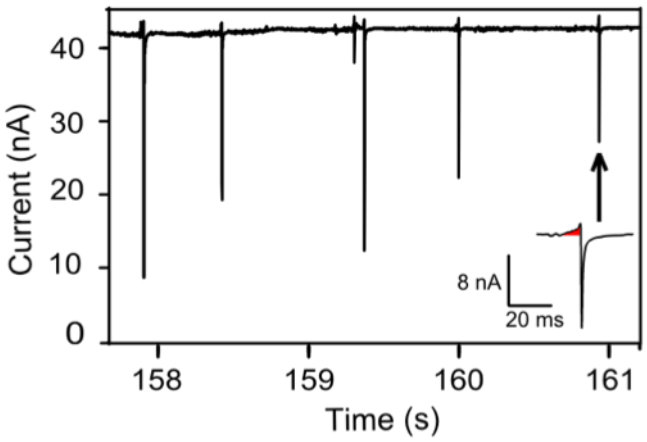

Figure 4.15. Representative current-time trace showing biphasic current spikes. A current-time trace showing individual biphasic spikes recorded at 2.5 V with 100 mM HCl inside and 10 mM NaBr and 8 pM 40 nm Ag nanoparticles outside. The inset is a zoom-in image of a representative biphasic spike from the trace indicated by the arrow.

4.7 REFERENCES

(1) Fan, Y.; Anderson, T. J.; Zhang, B. Single-Molecule Electrochemistry: From Redox Cycling to Single Redox Events. *Curr. Opin. Electrochem.* **2018**, *7*, 81-86.

(2) Robinson, D. A.; Edwards, M. A.; Ren, H.; White, H. S. Effects of Instrumental Filters on Electrochemical Measurement of Single-Nanoparticle Collision Dynamics. *ChemElectroChem.* **2018**, *5,*1-10.

(3) Fan, F. R.; Bard, A. J. Electrochemical Detection of Single Molecules. *Science* **1995**, *267*, 871-874.

(4) Lemay, S. G.; Kang, S.; Mathwig, K.; Singh, P. S. Single-Molecule Electrochemistry: Present Status and Outlook. *Acc. Chem. Res.* **2013***, 46,* 369-377.

(5) Mirkin Sun, P.; Mirkin, M. V. Electrochemistry of Individual Molecules in Zeptoliter Volume. *J. Am. Chem. Soc.* **2008**, *130*, 8241-8250.

(6) Byers, J. C.; Paulose Nadappuram, B.; Perry, D.; McKelvey, K.; Colburn, A. W.; Unwin, P. R. Single Molecule Electrochemical Detection in Aqueous Solutions and Ionic Liquids. *Anal. Chem.* **2015**, *87*, 10450-10456.

(7) Shi, W.; Friedman, A. K.; Baker, L. A. Nanopore Sensing. *Anal. Chem.* **2017**, *89*, 157-188.

(8) Heins, E. A.; Siwy, Z. S.; Baker, L. A.; Martin, C. R. Detecting Single Porphyrin Molecules in a Conically Shaped Synthetic Nanopore. *Nano Lett.* **2005**, *5*, 1824-1829.

(9) Bayley, H.; Martin, C. R. Resistive-Pulse Sensing-From Microbes to Molecules. *Chem. Rev.* **2000**, *100*, 2575-2594.

(10) Luo, L.; German, S. R.; Lan, W.-J.; Holden, D. A.; Mega, T. L.; White, H. S. Resistive-Pulse Analysis of Nanoparticles. *Annu. Rev. Anal. Chem.* **2014**, *7*, 513-535.

(11) Lan, W. J.; Holden, D. A.; Zhang, B.; White, H. S. Nanoparticle Transport in Conical-Shaped Nanopores. *Anal. Chem.* **2011**, *83*, 3840-3847.

(12) Ito, T.; Henriquez, R. R.; Crooks, R. M. A Carbon Nanotube-Based Coulter Nanoparticle Counter. *Acc. Chem. Res.* **2004**, *37*, 937-945.

(13) Fu, K.; Bohn, P. W. Nanopore Electrochemistry: A Nexus for Molecular Control of Electron Transfer Reactions. *ACS Cent. Sci.* **2018**, *4*, 20-29.

(14) Hill, C. M.; Pan, S. A Dark-Field Scattering Spectroelectrochemical Technique for Tracking the Electrodeposition of Single Silver Nanoparticles. *J. Am. Chem. Soc*. **2013**, *135*, 17250-17253.

(15) Hill, C. M.; Bennett, R.; Zhou, C.; Street, S.; Zheng, J.; Pan, S. Single Ag Nanoparticle Spectroelectrochemistry via Dark-Field Scattering and Fluorescence Microscopies. *J. Phys. Chem. C.* **2015**, *119*, 6760-6768.

(16) Brasiliense, V.; Patel, A.N.; Martinez-Marrades, A.; Shi, J.; Chen, Y.; Combellas, C.; Tessier, G.; Kanoufi, F. Correlated Electrochemical and Optical Detection Reveals the Chemical Reactivity of Individual Silver Nanoparticles. *J. Am. Chem. Soc.* **2016**, *138*, 3478-3483.

(17) Lu, J.; Fan, Y.; Howard, M. D.; Vaughan, J. C.; Zhang, B. Single-Molecule Electrochemistry on a Porous Silica-Coated Electrode. *J. Am. Chem. Soc.* **2017**, *139*, 2964-2971.

(18) Palacios, R. E.; Fan, F. R. F.; Bard, A. J.; Barbara, P. F. Single-Molecule Spectroelectrochemistry (SMS-EC). *J. Am. Chem. Soc.* **2006**, *128*, 9028-9029.

(19) Lei, C.; Hu, D.; Ackerman, E. J. Single-molecule Fluorescence Spectroelectrochemistry of Cresyl Violet. *Chem. Commun.* **2008**, *0*, 5490-5492.

(20) Xu, W.; Shen, H.; Kim, Y.; J.; Zhou, X.; Liu, G.; Park, J.; Chen P. Single-Molecule Electrocatalysis by Single-Walled Carbon Nanotubes. *Nano Lett.* **2009**, *9*, 3968-3973.

(21) Zhao, J.; Zaino, L. P.; Bohn, P. W. Potential-Dependent Single Molecule Blinking Dynamics for Flavin Adenine Dinucleotide Covalently Immobilized in Zero-Mode Waveguide Array of Working Electrodes. *Faraday Discuss.* **2013**, *164*, 57-69.

(22) Shan, X.; Diez-Perez, I.; Wang, L.; Wiktor, P.; Gu, Y.; Zhang, L.; Wang, W.; Lu, J.; Wang, S.; Gong, Q.; Li, J.; Tao, N. Imaging the Electrocatalytic Activity of Single Nanoparticles. *Nat. Nanotechnol.* **2012**, *7*, 668-672.

(23) Fang, Y.; Wang, W.; Wo, X.; Luo, Y.; Yin, S.; Wang, Y.; Shan, X.; Tao, N. Plasmonic Imaging of Electrochemical Oxidation of Single Nanoparticles. *J. Am. Chem. Soc.* **2014**, *136*, 12584-12587.

(24) Zong, C.; Chen, C.; Zhang, M.; Wu, D.; Ren, B. Transient Electrochemical Surface-Enhanced Raman Spectroscopy: A Millisecond Time-Resolved Study of an Electrochemical Redox Process. *J. Am. Chem. Soc.* **2015**, *137*, 11768-11774.

(25) Kwon, S. J.; Zhou, H.; Fan, F. R. F.; Vorobyev, V.; Zhang, B.; Bard, A. J. Stochastic Electrochemistry with Electrocatalytic Nanoparticles at Inert Ultramicroelectrodes--Theory and Experiments. *Phys. Chem. Chem. Phys.* **2011**, *13*, 5394-5402.

(26) Cheng, W.; Compton, R. G. Electrochemical Detection of Nanoparticles by 'Nano-impact' Methods. *TrAC Trends Anal. Chem.* **2014**, *58*, 79-89.

(27) Quinn, M.; van't Hof, P. G.; Lemay, S. G. Time-Resolved Electrochemical Detection of Discrete Adsorption Events. *J. Am. Chem. Soc.*, **2004**, *126*, 8360-836.

(28) Kim, B.-K.; Boika, A.; Kim, J.; Dick, J. E. Bard, A. J. Characterizing Emulsions by Observation of Single Droplet Collisions-Attoliter Electrochemical Reactors. *J. Am. Chem. Soc.* **2014**, *136*, 4849-4852.

(29) Xiao, X.; Bard, A. J. Observing Single Nanoparticle Collisions at an Ultramicroelectrode by Electrocatalytic Amplification. *J. Am. Chem. Soc.* **2007**, *129*, 9610-9612.

(30) Xiao, X.; Fan, F. R. F.; Zhou, J.; Bard, A. J. Current Transients in Single Nanoparticle Collision Events. *J. Am. Chem. Soc.* **2008**, *130*, 16669-16677.

(31) Oja, S. M.; Robinson, D. A.; Vitti, N. J. V.; Edward, M. A.; Liu, Y.; White, H. S.; Zhang, B. Observation of Multipeak Collision Behavior during the Electro-Oxidation of Single Ag Nanoparticles. *J. Am. Chem. Soc.* **2017**, *139*, 708-718.

(32) Hao, R.; Fan. Y.; Zhang, B. Imaging Dynamic Collision and Oxidation of Single Silver Nanoparticles at the Electrode/Solution Interface. *J. Am. Chem. Soc.* **2017**, *139*, 12274-12282.

(33) Fu, K.; Han, D.; Crouch, G. M.; Kwon, S. R.; Bohn, P. W. Voltage-Gated Nanoparticle Transport and Collisions in Attoliter-Volume Nanopore Electrode Arrays. *Small* **2018**, *14*, 1703248.

(34) Fosdick, S. E.; Knust, K. N.; Scida, K.; Crooks, R. M. Bipolar Electrochemistry. *Angew. Chem. Int. Ed.* **2013**, *52*, 10438-10456.

(35) Dumitrescu, I.; Anand, R. K.; Fosdick, S. E.; Crooks, R. M. Pressure-Driven Bipolar Electrochemistry. *J. Am. Chem. Soc.* **2011**, *133*, 4687-4689.

(36) Knust, K. N.; Sheridan, E.; Anand, R. K.; Crooks, R. M. Dual-Channel Bipolar Electrode Focusing: Simultaneous Separation and Enrichment of both Anions and Cations. *Lab Chip* **2012**, *12*, 4107-4114.

(37) Zhang, X.; Chen, C.; Li, J.; Zhang, L.; Wang, E. New Insight into a Microfluidic-Based Bipolar System for an Electrochemiluminescence Sensing Platform. *Anal. Chem.* **2013**, *85*, 5335-5339.

(38) Fosdick, S.E.; Crooks. R. M. Bipolar Electrodes for Rapid Screening of Electrocatalysts. *J. Am. Chem. Soc.* **2012**, *134*, 863-866.

(39) Guerrette, J. P.; Percival S. J.; Zhang, B. Fluorescence Coupling for Direct Imaging of Electrocatalytic Heterogeneity. *J. Am. Chem. Soc.* **2013**, *135*, 855-861.

(40) Oja, S. M.; Guerrette, J. P.; David, M. R.; Zhang, B. Fluorescence-Enabled Electrochemical Microscopy with Dihydroresorufin as a Fluorogenic Indicator. *Anal. Chem.* **2014**, *12*, 6040-6048.

(41) Oja, S.M.; Zhang, B. Imaging Transient Formation of Diffusion Layers with Fluorescence-Enabled Electrochemical Microscopy. *Anal. Chem*. **2014**, *24*, 12299-12307.

(42) Xu, W.; Fu, K.; Bohn, P. W. Electrochromic Sensor for Multiplex Detection of Metabolites Enabled by Closed Bipolar Electrode Coupling. *ACS Sens*. **2017**, *2*, 1020-1026.

(43) Paxton, W. F.; Kistler, K. C.; Olmeda, C. C.; Sen, A.; St. Angelo, S. K.; Cao, Y.; Mallouk, T. E.; Lammert, P. E.; Crespi, V. H. Catalytic Nanomotors: Autonomous Movement of Striped Nanorods. *J. Am. Chem. Soc.* **2004**, *126*, 13424-13431.

(44) Demirok, U. K.; Laocharoensuk R.; Manesh, K. M.; Wang, J. Ultrafast Catalytic Alloy Nanomotors. *Angew. Chem. Int. Ed.* **2008**, *47*, 9349-9351.

(45) Loget, G.; Zigah, D.; Bouffier, L.; Sojic, N.; Kuhn, A. Bipolar Electrochemistry: From Materials Science to Motion and Beyond. *Acc. Chem. Res.* **2013**, *46*, 2513-2523.

(46) Loget, G.; Roche, J.; Gianessi, E.; Bouffier, L.; Kuhn, A. Indirect Bipolar Electrodeposition. *J. Am. Chem. Soc.* **2012**, *134*, 20033-20036.

(47) Fattah, Z.; Garrigue, P.; Lapeyre, V.; Kuhn, A.; Bouffier, L. Controlled Orientation of Asymmetric Copper Deposits on Carbon Microobjects by Bipolar Electrochemistry. *J. Phys. Chem. C.* **2012**, *116*, 22021-22027.

(48) Fattah, Z.; Garrigue, P.; Goudeau, B.; Lapeyre, V.; Kuhn, A.; Bouffier, L. Capillary Electrophoresis as a Production Tool for Asymmetric Microhybrids. *Electrophoresis* **2013**, *34*, 1985-1990.

(49) Stockmann, T. J.; Angelé, L.; Brasiliense, V.; Combellas, C.; Kanoufi, F. Platinum Nanoparticle Impacts at a Liquid|Liquid Interface. *Angew. Chem. Int. Ed.* **2017**, *56*, 13493-13497.

(50) Zhang, F.; Defnet, P. A.; Fan, Y.; Hao, R.; Zhang, B. Transient Electrocatalytic Water Oxidation in Single-Nanoparticle Collision. *J. Phys. Chem. C.* **2018**, *11*, 6447-6455.

(51) Zhang, B.; Galusha, J.; Shiozawa, P. G.; Wang, G.; Bergren, A. J.; Jones, R. M.; White, R. J.; Ervin, E. N.; Cauley, C. C.; White, H. S. Bench-Top Method for Fabricating Glass-Sealed Nanodisk Electrodes, Glass Nanopore Electrodes, and Glass Nanopore Membranes of Controlled Size. *Anal. Chem.* **2007**, *79*, 4778-4787.

(52) Guerrette, J. P.; Zhang, B. Scan-Rate-Dependent Current Rectification of Cone-Shaped Silica Nanopores in Quartz Nanopipettes *J. Am. Chem. Soc.* **2010**, *132*, 17088-17091.

(53) Cox, J. T.; Guerrette, J. P.; Zhang, B. Steady-State Voltammetry of a Microelectrode in a Closed Bipolar Cell. *Anal. Chem.* **2012**, *84,* 8797-8804.

(54) Stanley-Wood, N. G.; Lines, R. W. *Particle Size Analysis*. Royal Society of Chemistry: Cambridge, U. K. **1992**, 351-383.

(55) Ito, T.; Sun, L.; Crooks, R. M. Simultaneous Determination of the Size and Surface Charge of Individual Nanoparticles Using a Carbon Nanotube-Based Coulter Counter. *Anal. Chem.* **2003**, *75*, 2399-2406.

(56) Bard, A. J.; Faulkner, L. R. *Electrochemical Methods*, 2nd ed.; John Wiley & Sons: New York, 2001.

(57) Hao, R.; Fan, Y.; Howard, M. D.; Vaughan, J. C.; Zhang, B. Imaging Nanobubble Nucleation and Hydrogen Spillover during Electrocatalytic Water Splitting. *Proc. Natl. Acad. Sci. U.S.A.* **2018**, *115*, 5878-5883.

(58) Peyser, L. A.; Vinson, A. E.; Bartko, A. P.; Dickson, R. M. Photoactivated Fluorescence from Individual Silver Nanoclusters. *Science* **2001**, *291*, 103-106.

(59) Peyser, L. A.; Lee, T.-H.; Dickson, R. M. Mechanism of Ag_n Nanocluster Photoproduction from Silver Oxide Films. *J. Phys. Chem. B.* **2002**, *106*, 7725-7728.

(60) Lan, W.; Kubeil, C.; Xiong, J.; Bund, A.; White, H. S. Effect of Surface Charge on the Resistive Pulse Waveshape during Particle Translocation through Glass Nanopores. *J. Phys. Chem. C.* **2014**, *118*, 2726-2734.

(61) Masitas, R.A.; Allen, S.; Zamborini, F.P. Size-Dependent Electrophoretic Deposition of Catalytic Gold Nanoparticles. *J. Am. Chem. Soc.* **2016**, *138*, 15295-15298.

Chapter 5. SINGLE VESICLE DETECTION WITH A GLASS MICROBULB

5.1 INTRODUCTION

Vesicles play a variety of functions in metabolism,[1] intracellular and intercellular transport,[2] and neurotransmission[3,4]. Vesicles in model cells, such as pheochromocytoma (PC12) cells, are around 100-300 nm in diameter, and could contain millions of dopamine molecules. In order to better understand the biological functions of vesicles, it is necessary to characterize the size of vesicles. Current analytical methods include dynamic light scattering (DLS),[5] nanoparticle tracking analysis (NTA),[6] cryo-electron microscopy (cryo-EM),[7] atomic force microscopy (AFM).[8] For electron microscopy, the extensive and multistep sample preparations could change the morphology of the vesicles. Moreover, the electron beam may also damage biological samples. It is beneficial to develop a noninvasive method to characterize vesicles so that it can be integrated with other analytical methods to analyze other information such as the content or neurotransmitter concentration.[9] For DLS and NTA methods, the vesicle population are not changed by the detection mechanism, however, relatively large number of vesicles are needed to yield statistical results.

Electrochemical methods have been applied to neurochemistry since 1970s. A variety of electrochemical techniques have been used to probe neurotransmitter release in living tissues, such as amperometry, cyclic voltammetry, and potential pulse methods.[10] Our group has been using polarized carbon fiber or modified ultramicroelectrodes to oxidize catecholamine released from cell exocytosis.[11,12] We are also developing new tools for studying single isolated vesicles. Compared to other methods, electrochemical methods are label-free, and can give chemical

information with high temporal resolution. For example, the temporal resolution for amperometry detection and fast scan cyclic voltammetry is microseconds and milliseconds, respectively.

A nanopore is a pore of nanometer size inside an ultrathin membrane. Ions flow across the nanopore under a voltage bias across the membrane. When a particle translocates through the nanopore and blocks a certain number of ions, the ionic resistance of the nanopore increases and results in a resistive current pulse in the current-time recording. [13-17] Nanopore sensing has been widely used in the detection of nanoparticles, DNA, protein, virus.[17] In the recent years, the translocation of soft particles are also studied with nanopore sensing technique. The dynamic deformation of soft particles increases the complexity of the translocation process but also reveals a lot of interesting information of the soft particles. Here we developed glass nanopores and detected the translocation of artificial ~80 nm and ~200 nm liposomes through the nanopore. Then we extend the nanopore sensing technique to the detection of single vesicles isolated from PC12 cells. This method is high-throughput, noninvasive, and it can analyze vesicles isolated from cellular samples directly. A size distribution of vesicles could be obtained from the resistive current pulses corresponding to every single vesicle, and the average diameter estimated from the current blockage was 221 nm, in good agreement with the known PC12 vesicles.[18]

5.2 Experimental Section

5.2.1 *Chemicals and Materials*

All chemicals and materials were used as received from the manufacturers. Sodium chloride (NaCl, J. T. Baker), potassium chloride (KCl, J. T. Baker), HEPES (Fisher BioReagents), sodium hydroxide pellets (NaOH, 98.5%, J.T. Baker), 1,2-dioleoyl-sn-glycero-3-phosphocholine (DOPC) (Avanti Polar Lipids), 2-allylphenol (Sigma Aldrich), citric acid monohydrate (Fisher Scientific), poly (acrylic acid) (Sigma Aldrich), sodium citrate dehydrate (Fisher Scientific), silver

wire (99.9%, 0.127 mm diameter, Alfa Aesar), single barrel borosilicate capillary with filament (0.69 mm I.D./1.2 mm O.D.). Running buffer contains 10 mM HEPES and 142 mM NaCl. The pH was adjusted to ~7.2 with 3 M NaOH. Homogenizing buffer contains 0.3 M sucrose, 1 mM EDTA, 1 mM $MgSO_4$, 10 mM HEPES and 10 mM KCl, the solution pH was adjusted to ~7.2 with 3 M NaOH. All aqueous solutions were prepared using deionized water (>18 MΩ cm) obtained through a Barnstead Nanopure water purification system.

5.2.2 *Fabrication of Borosilicate Glass Nanopipette*

Borosilicate nanopipettes were prepared with a P-97 puller (Sutter Instrument) by pulling a 0.69 mm I.D./1.2 mm O.D. capillary. The pulling program was "heat = 339, pull = 0, velocity = 60, time = 250".

5.2.3 *Scanning Electron Microscope (SEM) imaging*

SEM imaging (Figure 5.3b) was performed on an FEI XL830 Dual Beam system operating at a 5 kV accelerating potential. The sample was coated with a thin layer of carbon by sputtering.

5.2.4 *80 nm and 200 nm Liposome Preparation*

We applied a method described in work by Ewing's group to prepare 80 nm or 200 nm liposome.[19] First, a 0.3 mL lipid mixture (25 mg/mL lipid) was made by mixing DOPC, DOPE, and cholesterol in mass ratio 2:1:1. The lipid mixture was purged with argon to evaporate traces of organic solvent and form a thin lipid film in the vial. The lipid film was rehydrated with 150 mM dopamine in 1.5 mL running buffer at room temperature under argon for 30 min. Then the rehydrated mixture was placed in liquid nitrogen and a warm water bath alternately. This freeze-thaw cycle was repeated for five times. The liposomal suspension was then extruded 21 times with Avanti Mini-Extruder (Avanti Polar Lipids, Inc., USA) over 80 nm polycarbonate membranes

(Whatman, USA) at room temperature. To get liposomes of different sizes, 200 nm pore size polycarbonate membranes were used. The liposomal suspension was centrifuged at 15000 g at +4 ℃ for 45 min to exclude dopamine outside the liposomes. The suspension was discarded while the liposome pellet was redispersed in 1 mM running buffer.

5.2.5 *Vesicle Preparation*

Vesicle isolation from cultured cells involves breaking the cells, high-speed centrifugation, and re-suspension of vesicles. The isolation of vesicles from PC12 cells was previously described with modifications.[20] Confluent cells from 24 25 cm^2 flasks were forcefully detached from flasks, and the suspensions were combined into one fraction. This fraction was then centrifuged at 1500 rpm for 12 min under room temperature. The supernatant containing growth media was discarded. The cells pellets were then homogenized in 4 mM homogenizing buffer at 4 ° C until the cell membranes were broken, as observed under the microscope. The homogenate was centrifuged at 1000g for 20 min at 4 °C to remove nonlysed cells and cell debris. The supernatant was subsequently centrifuged at 15000g for 45 min at 4 °C to pellet PC12 vesicles. The pellet was re-suspended in 3 mL homogenizing or running buffer and used as vesicle stock solution.

5.2.6 *Electrochemical Detection*

All the electrochemical experiments were performed by using a Axopatch 200B integrating patch-clamp amplifier (Molecular Devices). Amperometry data were recorded on a Dell PC through a Digidata 1440 digitizer (Molecular Devices). The Axopatch was used in V-clamp mode with whole cell $\beta = 1$ and the low-pass filter set to 1 kHz. Amperometric traces were recorded using pClamp 10.4 Axoscope software (Molecular Devices) with a 50 kHz rate of data recording. All experiments were performed using a two-electrode setup placed in a lab-built Faraday cage.

Homemade Ag/AgCl electrodes, which were fabricated by dipping a silver wire (0.1 mm diameter, Alfa Aesar) in ferric chloride, were used as reference electrodes for all electrochemical measurement. A constant pressure was applied from the outside of the pipette vs. inside by a FemtoJet microinjector (Eppendorf) in continuous flow mode, as shown in Figure 5.1.

5.3 Results and Discussion

5.3.1 *Fabrication of Glass Microbulb*

The glass microbulb was fabricated with a conventional patch-pipette microforge that uses a Pt wire as heating filament to melt glass. The pulled borosilicate nanopipette was mounted in an electrode holder, as shown in Figure 5.2. The end of the pipette was connected to a N_2 gas tank. The nanopipette was heated on the microforge for several seconds to form a complete seal at the pipette tip. Then pressurized N_2 (~ 20 - 30 psi) was directed into the pipette while the pipette was heated until the glass wall at the pipette tip fully expanded to a form a spherical bulb (~80 μm in diameter). Different kind of glass pipette was used to fabricate the microbulb, such as quartz, and soda lime glass. The borosilicate glass has the appropriate melting point and softness and was used to make in the entire experiment. The glass microbulb was later coated with a thin film of carbon and milled by focused ion beam (FIB).[21] The microbulb was characterized by SEM. It could also be characterized by measuring resistance in an electrolyte solution. As the current-voltage response shown in Figure 5.3, the ionic resistance of a 435 nm diameter pore is calculated to be 3.64 M Ω, indicating the length of the pore is 378 nm.

5.3.2 *Detection of 80 nm and 200 nm Liposomes*

The glass microbulb has much larger space than a nanopipette and can be used as a high throughput single vesicle sensor without clogging issue. Single particle detection and analysis with a nanopore is based on a resistive pule-sensing mechanism. It is well known that a transient current spike in conventional resistive-pulse sensing experiments is caused by an analyte particle excluding a certain volume of solution when it translocates through the sensing zone or a nanopore.[13,15,22] The magnitude of the current pulse is largely determined by the volume ratio between the analyte particle and the nanopore. In order to verify the accuracy of this method, 80 nm and 200 nm artificial liposomes were detected by the microbulb first. As shown in Figure 5.4a, a representative current-time trace shows 80 nm liposome translocation through nanopore when +1 V was applied in internal solution vs. external solution between two Ag/AgCl reference electrodes. Liposomes were diluted 20 times by running buffer after preparation. 10 psi pressure was applied by FemtoJet inside the pipette for the purpose of pushing liposomes out of the glass bulb. The translocation of single liposomes is shown as individual resistive current pulses in the current-time trace, which is not seen in the control experiment without liposomes. Typical current spikes are given in Figure 5.4a as the inset. The full width at half maximum (FWHM) of the current spike shows a narrow distribution in Figure 5.4c. The average FWHM is 0.24 ± 0.37 ms, as summarized in Table 5.4. The asymmetric triangular peak shape reflects the slightly conical geometry of the nanopore formed in the FIB milling process. For the resistive current pulses, the magnitude of the spike can be readily determined. The magnitude was divided by the baseline current to calculated the percentage of current blockage. The average % current blockage is 0.31%. The distribution of %current blockage was shown in Figure 5.5d. The size estimated from the average %current blockage is 77 nm, which is very close to 80 nm.

The result of 200 nm liposome detection was shown in Figure 5.5. Compared with the result from 80 nm liposomes, the average translocation time of 200 nm liposome is much longer. The average FWHM is 54.6 ± 52.8 ms. Also, the resistive current spikes show a wider distribution in FWHM (Figure 5.5c). The % current blockage (Table 5.4) was summarized to be 3.6 ± 0.6%, which is also much larger than the result from 80 nm liposomes. The size estimated from the average %current blockage is 190 nm, which is very close to 200 nm! The results from 80 nm and 200 nm liposomes demonstrates that the size of artificial liposomes can be accurately determined by the resistive pulse method using our glass microbulb. Moreover, the significant difference in both translocation time and % current blockage enables us to distinguish different sized vesicles very easily.

5.3.3 *Detection of Isolated Vesicles from PC12 Cells*

We used the same method to analyze single vesicles isolated from PC12 cells. The vesicles were diluted 100 times by homogenizing buffer after isolated from cells. In order to avoid possible deformation of vesicles when they translocate through the nanopore, larger nanopores were chosen intentionally, as the SEM image shows in Figure 5.6b. Figure 5.6a displays a representative current-time trace showing single vesicle detection and the detail of current spike is given in the inset of Figure 5.6a. 0.5 V was applied in internal solution vs. external solution between two Ag/AgCl reference electrodes. A 30 psi pressure was applied by FemtoJet inside the pipette for the purpose of pushing vesicles out of the glass bulb. Every single current resistive pulse represents a translocation event of a single vesicle through the nanopore. Statistical results were extracted from the resistive current spikes and summarized in Figure 5.7. Compared with the results from 80 nm and 200 nm liposomes, the vesicles isolated from PC12 cells exhibits a broader dispersion in current magnitude (Figure 5.7d), indicating the large variation in vesicle size. The shape of the

current spike (inset of Figure 5.6a) was similar to those observed with liposomes, suggesting that the vesicles could be analyzed in a similar manner. The %current blockage calculated from 124 events is 4.95 ± 6.74%. The vesicle size calculated form the average %current blockage is 221 nm, which is consistent with what was reported before.[18]

5.4 Conclusions and Future Work

Glass microbulb was fabricated with a simple pressure-polishing method. A microbulb has very large surface and huge inside volume, and ultrathin glass wall. Nanopores could be milled on the bulb with focused ion beam, metal nanoparticles could be modified on the bulb and act as nanoelectrodes. Due to the large surface area, the bulb could support multiple pores and nanoelectrode arrays. Moreover, the huge volume of the bulb is beneficial because the diffusion of molecules is not limited by the geometry, and there is less nanoparticles clogging issue. We believe this bulb could have wide applications in single molecule and nanoparticle sensing. Here we used it as a high throughput single vesicle analyzer. Artificial liposomes and vesicles isolated from PC12 cells in the range of 80 - 200 nm in diameter were detected and sized with nanopore sensing technique. The size of the nanopore can be easily controlled during FIB milling process. With a smaller nanopore size it can be used in the future to characterize synaptic vesicles that are 30 - 50 nm in size. Our results show similar particle size distribution to the result reported before.[18] This method allows high throughput and noninvasive detection of vesicles. Moreover, this method could be combined with other analytical methods to obtain more information about biological samples.

In the future we will continue to build a high-throughput single-vesicle analyzer using a nanopore integrated to a microelectrode. Using resistive-pulse sensing, the nanopore sensor will give accurate size information of vesicles flowing through it. The microelectrode placed right after

the nanopore can measure dopamine content of the same vesicles. The ability to correlate vesicle size with neurotransmitter concentration and copy number of vesicular proteins, can greatly advance our understanding of neurotransmission.

5.5 TABLES AND FIGURES

Table 5.4. Half width and % current blockage of liposomes and vesicles

	Average half-width (FWHM) / ms	% current blockage
80 nm liposome	0.27 ± 0.37	0.31 ± 0.33
200 nm liposome	54.6 ± 52.8	3.6 ± 0.6
Vesicles	0.39 ± 0.09	4.95 ± 6.74

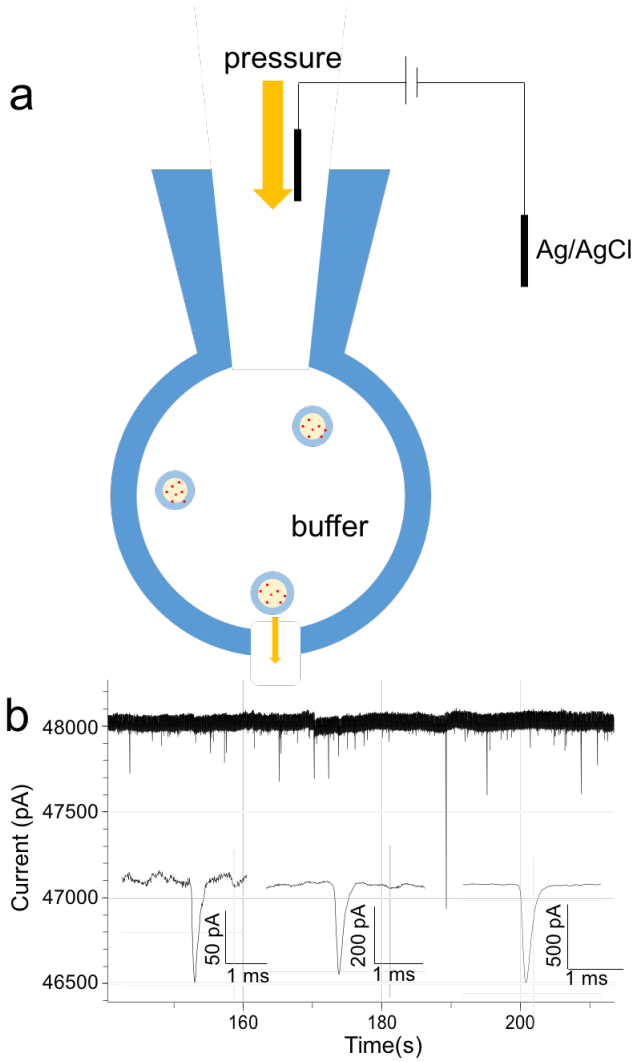

Figure 5.1. Schematic of experimental setup to detect single vesicles

(a) A schematic showing nanopore sensing of single vesicles. Vesicles are pushed out of a glass nanopore causing a change in the nanopore's ionic current (b) A representative current-time trace showing detection of vesicles isolated from PC12 cells. The insets are typical current spikes of single events. The nanopore is ~400 nm in diameter.

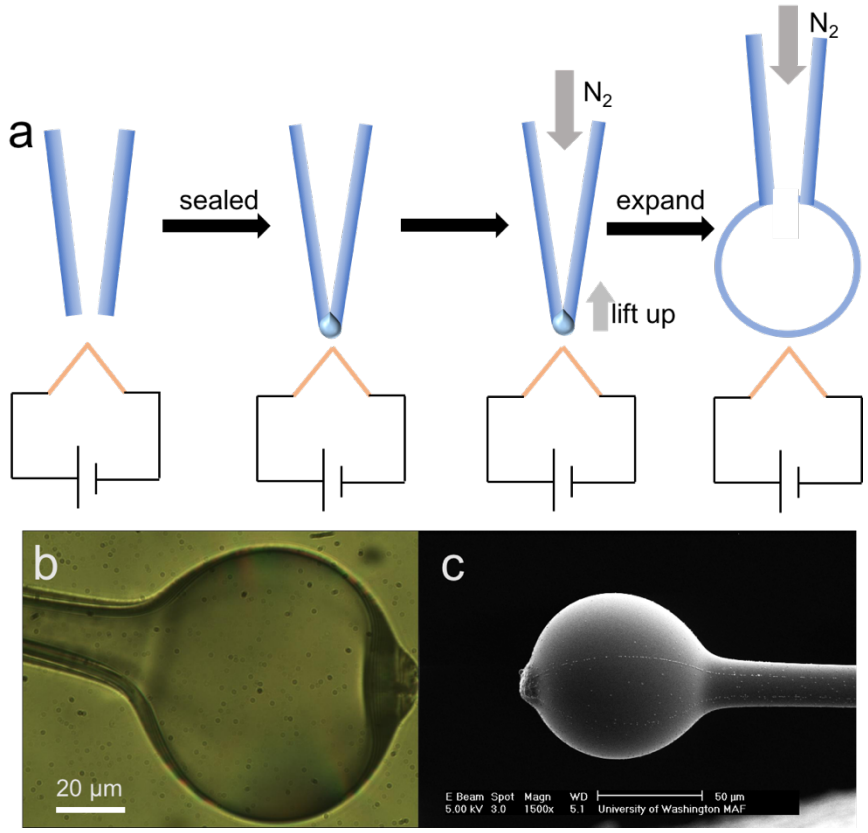

Figure 5.2. Schematic depicting the fabrication of glass microbulb

(a) The schematic depicts the fabrication of glass microbulb. (b) is an optical picture of a glass microbulb. (c) The SEM image of the same glass microbulb as in (b).

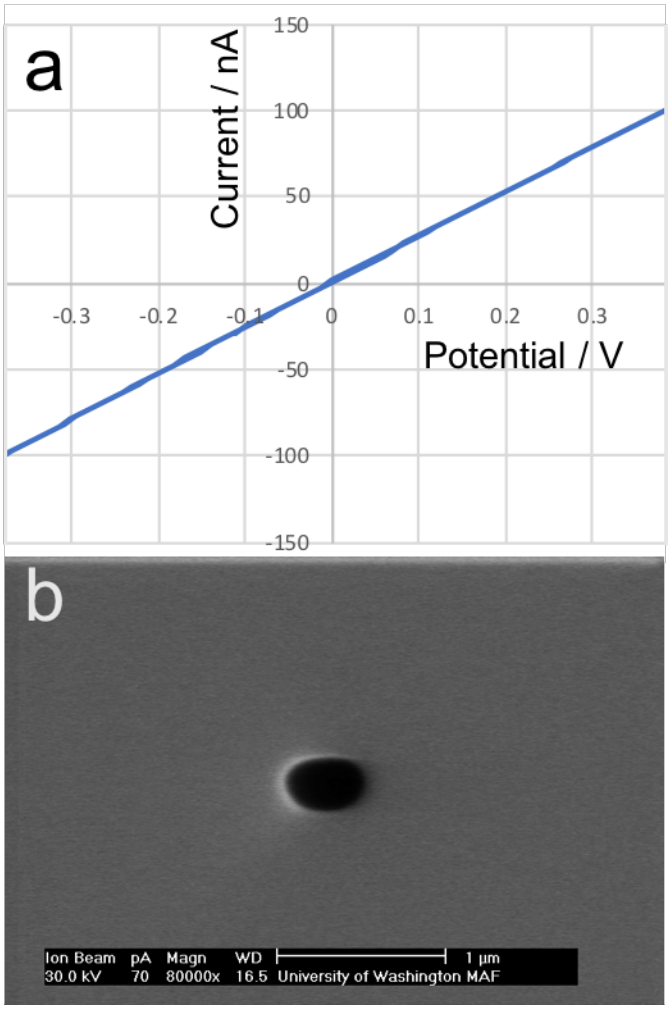

Figure 5.3. i-V curve and SEM imaging of a FIB-milled nanopore

(a) A representative i-V curve of a 435 nm nanopore in 100 mM KCl. The scan rate was 100 mV/s. The pipette pore diameter was calculated from the ionic resistance. (b) SEM image of the same nanopore with a diameter ~ nm. The potential in (a) was applied between two Ag/AgCl quasi-reference electrodes (QREs).

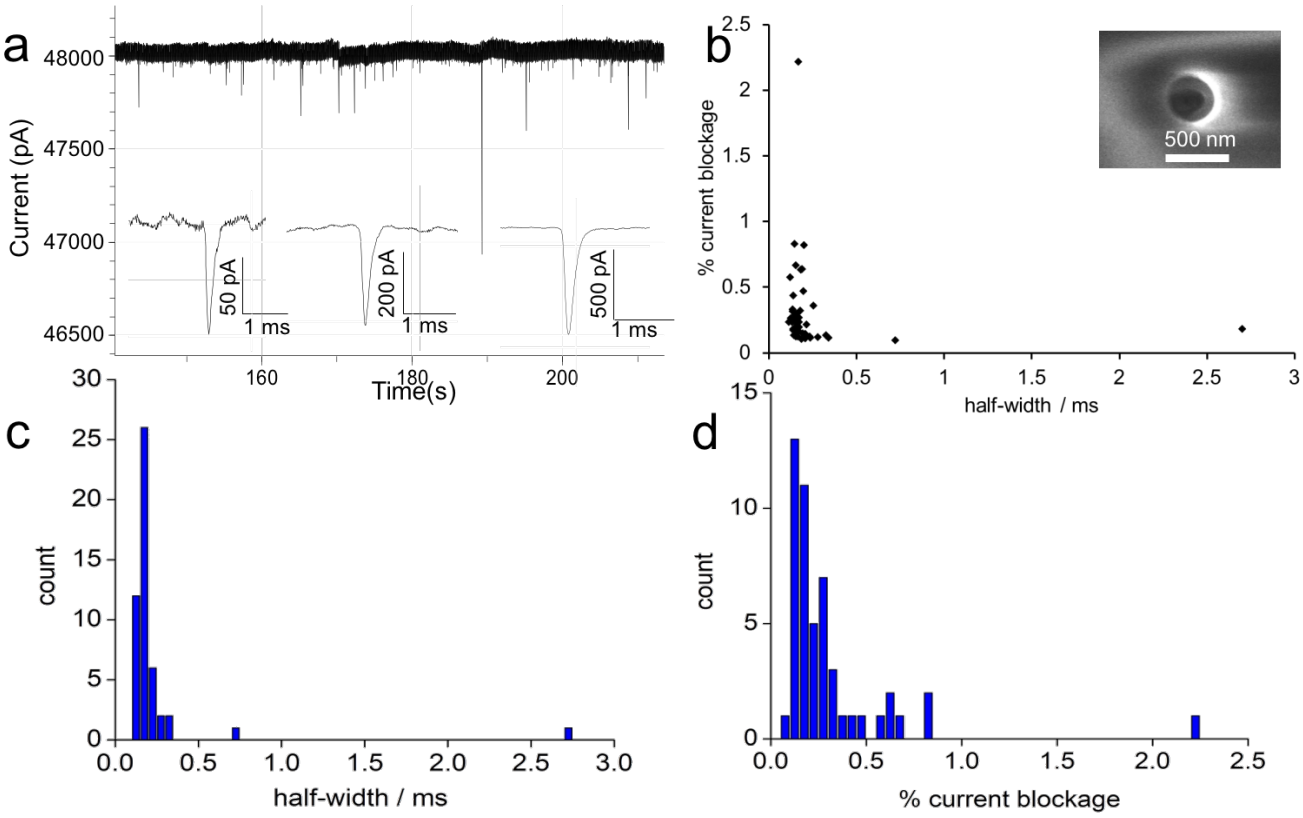

Figure 5.4. Nanopore detection of 80 nm liposome

(a) A representative current-time trace showing 80 nm liposome translocation through a nanopore (OD = 347 nm ID = 255 nm L= 690 nm) on glass bulb. Condition: +1 V was applied in internal solution vs. external solution between two Ag/AgCl reference electrodes. The solution was running buffer. Liposomes were diluted 20 times by running buffer. 10 psi pressure was applied by a FemtoJet inside the pipette for the purpose of pushing liposomes out of the glass bulb. (b) % current blockage vs. translocation time (half-width), inset figure is a SEM image of the nanopore. (c) Histogram of translocation time distribution (half width) (d) Histogram of % current blockage distribution.

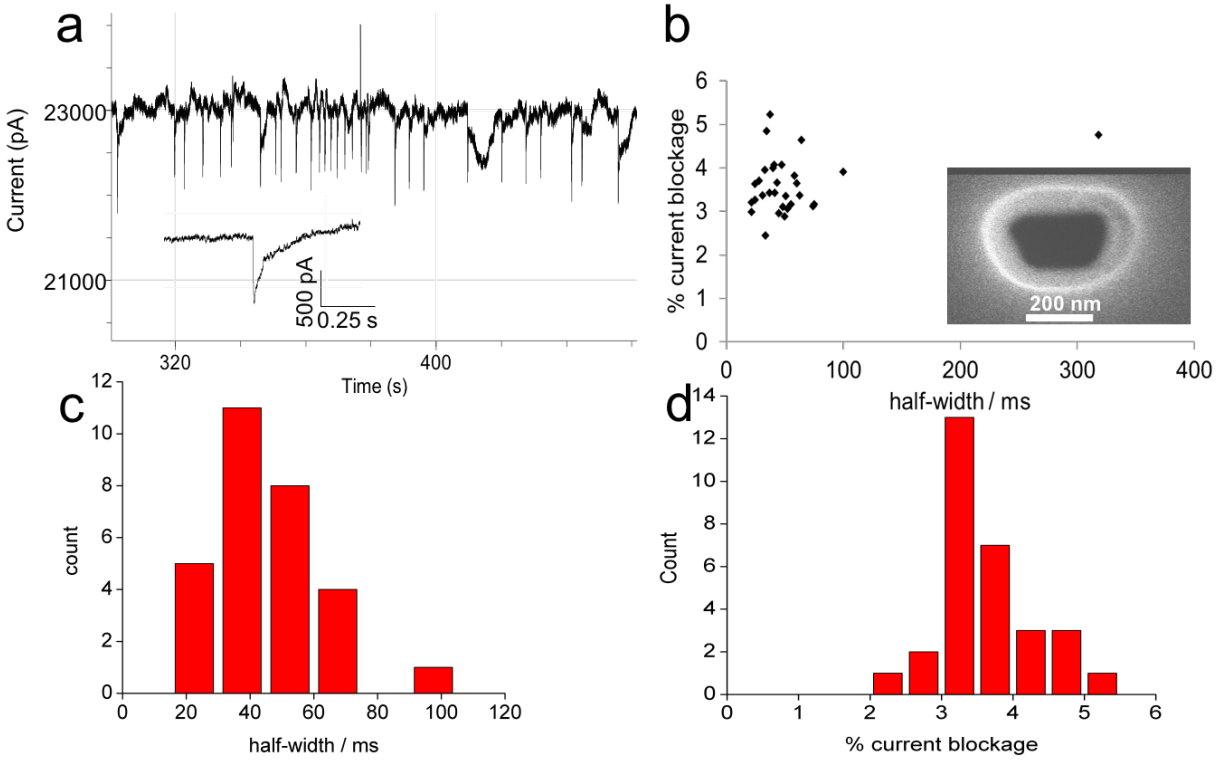

Figure 5.5. Nanopore detection of 200 nm liposome

(a) A representative current-time trace showing 200 nm liposome translocation through a nanopore (OD 448 nm ID 254 nm L=2.55 μm) on glass bulb. Condition: +1 V was applied in internal solution vs. external solution between two Ag/AgCl reference electrodes. The solution was running buffer. Liposomes were diluted 20 times by running buffer. 30 psi pressure was applied by FemtoJet inside the pipette for the purpose of pushing liposomes out of the glass bulb. (b) % current blockage vs. translocation time (half-width), inset figure is a SEM image of the nanopore. (c) Histogram of translocation time distribution (half width) (d) Histogram of % current blockage distribution.

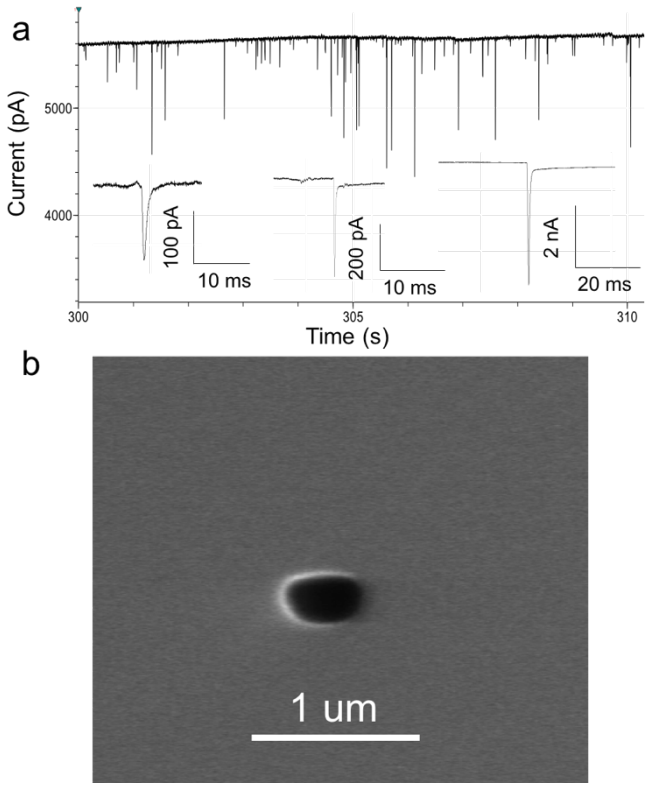

Figure 5.6. Nanopore detection of single isolated vesicles

(a) A 20-s current-time trace showing vesicles (from PC12 cells) translocation through nanopore on glass bulb. Condition: +0.5 V was applied in internal solution vs. external solution between two Ag/AgCl reference electrodes. The solution was homogenizing buffer. Vesicles were diluted 100 times by homogenizing buffer after isolated from cells. 30 psi pressure was applied by FemtoJet inside the pipette for the purpose of pushing vesicles out of the glass bulb. (b) A SEM image of the nanopore used in the nanoparticle translocation experiment.

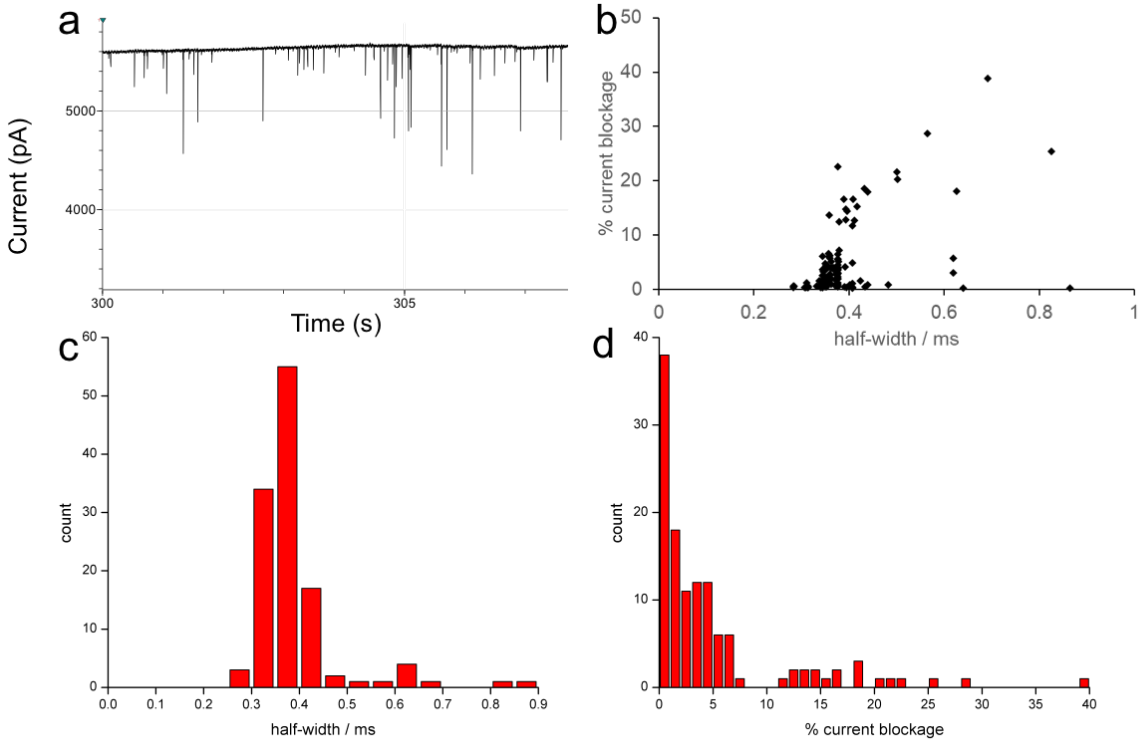

Figure 5.7 Data analysis of nanopore detection of vesicles

(a) A representative current-time trace showing vesicles (from PC12 cells) translocation through nanopore on glass bulb. (b) % current blockage vs. translocation time (half-width). (c) Histogram of translocation time (half width). (d) Histogram of % current blockage.

5.6 REFERENCES

(1) Iraci, N.; Gaude, E.; Leonardi, T.; Costa, A. S. H.; Cossetti, C.; Peruzzotti-Jametti, L.; Bernstock, J. D.; Saini, H. K.; Gelati, M.; Vescovi, A. L.; Bastos, C.; Faria, N.; Occhipinti, L. G.; Enright, A. J.; Frezza, C.; Pluchino, S. Extracellular Vesicles are Independent Metabolic Units with Asparaginase Activity. *Nat. Chem. Biol.* **2017**, *13*, 951-955.

(2) Alberts, B.; Johnson, A.; Lewis, J.; Raff, M.; Roberts, K.; Peter, W. Molecular Biology of the Cell; Garland Science: New York, 2002.

(3) Jahn, R.; Sudhof, T. C. Synaptic Vesicles and Exocytosis. *Annu. Rev. Neurosci.* **1994**, 17, 219-246.

(4) Sudhof, T. C.; Jahn, R. Proteins of Synaptic Vesicles involved in Exocytosis and Membrane Recycling. *Neuron*, **1991**, *6*, 665-677.

(5) Hallett, F. R.; Watton, J.; Krygsman, P. Vesicle Sizing: Number Distributions by Dynamic Light Scattering. *Biophys. J.* **1991**, *59*, 357-362.

(6) Gardiner, C.; Ferreira, Y. J.; Dragovic, R. A.; Redman, C. W. G.; Sargent, I. L. Extracellular Vesicle Sizing and Enumeration by Nanoparticle Tracking Analysis. *J. Extracell. Vesicles* **2013**, *2*, 1-11.

(7) Talmon, Y.; Burns, J. L.; Chestnut, M. H.; Siegel, D. P. Time-resolved Cryotransmission Electron Microscopy. *J. Electron Microsc*. **1990**, *14*, 6-12.

(8) Yuana, Y.; Oosterkamp, T.H.; Bahatyrova, S.; Ashcroft, B.; Garcia Rodriguez, P.; Bertina, R.M.; Osanto, S. Atomic Force Microscopy: a Novel Approach to the Detection of Nanosized Blood Microparticles. *J. Thromb. Haemost.* **2010**, *8*, 315-323.

(9) Sun, B. Y.; Chiu, D. T. Determination of the Encapsulation Efficiency of Individual Vesicles Using Single-Vesicle Photolysis and Confocal Single-Molecule Detection. *Anal. Chem.* **2005**, *77*, 2770-2776.

(10) Ganesana, M.; Lee, S. T.; Wang, Y.; Venton, B. J. Analytical Techniques in Neuroscience: Recent Advances in Imaging, Separation, and Electrochemical Methods. *Anal. Chem.* **2017**, *89*, 314-341.

(11) Adams, K. L.; Jena, B. K.; Percival, S. J.; Zhang, B. Highly Sensitive Detection of Exocytotic Dopamine Release Using a Gold-Nanoparticle-Network Microelectrode. *Anal. Chem.* **2011**, *83*, 920-927.

(12) Barlow, S. T.; Louie, M.; Hao, R.; Defnet, P. A.; Zhang, B. Electrodeposited Gold on Carbon-Fiber Microelectrodes Enhances Amperometric Detection of Dopamine Release from PC12 Cells. *Anal. Chem*. **2018**, *90*, 10049-10055.

(13) Ito, T.; Henriquez, R. R.; Crooks, R. M. A Carbon Nanotube-Based Coulter Nanoparticle Counter. *Acc. Chem. Res.* **2004**, *37*, 937-945.

(14) Shi, W.; Friedman, A. K.; Baker, L. A. Nanopore Sensing. *Anal. Chem.* **2017**, *89*, 157-188.

(15) Bayley, H.; Martin, C. R. Resistive-Pulse Sensing-From Microbes to Molecules. *Chem. Rev.* **2000**, *100*, 2575-2594.

(16) Heins, E. A.; Siwy, Z. S.; Baker, L. A.; Martin, C. R. Detecting Single Porphyrin Molecules in a Conically Shaped Synthetic Nanopore. *Nano Lett.* **2005**, *5*, 1824-1829.

(17) Luo, L.; German, S. R.; Lan, W.-J.; Holden, D. A.; Mega, T. L.; White, H. S. Resistive-Pulse Analysis of Nanoparticles. *Annu. Rev. Anal. Chem.* **2014**, *7*, 513-535.

(18) Li, X.; Dunevall, J.; Ewing, A. G. Electrochemical Quantification of Transmitter Concentration in Single Nanoscale Vesicles Isolated from PC12 Cells. *Faraday Discuss*. **2018**, *210*, 353-364.

(19) Lovric, J.; Najafinobar, N.; Dunevall, J.; Majdi, S.; Svir, I.; Oleinick, A.; Amatore, C.; Ewing, A. G. On the Mechanism of Electrochemical Vesicle Cytometry: Chromaffin Cell Vesicles and Liposomes. *Faraday Discuss*., **2016**, *193*, 65-79.

(20) Li, X.; Dunevall, J.; Ren, L.; Ewing, A. G. Mechanistic Aspects of Vesicle Opening during Analysis with Vesicle Impact Electrochemical Cytometry. *Anal. Chem*. **2017**, *89*, 9416-9423.

(21) Hao, R.; Fan, Y.; Han, C.; Zhang, B. Bipolar Electrochemistry on a Nanopore-Supported Platinum Nanoparticle Electrode. *Anal. Chem*. *2017*, **89**, 12652-12658.

(22) Fan, Y.; Han, C.; Zhang, B. Recent Advances in the Development and Application of Nanoelectrodes. *Analyst*, **2016**, *141*, 5474-5487.

Chapter 6. SUMMARY AND FUTURE WORK

In conclusion, this dissertation can be separated to two parts. The first part discusses the study of nanoscale materials with electrochemical methods. We investigate the redox behavior of single nanoparticles and nanoparticle films with voltammetry techniques. In the other part, we aim to develop new electrochemical methods to discover more complicated information from nanoparticles and extend its application in electrocatalysis and biological study.

We first described the preparation, characterization, and electrochemical study of conductive, ultrathin films of cross-linked metal nanoparticles. Nanoporous films ranging from 40 to 200 nm in thickness composed of gold and platinum nanoparticles of ~5 nm can be fabricated via a powerful layer-by-layer spin coating process. This process allows preparation of uniform nanoparticle films as large as 2×2 cm^2 with precise control over thickness, structure, and electrochemical and electrocatalytic properties. Gold, platinum, and bimetallic nanoparticle films were fabricated and characterized using cyclic voltammetry, scanning electron microscopy, and conductance measurements. Their electrocatalytic activity toward the oxygen reduction reaction (ORR) was investigated. Our results show that the electrochemical activity of such nanoparticle films is initially hindered by the presence of dense thiolate cross-linking ligands. Both electrochemical cycling and oxygen plasma cleaning are effective means in restoring their electrochemical activity. Gold nanoparticle films have higher electric conductivity than platinum possibly due to more uniform film structure and closer particle−particle distance. The electrochemical and electrocatalytic performance of platinum nanoparticle films can be greatly enhanced by the incorporation of gold nanoparticles. This work focuses on electrochemical characterization of cross-linked nanoparticle films and demonstrates several unique properties.

These include quick and easy preparation, ultrathin and uniform film thickness, tunable structure and composition, and transferability to many other substrates.

Next, we turned to study fundamental properties of single nanoparticles. we report the electrochemical characterization of Janus Au-silica nanoparticles at the single particle level with single-nanoparticle collision method. By holding a constant potential on an inert carbon ultramicroelectrode, current transient can be induced and detected when a single Janus nanoparticle lands on the electrode surface and catalyzes the reaction of the redox indicator. Different molecules such as hydrazine and proton were examined in the Janus nanoparticle collision experiment. By comparing the diffusion-limited current steps of Janus nanoparticles to the current of Au nanoparticles, we were able to calculate the electroactive area of Au-SiO_2 nanoparticles. Through the simulation of the hydrazine concentration profile on the Au-SiO_2 nanoparticle, the geometry was correlated with electroactivity. This work demonstrates that nanoparticle collision experiment can be a simple and efficient technique to characterize single Janus nanoparticles and study the geometry quantitatively.

We also developed new electrochemical methods for the characterization of single nanoparticles. In the next chapter we report the observation of transient bipolar electrochemical coupling on freely-moving 40 nm silver nanoparticles. The use of an asymmetric nanoscale electrochemical environment at the nanopore orifice, e.g., an acid inside the pipette and halide ions in the bulk, enabled us to observe unusually large current blockages of single Ag nanoparticles. We attribute these current blockages to the formation of H2 nanobubbles on the surface of translocation of Ag nanoparticles due to the coupled faradaic reactions, in which the reduction of protons and water is coupled to the oxidation of Ag and water under potentials higher than 1 V. The appearance of large current blockages was strongly dependent on voltage and the choice of

anions in the bulk solution. The correlation between large current blockages with the oxidation of Ag nanoparticles and their nanopore translocation was further confirmed by simultaneous fluorescence and electric recordings. This study demonstrates that transient bipolar electrochemistry can take place on small metal nanoparticles below 50 nm when they pass through nanopores where the electric field is highly localized. The use of a nanopore and the resistive-pulse sensing method to study transient bipolar electrochemistry of nanoparticles may be extended to the future studies in ultrafast electrochemistry, nanocatalyst screening, and gas nucleation on nanoparticles.

We summarized efforts to develop new tools for analyzing single isolated vesicles. In chapter 5, glass nanopores were fabricated and used to detect and analyze individual artificial vesicles ranging from 100 to 300 nm and dopaminergic vesicles isolated from PC12 cells. The average diameter estimated from the current signal was 221 nm, in good agreement with the known PC12 cell vesicles. In the future we will continue to build a high-throughput single vesicle analyzer with a nanopore integrated with an ultramicroelectrode. Using resistive-pulse sensing, the nanopore sensor will give accurate size information of vesicles flowing through it. The microelectrode placed right after the nanopore can measure dopamine content of the same vesicles.

BIBLIOGRAPHY

Adams, K. L.; Jena, B. K.; Percival, S. J.; Zhang, B. *Anal. Chem.* **2011**, *83*, 920-927.

Alberts, B.; Johnson, A.; Lewis, J.; Raff, M.; Roberts, K.; Peter, W. Molecular Biology of the Cell; Garland Science: New York, 2002.

Alexeyeva, N.; Laaksonen, T.; Kontturi, K.; Mirkhalaf, F.; Schiffrin, D. J.; Tammeveski, K. *Electrochem. Commun*. **2006**, 8, 1475-1480.

Anicet, N.; Bourdillon, C.; Moiroux, J.; Saveant, J. M. *J. Phys. Chem. B* **1998**, *102*, 9844-9849.

Arora, A.; Eijkel, J. C. T.; Morf, W. E.; Manz, A. *Anal. Chem.* **2001**, *73*, 3282–3288. Avasare, V.; Zhang, Z.; Avasare, D.; Khan, I.; Qurashi.; A. *Int. J. Energy Res.,* **2015**, *39*, 1714-1719.

Bahshi, L.; Frasconi, M.; Tel-Vered, R.; Yehezkeli, O.; Willner, I. *Anal. Chem.* **2008**, *80*, 8253-8259.

Ballarin, B.; Cassani, M. C.; Scavetta, E.; Tonelli, D. *Electrochem. Acta* **2008**, *53*, 8034-8044.

Bard, A. J.; Faulkner, L. R. Elecrochemical Methods, 2nd ed.; John Wiley & Sons: New York, 2001.

Bartlett, P. N.; Baumberg, J. J.; Birkin, P. R.; Ghanem, M. A.; Netti, M. C. *Chem. Mater.* **2002**, *14*, 2199-2208.

Barlow, S. T.; Louie, M.; Hao, R.; Defnet, P. A.; Zhang, B. Electrodeposited Gold on Carbon-Fiber Microelectrodes Enhances Amperometric Detection of Dopamine Release from PC12 Cells. *Anal. Chem*. **2018**, *90*, 10049-10055.

Bayley, H.; Cremer, P. S. *Nature* **2001**, *413*, 226-230.

Bayley, H.; Martin, C. R. *Chem. Rev.* **2000**, *100*, 2575-2594.

Bezrukov, S. M.; Vodyanoy, I.; Parsegian, V. A. *Nature* **1994**, *370*, 279-281.

Biji, P.; Patnaik, A. *Analyst*, **2012**, *137*, 4795-4801.

Boika, A.; Thorgaard, S. N.; Bard, A. J. *J. Phys. Chem. B*. **2013**, *117*, 4371-4380.

Boontongkong, Y.; Cohen, R. E. *Macromolecules* **2002**, *35*, 3647-3652.

Brasiliense, V.; Patel, A.N.; Martinez-Marrades, A.; Shi, J.; Chen, Y.; Combellas, C.; Tessier, G.; Kanoufi, F. *J. Am. Chem. Soc.* **2016**, *138*, 3478-3483.

Brown, K. R.; Fox, A. P.; Natan, M. J. *J. Am. Chem. Soc.* **1996**, *118*, 1154-1157.

Brust, M.; Stuhr-Hansen, N.; Norgaard, K.; Christensen, J. B.; Nielsen, L. K.; Bjornholm, T. *Nano Lett.* **2001**, *1*, 189-191.

Burke, L. D.; Cunnane, V. J. *J. Electroanal. Chem.* **1986**, *210*, 69-94.

Byers, J. C.; Paulose Nadappuram, B.; Perry, D.; McKelvey, K.; Colburn, A. W.; Unwin, P. R. *Anal. Chem.* **2015**, *87*, 10450-10456.

Campbell, C. T.; Sellers J. R. V. *Farad. Discuss.* **2013**, *162*, 9-30.

Campbell, F. W.; Compton, R. G.; *Anal. Bioanal. Chem.,* **2010,** *396*, 241-259.

Cannes, C.; Kanoufi, F.; Bard, A. J. *J. Electroanal. Chem.* **2003**, *547*, 83-91.

Castner, D. G.; Hinds, K.; Grainger, D. W. Langmuir, 1996, 12, 5083-5086.

Chen, T.; Chen, G.; Xing, S.; Wu, T.; Chen, H. *Chem. Mater.* **2010**, *22*, 3826-3828.

Chen, P.; McCreery, R. L. *Anal. Chem.* **1996**, *68*, 3958-3965.

Cheng, W.; Compton, R. G. Angew. Chem., Int. Ed. 2014, 53, 13928-13930. Cheng, W.; Compton, R. G. *Angew. Chem., Int. Ed.* **2015**, *54*, 7082-7085.

Chow, K.-F.; Mavre´, F.; Crooks, R. M. *J. Am. Chem. Soc*. **2008**, *130*, 7544-7545.

Coulter, W. H. U.S. Patent 2656508, October 20, 1953.

Cox, J. T.; Guerrette, J. P.; Zhang, B. *Anal. Chem.* **2012**, *84,* 8797-8804.

Cox, J. T.; Zhang, B. *Annu. Rev. Anal. Chem.* **2012**, *5*, 253-272.

Cui, H.-F.; Ye, J.-S.; Zhang, W.-D.; Wang, J.; Sheu, F.S. *J. Electroanal. Chem.* **2005**, *577*, 295-302.

Deamer, D. W.; Branton, D. *Acc. Chem. Res.* **2002**, *35*, 817-825.

Decher, G. *Science* **1997**, *277*, 1232-1237.

Deblois, R. W.; Bean, C. P. *Rev. Sci. Instrum*. **1970**, *41*, 909-916.

Deblois, R. W.; Bean, C. P.; Wesley, R. K. A. *J. Colloid Interface Sci.* **1977**, *61*, 323-335.

Deblois, R. W.; Wesley, R. K. A. *J. Virol.* **1977**, *23*, 227-233.

Decher, G.; Hong, J. D. *Makromol. Chem., Macromol. Symp.* **1991**, *46*, 321-327.

Demirok, U. K.; Laocharoensuk R.; Manesh, K. M.; Wang, J. *Angew. Chem. Int. Ed.* **2008**, *47*, 9349-9351.

Dick, J. E.; Renault, C.; Bard, A. J. *J. Am. Chem. Soc.* **2015**, *137*, 8376-8379.

Dick, J. E.; Hilterbrand, A. T.; Strawsine, L. M.; Upton, J. W.; Bard, A. J. *Proc. Natl. Acad. Sci. U. S. A* **2016**, *113*, 6403-6408.

Ding, Y.; Kim, Y. J.; Erlebacher, J. *Adv. Mater*. **2004**, *16*, 1897-1900.

Dumitrescu, I.; Anand, R. K.; Fosdick, S. E.; Crooks, R. M. *J. Am. Chem. Soc.* **2011**, *133*, 4687-4689.

Dunevall, J.; Fathali, H.; Najafinobar, N.; Lovric, J.; Wigstrom, J.; Cans, A. S.; Ewing, A. G. *J. Am. Chem. Soc.* **2015**, *137*, 4344-4346.

Erlebacher, J.; Snyder, J. *ECS Trans.* **2009**, *25*, 603-612.

Fan, F. R.; Bard, A. J. *Science* **1995**, *267*, 871-874.

Fan, H. Y.; Wright, A.; Gabaldon, J.; Rodriguez, A.; Brinker, C. J.; Jiang, Y. B. *Adv. Funct. Mater.* **2006**, *16*, 891-895.

Fan, Y.; Anderson, T. J.; Zhang, B. *Curr. Opin. Electrochem.* **2018**, *7*, 81-86.

Fan, Y.; Han, C.; Zhang, B. *Analyst*, **2016**, *141*, 5474-5487.

Fang, Y.; Wang, W.; Wo, X.; Luo, Y.; Yin, S.; Wang, Y.; Shan, X.; Tao, N. *J. Am. Chem. Soc.* **2014**, *136*, 12584-12587.

Fattah, Z.; Garrigue, P.; Goudeau, B.; Lapeyre, V.; Kuhn, A.; Bouffier, L. *Electrophoresis* **2013**, *34*, 1985-1990.

Fattah, Z.; Garrigue, P.; Lapeyre, V.; Kuhn, A.; Bouffier, L. *J. Phys. Chem. C.* **2012**, *116*, 22021-22027.

Fernando, A.; Parajuli, S.; Alpuche-Aviles, M. A. *J. Am. Chem. Soc.* **2013**, *135*, 10894-10897.

Fosdick, S. E.; Anderson, M. J.; Nettleton, E. G.; Crooks, R. M. *J. Am. Chem. Soc.* **2013**, *135*, 5994-5997.

Fosdick, S.E.; Crooks. R. M. *J. Am. Chem. Soc.* **2012**, *134*, 863-866.

Fosdick, S. E.; Knust, K. N.; Scida, K.; Crooks, R. M. *Angew. Chem. Int. Ed.* **2013**, *52*, 10438–10456.

Frens, G. *Nature Phys. Sci.* **1973**, *241*, 20-22.

Fu, K.; Bohn, P. W. *ACS Cent. Sci.* **2018**, *4*, 20-29.

Fu, K.; Han, D.; Crouch, G. M.; Kwon, S. R.; Bohn, P. W. *Small* **2018**, *14*, 1703248.

Fu, S.; Yang, G.; Zhou,Y.; Pan, H-B.; Wai, C. M.; Dan D.; Lin Y. *RSC Adv.* **2015**, *5*, 32685-32689.

Ganesana, M.; Lee, S. T.; Wang, Y.; Venton, B. J. *Anal. Chem.* **2017**, *89*, 314-341.

Gardiner, C.; Ferreira, Y. J.; Dragovic, R. A.; Redman, C. W. G.; Sargent, I. L. *J. Extracell. Vesicles* **2013**, *2*, 1-11.

Giovanni, M.; Ambrosi, A.; Sofer, Z.; Pumera, M. *Electrochem. Commun.* **2015**, *56*, 16-19.

Gong, M.; Li, Y.; Wang, H.; Liang, Y.; Wu, J.; Zhou, J.; Wang, J.; Regier, T.; Wei, F.; Dai, H. J. *Am. Chem. Soc.* **2013**, *135*, 8452-8455.

Gorlin, Y.; Chung, C. J.; Nordlund, D.; Clemens, B. M.; Jaramillo, T. F. *ACS Catal.* **2012**, *2*, 2687−2694.

Grzelczak, M.; Vermant, J.; Furst, E. M.; Liz-Marzán, L. M. *ACS Nano*. **2010**, *4*, 3591-3605.

Guerrette, J. P., Percival, S. J., Zhang, B. *J. Am. Chem. Soc*. **2013**, 135, 855-861.

Guerrette, J. P.; Zhang, B. *J. Am. Chem. Soc.* **2010**, *132*, 17088-17091.

Guo W.; Pi Y.; Song H.; Tang W.; Sun. J. *Colloids and Surfaces A: Physicochemical and Engineering Aspects* **2012**, *415*, 105-111.

Guo, W.; Cui, Y.; Song, H.; Sun, J. *Bioprocess Biosys. Engi.* **2014**, *37*, 1749-1758.

Guo, Z.; Percival, S. J.; Zhang, B. *J. Am. Chem. Soc.* **2014**, *136*, 8879-8882.

Hallett, F. R.; Watton, J.; Krygsman, P. *Biophys. J.* **1991**, *59*, 357-362.

Hammond, P. T. *Adv. Mater.* **2004**, *16*, 1271-1293.

Hanarp, P.; Sutherland, D. S.; Gold, J.; Kasemo, B. *Colloids Surf. A* **2003**, *214*, 23-26.

Hao, R.; Fan, Y.; Howard, M. D.; Vaughan, J. C.; Zhang, B. *Proc. Natl. Acad. Sci. U.S.A.* **2018**, *115*, 5878-5883.

Hao, R.; Fan, Y.; Han, C.; Zhang, B. *Anal. Chem*. *2017*, **89**, 12652-12658.

Hao, R.; Fan. Y.; Zhang, B. *J. Am. Chem. Soc.* **2017**, *139*, 12274-12282.

Heins, E. A.; Siwy, Z. S.; Baker, L. A.; Martin, C. R. *Nano Lett.* **2005**, *5*, 1824-1829.

Henriquez, R. R.; Ito, T.; Sun, L.; Crooks, R. M. *Analyst* **2004**, *129*, 478-482.

Hernandez J.; Solla-Gullo, J.; Herrero, E.; Aldaz, A.; Feliu, J. M. *J. Phys. Chem. C.* **2007**, *111*, 14078-14083.

Hill, C. M.; Bennett, R.; Zhou, C.; Street, S.; Zheng, J.; Pan, S. *J. Phys. Chem. C.* **2015**, *119*, 6760-6768.

Hill, C. M.; Pan, S. *J. Am. Chem. Soc*. **2013**, *135*, 17250-17253.

Holden, D.A.; Hendrickson, G., Lyon, L.A.; White, H.S. *J. Phys. Chem. C* **2011**, *115*, 2999-3004.

Holden, D.A.; Watkins, J.J.; White, H.S. *Langmuir*, **2012**, *28*, 7572-7577.

Hines, M. A.; Todd, J. A.; Guyot-Sionnest, P. *Langmuir* **1995**, *11*, 493-497.

Howorka, S.; Siwy, Z. *Chem. Soc. Rev.* **2009**, *38*, 2360-2384.

Hu, H.; Ji, F.; Xu, Y.; Yu, J.; Liu, Q.; Chen, L.; Chen, Q.; Wen, P.; Lifshitz, Y.; Wang, Y.; Zhang, Q.; Lee, S.-T. *ACS Nano.* **2016**, *10*, 7323-7330.

Iler, R. K. *J. Colloid Interface Sci*. **1966**, *21*, 569-594.

Iraci, N.; Gaude, E.; Leonardi, T.; Costa, A. S. H.; Cossetti, C.; Peruzzotti-Jametti, L.; Bernstock, J. D.; Saini, H. K.; Gelati, M.; Vescovi, A. L.; Bastos, C.; Faria, N.; Occhipinti, L. G.; Enright, A. J.; Frezza, C.; Pluchino, S. *Nat. Chem. Biol.* **2017**, *13*, 951-955.

Ito, T.; Henriquez, R. R.; Crooks, R. M. *Acc. Chem. Res.* **2004**, *37*, 937-945.

Ito, T.; Sun, L.; Crooks, R. M. *Anal. Chem.* **2003**, *75*, 2399-2406.

Jahn, R.; Sudhof, T. C. *Annu. Rev. Neurosci.* **1994**, 17, 219-246.

Jia, J.; Wang, B.; Wu, A.; Cheng, G.; Li, Z.; Dong, S. *Anal. Chem*. **2002**, *74*, 2217-2223.

Jiang, Z.; He, J.; Deshmukh, S. A.; Kanjanaboos, P.; Kamath, G.; Wang, Y.; Sankaranarayanan, S. K. R. S.; Wang, J.; Jaeger, H. M.; Lin, X. M. *Nat. Mater*. **2015**, *14*, 912-917.

Jin, Y.; Shen, Y.; Dong, S. *J. Phys. Chem. B* **2004**, *108*, 8142-8147.

Kaewsaneha, C.; Tangboriboonrat, P.; Polpanich, D.; Eissa, M.; Elaissari, A. *ACS Appl. Mater. Interfaces* **2013**, *5*, 1857-1869.

Kahk, J. M.; Rees, N. V.; Pillay, J.; Tshikhudo, R.; Vilakazi, S.; Compton, R. G. *Nano Today*, **2012**, *7*, 174-179.

Karp, S.; Meites, L. *J. Am. Chem. Soc.* **1962**, *84*, 906-912.

Kim, B.-K.; Boika, A.; Kim, J.; Dick, J. E. Bard, A. J. *J. Am. Chem. Soc.* **2014**, *136*, 4849-4852.

Kim, Y.; Zhu, J.; Yeom, B.; Prima, M. D.; Su, X.; Kim, J. G.; Yoo, S., J.; Uher, C.; Kotov, N. *Nature* **2013**, *500*, 59-64.

Kleijn, S.E.F; Lai, S.C.S.; Koper, M.T.M.; Unwin, P.R. *Angew. Chem. Int. Ed*. **2014**, *53*, 3558-3586.

Knust, K. N.; Sheridan, E.; Anand, R. K.; Crooks, R. M. *Lab Chip* **2012**, *12*, 4107-4114.

Koper. M. T. M. *Nanoscale*, **2011**, *3*, 2054-2073.

Kumar, S.; Zou, S. *Langmuir* **2007**, *23*, 7365-7371.

Kuttiyiel, K. A.; Sasaki, K.; Park, G.-G.; Vukmirovic, M. B.; Wu, L.; Zhu, Y.; Chen, J. G.; Adzic, R. R. *Chem. Commun.* **2017**, *53*, 1660-1663.

Kwon, S. J.; Bard, A. J. *J. Am. Chem. Soc*. **2012**, *134*, 7102-7108.

Kwon, S. J.; Zhou, H.; Fan, F.-R. F.; Vorobyev, V.; Zhang, B.; Bard, A. J. *Phys. Chem. Chem. Phys.* **2011**, *13*, 5394-5402.

Lammert, P. E.; Crespi, V. H.; *J. Am. Chem. Soc*. **2004**, *126*, 13424-13431.

Lan, W. J.; Holden, D. A.; Zhang, B.; White, H. S. *Anal. Chem.* **2011**, *83*, 3840-3847.

Lan, W.; Kubeil, C.; Xiong, J.; Bund, A.; White, H. S. *J. Phys. Chem. C.* **2014**, *118*, 2726-2734.

Lang, X.; Chen, L.; Guan, P.; Fujita, T.; Chen, M. *Appl. Phys. Lett.* **2009**, **94**, 213109-1 - 213109-3.

Lebegue, E.; Anderson, C. M.; Dick, J. E.; Webb, L. J.; Bard, A. J. *Langmuir* **2015**, *31*, 11734-11739.

Lee, D.; Rubner, M. F.; Cohen, R. E. *Nano Lett.*, **2006**, *6*, 2305-2312.

Lei, C.; Hu, D.; Ackerman, E. J. *Chem. Commun.* **2008**, *0*, 5490-5492.

Lemay, S. G.; Kang, S.; Mathwig, K.; Singh, P. S. *Acc. Chem. Res.* **2013***, 46,* 369-377.

Li, J.; Stein, D.; McMullan, C.; Branton, D.; Aziz, M. J.; Golovchenko, J. A. *Nature* **2001**, *412*, 166-169.

Li, J. L.; Gershow, M.; Stein, D.; Brandin, E.; Golovchenko, J. A. *Nat. Mater*. **2003**, *2*, 611-615.

Major, J. S.; Blanchard, G. J. *Langmuir* **2001**, *17*, 1163-1168.

Li, X.; Dunevall, J.; Ewing, A. G. *Faraday Discuss*. **2018**, *210*, 353-364.

Li, Y.; Cox, J. T.; Zhang, B. *J. Am. Chem. Soc.* **2010**, *132*, 3047-3052.

Liu, G. Z.; Luais, E.; Gooding, J. J. *Langmuir* **2011**, *27*, 4176-4183.

Loget, G.; Roche, J.; Gianessi, E.; Bouffier, L.; Kuhn, A. *J. Am. Chem. Soc.* **2012**, *134*, 20033-20036.

Loget, G.; Zigah, D.; Bouffier, L.; Sojic, N.; Kuhn, A. *Acc. Chem. Res.* **2013**, *46*, 2513-2523.

Lovric, J.; Najafinobar, N.; Dunevall, J.; Majdi, S.; Svir, I.; Oleinick, A.; Amatore, C.; Ewing, *Faraday Discuss*., **2016**, *193*, 65-79.

Lu, J.; Fan, Y.; Howard, M. D.; Vaughan, J. C.; Zhang, B. *J. Am. Chem. Soc.* **2017**, *139*, 2964-2971.

Luo, Y.; Geng, S.; Dube, L.; Zhao, J. *J. Phys. Chem. C.* **2018**, *122*, 18077-18085.

Luo, L.; German, S. R.; Lan, W.-J.; Holden, D. A.; Mega, T. L.; White, H. S. *Annu. Rev. Anal. Chem.* **2014**, *7*, 513-535.

Masitas, R.A.; Allen, S.; Zamborini, F.P. *J. Am. Chem. Soc.* **2016**, *138*, 15295-15298.

Mavre, F.; Anand, R. K.; Laws, D. R.; Chow, K.-F.; Chang, B.-Y.; Crooks, J. A.; Crooks, R. M. *Anal. Chem.* **2010**, *82*, 8766-8774.

Mirkin Sun, P.; Mirkin, M. V. *J. Am. Chem. Soc.* **2008**, *130*, 8241-8250.

Miyabayashi, K.; Nishihara, H.; Miyake, M. *Langmuir* **2014**, *30*, 2936-2942.

Moorcroft, M. J.; Lawrence, N. S.; Coles, B. A.; Compton, R. G.; Trevani, L. N. *J. Electroanal. Chem.* **2001**, *506*, 28-33.

Normand, P.; Tsoukalas, D.; Petty, M. C. *Nano Lett.* **2003**, *3*, 533-536.

Ning, F.; Shao, M.; Xu, S.; Y. Fu, R. Zhang, M. Wei, D.G. Evans, X. Duan. *Energy Environ. Sci*., 2016, 9, 2633-2643.

Oja, S. M.; Robinson, D. A.; Vitti, N. J.; Edwards, M. A.; Yuwen Liu, White, H. S.; Zhang, B. *J. Am. Chem. Soc.* **2017**, *139*, 708-718.

Oja, S. M.; Fan, Y.; Armstrong, C. M.; Defnet, P.; Zhang, B. *Anal. Chem*. **2016**, *88*, 414-430.

Oja, S. M.; Guerrette, J. P.; David, M. R.; Zhang, B. *Anal. Chem.* **2014**, *86*, 6040-6048.

Oja, S. M.; Wood, M.; Zhang, B. *Anal. Chem.* **2013**, *85*, 473-486.

Oja, S.M.; Zhang, B. *Anal. Chem*. **2014**, *24*, 12299-12307.

Palacios, R. E.; Fan, F. R. F.; Bard, A. J.; Barbara, P. F. *J. Am. Chem. Soc.* **2006**, *128*, 9028-9029.

Palgrave, R. G.; Parkin, I. P. *J. Am. Chem. Soc.* **2006**, *128*, 1587-1597.

Pandey, P. A.; Bell, G. R.; Rourke, J. P.; Sanchez, A. M.; Elkin, M. D.; Hickey, B. J.; Wilson, N. R. *Small* **2011**, *7*, 3202-3210.

Park, J. H.; Boika, A.; Park, H. S.; Lee, H. C.; Bard, A. J. *J. Phys. Chem. C.* **2013**, *117*, 6651-6657.

Paul, S.; Pearson, C.; Molloy, A.; Cousins, M. A.; Green, M.; Kolliopoulou, S.; Dimitrakis, P.; Normand, P.; Tsoukalas, D.; Petty, M. C. *Nano Lett.* **2003**, *3*, 533-536.

Paxton, W. F.; Kistler, K. C.; Olmeda, C. C.; Sen, A.; St. Angelo, S. K.; Cao, Y.; Mallouk, T. E.; Demirok, U. K.; Laocharoensuk R.; Manesh, K. M.; Wang, J. *Angew. Chem. Int. Ed*. **2008**, *47*, 9349-9351.

Peng, F.; Tu, Y.; van Hest, J. C. M.; Wilson, D. A. *Angew. Chem.* **2015**, *127*, 11828-11831.

Peng, S.; Lee, Y.; Wang, C.; Yin, H.; Dai, S.; Sun, S. *Nano Res.* **2008**, *1*, 229-234.

Percival, S. J.; Zhang, B. *J. Phys. Chem. C.* **2016**, *120*, 20536-20546.

Perera, N.; Karunathilake, N.; Chhetri, P.; Alpuche-Aviles, M. A. *Anal. Chem.* **2015**, *87*, 777-784.

Roduner, E. *Chem. Soc. Rev.* **2006**, *35*, 583-592.

Pevarnik, M.; Healy, K.; Toimil-Molares, M.E.; Morrison, A.; Letant, S.E.; Siwy, Z.S. *ACS Nano* **2012,** *6*, 7295-7302.

Peyser, L. A.; Lee, T.-H.; Dickson, R. M. *J. Phys. Chem. B.* **2002**, *106*, 7725-7728.

Peyser, L. A.; Vinson, A. E.; Bartko, A. P.; Dickson, R. M. *Science* **2001**, *291*, 103-106.

Pfeiffer, C.; Rehbock, C.; Hühn, D.; Carrillo-Carrion, C.; Aberasturi, D.; Merk, V.; Barcikowski, S.; Parak. W. J. *J. R. Soc. Interface* **2014**, *11,* 20130931.

Polarz, S.; Smarsly, B. *J. Nanosci. Nanotechnol.* **2002**, *2*, 581-612.

Pradhan, S.; Ghosh, D.; Chen, S. *ACS Appl. Mater. Interfaces* **2009**, *1*, 2060-2065.

Pradhan, S.; Xu, L.; Chen, S. *Adv. Funct. Mater.* **2007**, *17*, 2385-2392.

Qin, W.; Peng, T.; Gao, Y.; Wang, F.; Hu, X.; Wang, K.; Shi, J.; Li, D.; Ren, J.; Fan, C. *Angew. Chem. Int. Ed.* **2017**, *56*, 515-518.

Quinn, M.; van't Hof, P. G.; Lemay, S. G. *J. Am. Chem. Soc.* **2004**, *126*, 8360-836.

Quinn, B. M.; Dekker: C.; Lemay, S. G. *J. Am. Chem. Soc*. **2005**, *127*, 6146-6147.

Riskin, M.; Tel-Vered, R.; Bourenko, T; Granot, E.; Willner, I. *J. Am. Chem. Soc.* **2008**, *130*, 9726-9733

Sanchez, A.; Díez, P.; Martínez-Ruíz, P.; Villalonga, R.; Pingarron, J. M. *Electrochem. Commun.* **2013**, *30*, 51-54.

Robinson, D. A.; Edwards, M. A.; Ren, H.; White, H. S. *ChemElectroChem.* **2018**, *5,* 1-10.

Sardesai, N. P.; Andreescu, D.; Andreescu, S. *J. Am. Chem. Soc.* **2013**, *135*, 16770-16773.

Schlicke, H.; Schroder J. H.; Trebbin M.; Petrov A.; Ijeh M.; Weller H.; Vossmeyer T. *Nanotechnology* **2011**, *22*, 305303-305311.

Schmidt, D. J.; Hammond, P. T. *Chem. Commun*. **2010**, *46*, 7358-7360.

Segalman, R. A. *Mater. Sci. Eng., R.* **2005**, *48*, 191-226.

Shao, M.; Chang, Q.; Dodelet, J.-P.; Chenitz, R.. *Chem. Rev.* **2016**, *116*, 3594-3657.

Shan, X.; Diez-Perez, I.; Wang, L.; Wiktor, P.; Gu, Y.; Zhang, L.; Wang, W.; Lu, J.; Wang, S.; Gong, Q.; Li, J.; Tao, N. *Nat. Nanotechnol.* **2012**, *7*, 668-672.

Sheridan, A. K.; Ngamukot, P.; Bartlett, P. N.; Wilkinson, J. S. *Sens. Actuators, B: Chem.* **2006**, *117*, 253-260.

Shi, W.; Friedman, A. K.; Baker, L. A. *Anal. Chem.* **2017**, *89*, 157-188.

Shin, H. C.; Dong, J.; Liu, M. *Adv. Mater.* **2003**, *15*, 1610-1614.

Shipway, A. N.; Lahav, M.; Blonder, R.; Willner, I. *Chem. Mater.* **1999**, *11*, 13-15.

Sieradzki, K.; Dimitrov, N.; Movrin, D.; McCall, C.; Vasiljevic, N.; Erlebacher, J. *J. Electrochem. Soc.* **2002,** *149*, 370-377.

Smeets, R. M. M.; Keyser, U. F.; Krapf, D.; Wu, M.-Y.; Dekker, N. H.; Dekker, C. *Nano Lett.* **2006**, *6*, 89-95.

Smirnov, E.; Peljo, P.; Scanlon, M. D.; Girault, H. H. *ACS Nano*. **2015**, *9*, 6565-6575.

Smith, T. *J. Colloid and Interface Sci.* **1980**, *75*, 51-55.

Sotiriou, G. A.; Hirt, A. M.; Lozach, P. Y.; Teleki, A.; Krumeich, F.; Pratsinis, S. E. *Chem. Mater.* **2011**, *23*, 1985-1992.

Stanley-Wood, N. G.; Lines, R. W. Royal Society of Chemistry: Cambridge, U. K. **1992**, 351-383.

Stockmann, T. J.; Angelé, L.; Brasiliense, V.; Combellas, C.; Kanoufi, F. *Angew. Chem. Int. Ed.* **2017**, *56*, 13493-13497.

Strein, T. G.; Ewing, A. G. *Anal. Chem.* **1992**, *64*, 1368-1373.

Strong, L.; Whitesides, G. M. *Langmuir* **1988**, *4*, 546-558.

Stuart, E. J. E.; Tschulik, K.; Batchelor-McAuley, C.; Compton, R. G. *ACS Nano.* **2014**, *8*, 7648-7654.

Such, G. K.; Quinn, J. F.; Quinn, A.; Tjipto, E.; Caruso, F. *J. Am. Chem. Soc*. **2006**, *128*, 9318-9319.

Sudhof, T. C.; Jahn, R. *Neuron*, **1991**, *6*, 665-677.

Suh, J. Y.; Lopez, R.; Feldman, L. C.; Haglund, R. F., Jr. *J. Appl. Phys.* **2004**, *96*, 1209-1213.

Sun, B. Y.; Chiu, D. T. *Anal. Chem.* **2005**, *77*, 2770-2776.

Talmon, Y.; Burns, J. L.; Chestnut, M. H.; Siegel, D. P. *J. Electron Microsc*. **1990**, *14*, 6-12.

Toh, H. S.; Compton, R. G. *Chem. Sci.* **2015**, *6*, 5053-5058.

Wakerley, D.; Güell, A. G.; Hutton, L. A.; Miller, T. S.; Bard, A. J.; Macpherson, J. V. *Chem. Commun.* **2013**, *49*, 5657-5659.

Unser, S.; Bruzas, I.; He, J.; Sagle, L. *Sensors,* **2015**, *15*, 15684-15716.

Walther, A.; Müller, A. H. E. *Chem. Rev.* **2013**, *113*, 5194-5261.

Wang, H. J.; Ishihara, S.; Ariga, K.; Yamauchi, Y. *J. Am. Chem. Soc*. **2012**, *134,* 10819-10821

Wang, J. Analytical Electrochemistry, John Wiley & Sons VCH, Hoboken, New Jersey, USA, **2006**.

Wang, J. *Microchimica Acta* **2012**, *177*, 245-270.

Wang, W.; Tao, N. *Anal. Chem.* **2014**, *86*, 2-14.

Wang, Y.; Kececi, K.; Mirkin, M. V.; Mani, V.; Sardesai, N.; Rusling, J. F. *Chem. Sci*. **2013**, *4*, 655-663.

Wang, S.; Jiang, S.; White, T. J.; Wang, X. *Electrochim. Acta.* **2010**, *55*, 7652-7658.

Watson, D. C.; Martinez, R. V.; Fontana, Y.; Russo-Averchi, E.; Heiss, M.; Morral, A. F.; Whitesides, G. M.; Loncar, M. *Nano Lett.* **2014**, *14*, 524-531.

Wei, Q.; Zhao, Y.; Xu, C.; Wu, D.; Cai, Y.; He, J.; Li, H.; Du, B.; Yang, M. *Biosens. Bioelectron*. **2011**, *26*, 3714-3718.

Wilson, D. A.; Nolte, R. J. M.; van Hest, J. C. M. *Nat. Chem.* **2012**, *4*, 268-274.

Wood, M.; Zhang, B. *ACS Nano.* **2015**, *9*, 2454-2464.

Xiao, X.; Bard, A. J. *J. Am. Chem. Soc*. **2007**, *129*, 9610-9612.

Xiao, X.; Fan, F.-R. F.; Zhou, J.; Bard, A. J. *J. Am. Chem. Soc.* **2008**, *130*, 16669-16677.

Xu, W.; Fu, K.; Bohn, P. W. *ACS Sens*. **2017**, *2*, 1020-1026.

Xu, W.; Shen, H.; Kim, Y.; J.; Zhou, X.; Liu, G.; Park, J.; Chen P. *Nano Lett.* **2009**, *9*, 3968-3973.

Xu, Z. *Energy & Environ. Sci.* **2008**, *1*, 454-466.

Yang, D.; Wilde, C. P.; Morin, M. *Langmuir* **1997**, *13*, 243-249.

Yang, R.; Leisch, J.; Strasser, P.; Toney, M. F. *Chem. Mater.* **2010**, *22*, 4712-4720.

Yan, X.; Meng, F.; Cui, S.; Liu, J.; Gu, J.; Zou, Z. *J. Electroanal. Chem*. **2011**, *661*, 44-48.

Ye, H.; Crooks, R. M. *J. Am. Chem. Soc.* **2007**, *129*, 3627-3633.

Yu, Y.; Huang, S.; Li, Y.; Steinmann, S. N.; Yang, W.; Cao, L. *Nano Lett*. **2014**, *14*, 553-558.

Yuana, Y.; Oosterkamp, T.H.; Bahatyrova, S.; Ashcroft, B.; Garcia Rodriguez, P.; Bertina, R.M.; Osanto, S. *J. Thromb. Haemost.* **2010**, *8*, 315-323.

Zhang, B.; Galusha, J.; Shiozawa, P. G.; Wang, G.; Bergren, A. J.; Jones, R. M.; White, R. J.; Ervin, E. N.; Cauley, C. C.; White, H. S. *Anal. Chem.* **2007**, *79*, 4778-4787.

Zhang, F.; Defnet, P. A.; Fan, Y.; Hao, R.; Zhang, B. *J. Phys. Chem. C.* **2018**, *11*, 6447-6455

Zhang, F.; Srinivasan, M. P. *Langmuir* **2007**, *23*, 10102-10108.

Zhang, J.; Grzybowski, B. A.; Granick, S. *Langmuir* **2017**, *33*, 6964-6977.

Zhang, L.; Chen, L.; Liu, H.; Hou, Y.; Hirata, A.; Fujita, T.; Chen, M. *J. Phys. Chem. C* **2011**, *115*, 19583-19587.

Zhang, X.; Chen, C.; Li, J.; Zhang, L.; Wang, E. *Anal. Chem.* **2013**, *85*, 5335-5339.

Zhang, X.; Zhai, Q.; Xing, H.; Li, J.; Wang, E. *ACS Sensors* **2017**, *2*, 320-326.

Zhang, Y.; Guan, Y.; Yang, S.; Xu, J.; Han, C. *Adv. Mater*. **2003**, *15*, 832-835.

Zhao, B.; Collinson, M. M. *J. Electroanal. Chem.* **2012**, *684*, 53-59.

Zhao, L. Y.; Eldridge, K. R.; Sukhija, K.; Jalili, H.; Heinig, N. F.; Leung, K. T. *Appl. Phys. Lett.* **2006**, *88*, 033111.

Zhao, J.; Zaino, L. P.; Bohn, P. W. *Faraday Discuss.* **2013**, *164*, 57-69.

Zhong, C.-J.; Luo, J.; Njoki, P. N.; Mott, D.; Wanjala, B.; Loukrakpam, R.; Lim, S.; Wang, L.; Fang, B.; Zhou, H.; Fan, F.-R. F.; Bard, A. J. *J. Phys. Chem. Lett.* **2010**, *1*, 2671-2674.

Zhou, K.; Li, L.; Tan, Z.; Zlotnick, A.; Jacobson, S. C. *J. Am. Chem. Soc.* **2011**, *133*, 1618-1621.

Zong, C.; Chen, C.; Zhang, M.; Wu, D.; Ren, B. *J. Am. Chem. Soc.* **2015**, *137*, 11768-11774.

Zou, L.; Li, Y.; Cao, S.; Ye, B. *Talanta* **2013**, *117*, 333-337.

Chu HAN

hanchu1993@gmail.com 36 Bagley Hall, Seattle, WA 98195 (206)295-8020
https://www.linkedin.com/in/chu-han-282a1188

Skills

Research background in electrochemistry, nanotechnology, and material science

Extensive experience in surface modification: thin film coating, plasma etching, wet etching

Expertise in nanomaterial characterization: optical microscopy, SEM, TEM, in situ TEM, XPS, GC, Nanoparticle Tracking Analysis (NTA), UV-vis.

Data analysis skills with Microsoft office, ImageJ, Origin

Experience in Finite Element Analysis (FEA) with COMSOL

Scientific writing and oral presentation skills

Programming: Matlab, Python

Education

University of Washington Seattle, WA
Ph.D. candidate, Chemistry 2013 – Dec 2018(expected)

University of Science and Technology of China Hefei, China
Bachelor of Science, Material Science and Engineering 2009 - 2013

Research Experience

University of Washington, Graduate Research Assistant 2013 - present

- **Designing ultrathin nanoparticle films (30-200 nm) for electrical analysis and electrocatalysis study.**
  - Designed and fabricated tunable layer-by-layer cross-linked nanoparticle film as an excellent electrocatalyst toward oxygen reduction reaction.
  - The structure and morphology of the film was characterized by SEM, TEM and XPS. The electrochemical activity and conductivity was tuned by plasma treatment and electrochemical potential cycling.
  - Relevant skills: XPS, SEM, TEM, spin coating, oxygen plasma cleaning, wet etching, photolithography
- **Studying transient electrochemistry of single nanoparticles translocating through a glass nanopore.**
  - Designed a unique system to observe transient electrochemical bipolar coupling on free moving nanoparticles.
  - Researched into the phenomenon with electrochemical method and fluorescence microscopy, generated Finite Element Model of the system.
  - Relevant skills: optical microscopy, glass nanopipette fabrication and characterization, data processing and COMSOL simulation, SEM.
- **Fabrication of single germanium nanowire.**
  - Fabricated single germanium wire on a nanoelectrode surface with an electrochemical liquid-liquid-solid crystal growth method (ec-LLS) under room temperature.
  - Relevant skills: nanoelectrode fabrication, electrodeposition, coulometry, SEM
- **Bipolar Electrochemistry of a Nanopore-Supported Nanoparticle Electrode.**
  - Worked with team members and fabricated a quartz nanopore-supported nanoparticle electrode.
  - Relevant skills: nanofabrication.

University of Science and Technology of China, Undergraduate Research Assistant 2011 - 2013

- **Synthesized highly sensitive surface enhanced Raman spectroscopy (SERS) substrates for R6G detection.**
  - Nanomaterials synthesis

- **Prepared Cu-based and Ir-based catalyst, achieved high yield and selectivity in biomass conversion.**
  - Organic synthesis**,** trained on using GC (gas chromatography)

Teaching Experience

University of Washington, Graduate Teaching Assistant
General Chemistry (CHEM142): Fall 2017, Spring 2018, Autumn 2018
General Chemistry (CHEM152): Winter 2016, Winter 2018
General Chemistry (CHEM162): Spring 2014, Fall 2014, Spring 2017
Electrochemistry (CHEM521, graduate level class): Fall 2016
Tutor in chemistry study center: Fall 2013, Winter 2014, Fall 2016
Responsibilities: review lecture notes and worksheet in quiz sections, lead lab sections, hold weekly office hours, grade lab reports and exams.

Publications

1. **Han, C**.; Hao, R; Fan, Y.; Zhang, B. "Observing Transient Electrochemistry of Single Nanoparticles Translocating through a Nanopore." *J. Am. Chem. Soc.* **2018**, in revision.
2. **Han, C**.; Luo, Y.; Gunderson, C.; Zhao J.; Zhang, B. "Characterization of the Apparent Electroactive Area of Janus Au-SiO_2 Nanoparticles Using Single-Nanoparticle Collision." **2018**, to be submitted.
3. Defnet, P. A.; **Han, C**.; Zhang, B. "Hydrogen Adsorption during Single-Particle Collision." **2018**, to be submitted.
4. Fan, Y.; Hao, R.; **Han, C**.; Zhang, B. "Counting Single Redox Molecules in a Nanoscale Electrochemical Cell." **2018**, *Anal. Chem*.in revision.
5. Hao, R.; Fan, Y.; **Han, C**.; Zhang, B. "Bipolar Electrochemistry of a Nanopore-Supported Nanoparticle Electrode." *Anal. Chem*., **2017**, *89*, 12652−12658.
6. **Han, C**.; Percival, S. J.; Zhang, B. "Electrochemical Characterization of Ultrathin Cross-linked Metal Nanoparticle Films." *Langmuir*, **2016**, *32*, 8783−8792.
7. Fan, Y.; **Han, C**.; Zhang, B. "Recent Advances in Development and Application of Nanoelectrodes." *Analyst*, **2016**, *141*, 5474-5487.
8. Li, R.; **Han, C**.; Chen, Q. A Facile Synthesis of Multifunctional ZnO/Ag Seaurchin-like Hybrids as Highly Sensitive Substrates for Surface-enhanced Ramen Detection. *RSC Advances*, **2013**, *3*, 11715-11722.

Awards

Graduate Student Travel Award 2017
(Graduate School Fund for Excellence and Innovation (GSFEI), University of Washington)

Yan Dongsheng Fellowship 2011
(Shanghai Institute of Ceramics, Chinese Academy of Sciences)

Outstanding Student Scholarship 2010, 2012
(University of Science and Technology of China)

Conferences

Pittsburgh Conference on Analytical Chemistry and Applied Spectroscopy (Pittcon), Chicago, March 2017
oral presentation: "Electrochemical Characterization of Ultrathin Cross-linked Metal Nanoparticle Films."